

# NAVAL POSTGRADUATE SCHOOL

## Monterey, California



## THESIS

### SCENE CLASSIFICATION USING HIGH SPATIAL RESOLUTION MULTISPECTRAL DATA

by

Jamada Jerael Garner

June 2002

Thesis Advisor:  
Second Reader:

Richard C. Olsen  
David Trask

**Approved for public release; distribution is unlimited.**

THIS PAGE INTENTIONALLY LEFT BLANK

<b>REPORT DOCUMENTATION PAGE</b>			<i>Form Approved OMB No. 0704-0188</i>	
Public reporting burden for this collection of information is estimated to average 1 hour per response, including the time for reviewing instruction, searching existing data sources, gathering and maintaining the data needed, and completing and reviewing the collection of information. Send comments regarding this burden estimate or any other aspect of this collection of information, including suggestions for reducing this burden, to Washington headquarters Services, Directorate for Information Operations and Reports, 1215 Jefferson Davis Highway, Suite 1204, Arlington, VA 22202-4302, and to the Office of Management and Budget, Paperwork Reduction Project (0704-0188) Washington DC 20503.				
<b>1. AGENCY USE ONLY (Leave blank)</b>		<b>2. REPORT DATE</b> June 2002	<b>3. REPORT TYPE AND DATES COVERED</b> Master's Thesis	
<b>4. TITLE AND SUBTITLE:</b> Scene Classification using High Spatial Resolution Multispectral Data			<b>5. FUNDING NUMBERS</b>	
<b>6. AUTHOR(S)</b> Jamada J. Garner				
<b>7. PERFORMING ORGANIZATION NAME(S) AND ADDRESS(ES)</b> Naval Postgraduate School Monterey, CA 93943-5000			<b>8. PERFORMING ORGANIZATION REPORT NUMBER</b>	
<b>9. SPONSORING /MONITORING AGENCY NAME(S) AND ADDRESS(ES)</b> N/A			<b>10. SPONSORING/MONITORING AGENCY REPORT NUMBER</b>	
<b>11. SUPPLEMENTARY NOTES</b> The views expressed in this thesis are those of the author and do not reflect the official policy or position of the Department of Defense or the U.S. Government.				
<b>12a. DISTRIBUTION / AVAILABILITY STATEMENT</b> Approved for public release; distribution is unlimited.			<b>12b. DISTRIBUTION CODE</b>	
<b>13. ABSTRACT (maximum 200 words)</b> Spectral imagery has traditionally been an important tool for terrain categorization (TERCAT). High-spatial resolution (8-meter), 4-color MSI data from IKONOS provide a new tool for scene classification. The utility of these data are studied for the purpose of classifying the Elkhorn Slough and surrounding wetlands in central California. The specific goal was to determine to what degree an existing classification map could be replicated using the 4-color imagery. The existing map was used as an input to a supervised classification process. Errors in that map required development of revised exemplar spectra sets, eliminating mixed classes. Classification was done using a spectral angle mapper and maximum likelihood classifier. Results were compared to the original classification map. Confusion matrix calculations showed agreement at the 10-20% level. This lack of agreement is attributed to errors in the original map at the relatively high resolution of IKONOS.				
<b>14. SUBJECT TERMS</b> Remote Sensing, Multispectral, Ikonos, Landsat 7, High Resolution, Scene Classification			<b>15. NUMBER OF PAGES</b> 158	
			<b>16. PRICE CODE</b>	
<b>17. SECURITY CLASSIFICATION OF REPORT</b> Unclassified	<b>18. SECURITY CLASSIFICATION OF THIS PAGE</b> Unclassified	<b>19. SECURITY CLASSIFICATION OF ABSTRACT</b> Unclassified	<b>20. LIMITATION OF ABSTRACT</b> UL	

NSN 7540-01-280-5500

Standard Form 298 (Rev. 2-89)  
Prescribed by ANSI Std. Z39-18

THIS PAGE INTENTIONALLY LEFT BLANK

**Approved for public release; distribution is unlimited.**

**SCENE CLASSIFICATION USING HIGH SPATIAL RESOLUTION  
MULTISPECTRAL DATA**

Jamada J. Garner  
Ensign, United States Navy  
B.S., The Florida A&M University, 2001

Submitted in partial fulfillment of the  
requirements for the degree of

**MASTER OF SCIENCE IN APPLIED PHYSICS**

from the

**NAVAL POSTGRADUATE SCHOOL  
June 2002**

Author: Jamada J. Garner

Approved by: Richard C. Olsen  
Thesis Advisor

David M. Trask  
Second Reader

William B. Maier II  
Chairman, Department of Physics

THIS PAGE INTENTIONALLY LEFT BLANK

## **ABSTRACT**

Spectral imagery has traditionally been an important tool for terrain categorization (TERCAT). High-spatial resolution (8-meter), 4-color Multispectral Imagery (MSI) data from IKONOS provide a new tool for scene classification. The utility of these data are studied for the purpose of classifying the Elkhorn Slough and surrounding wetlands in central California. The specific goal was to determine to what degree an existing classification map could be replicated using the 4-color imagery. The existing map was used as an input to a supervised classification process. Errors in that map required development of revised exemplar spectra sets, eliminating mixed classes. Classification was done by using a spectral angle mapper and maximum likelihood classifier. Results were compared to the original classification map. Confusion matrix calculations showed agreement at the 10-20% level. This lack of agreement is attributed to errors in the original map at the relatively high resolution of IKONOS.

THIS PAGE INTENTIONALLY LEFT BLANK

## TABLE OF CONTENTS

I.	INTRODUCTION.....	1
II.	MULTISPECTRAL IMAGING THEORY .....	3
	A. SPECTRAL REMOTE SENSING.....	3
1.	Background .....	3
2.	Electromagnetic Spectrum .....	4
3.	Spectral Response .....	5
4.	General Radiation Laws .....	7
	a. Electromagnetic Radiation .....	7
	b. Planck Radiation Laws.....	9
	c. Spatial Resolution Limitations .....	12
	B. SENSING THE EARTH'S SURFACE .....	14
1.	Radiation Propagation in the Atmosphere .....	14
2.	Radiation Interacting with Surface Materials.....	19
III.	COLLECTING SPECTRAL INFORMATION.....	23
	A. REMOTE SENSING PLATFORMS .....	23
1.	Altitudes of Operation.....	23
2.	Airborne Sensors .....	23
	a. Camera Components .....	24
	b. Strip Cameras .....	24
	c. Panoramic Cameras.....	25
	d. Metric Cameras .....	25
	e. Image Distortions .....	25
	f. Geographic Information Systems.....	26
3.	Spaceborne Multispectral Scanning Systems.....	27
	a. Charge Coupled Imager .....	27
	b. Traverse and Pushbroom Scanning .....	28
4.	Other Remote Sensing Systems .....	28
	B. RESOLUTION.....	28
IV.	MULTISPECTRAL DATA ANALYSIS TOOLS .....	31
	A. MULTISPECTRAL DATA .....	31
1.	Digital Images .....	31
	B. PRINCIPAL COMPONENTS ANALYSIS.....	32
	C. MULTISPECTRAL IMAGE CLASSIFICATION.....	33
1.	Supervised Classification .....	34
	a. Maximum Likelihood.....	34

b.	Spectral Angle Mapper.....	35
D.	ACCURACY ACESSMENT.....	36
V.	LANDSAT 7 AND IKONOS .....	39
A.	OPERATIONAL DIFFERENCES .....	39
B.	LANDSAT 7 .....	39
1.	The Enhanced Thematic Mapper Plus .....	39
2.	Orbit .....	40
3.	Radiometric Calibration and Relative Spectral Response.....	40
C.	IKONOS.....	43
1.	Sensor System .....	43
2.	Radiometric Calibration and Relative Spectral Response.....	44
VI.	MULTISPECTRAL ANALYSIS .....	47
A.	DESCRIPTION OF STUDY AREA.....	47
B.	COLLECTING DATA.....	47
C.	PROCESSING DATA .....	48
D.	TRAINING DATA .....	48
E.	CLASSIFICATION .....	50
1.	Spectral Angle Mapper.....	50
2.	Maximum Likelihood.....	50
F.	CONFUSION MATRIX .....	51
G.	RESULTS.....	51
VII.	SUMMARY AND CONCLUSION.....	53
	APPENDIX A. GENERAL FIGURES AND TABLES .....	55
	APPENDIX B. FIGURES AND TABLES OF RESULTS.....	93
	LIST OF REFERENCES .....	141
	INITIAL DISTRIBUTION LIST .....	143

## LIST OF SYMBOLS AND ACRONYMS

$\lambda$	wavelength
$h$	Planck's constant
$\overline{K}$	wavenumber
$\nu$	frequency
$T$	temperature
$\overline{k}$	Boltzmann constant
$c$	speed of light
$L$	spectral emittance or radiance
$\theta$	angle relative to the normal
$d\Omega$	solid angle element
$\overline{M}$	total power
$\Lambda$	Stefan-Boltzmann constant
$\beta$	absorptance
$\rho$	reflectance
$\tau$	transmittance
$\varepsilon$	emissivity
$J$	Bessel function
$D$	diameter
$I$	intensity
$\sigma_m$	Rayleigh scattering coefficient
$R$	path length

$\sigma_r$	Rayleigh scattering cross section
$n$	index of refraction
$N$	molecular number density
$\sigma_a$	aerosol attenuation coefficient
$M$	aerosol number density
$c_n$	speed of propagation in material with index of refraction $n$
$C_n^2$	refractive index structure parameter
$C_T^2$	temperature structure parameter
$h$	height
$f$	angular frequency
$OTF$	optical transfer function
$A$	optical transfer function parameter
$E$	energy
$\bar{Y}$	set of pixels in principle components space
$G$	linear principle components transformation matrix
$\bar{X}$	set of pixels in original space
$\alpha$	spectral angle
$t$	unclassified scene spectrum
$r$	reference spectra
$\bar{N}$	number of bands of spectral data
$e_{ii}$	confusion matrix elements
$\bar{P}$	total number of pixels

$\bar{c}$	total number of classes
$p$	probability
$x$	set of pixels in image $x$
$y$	set of pixels in image $y$
$Q$	quantized detector responses
$G$	gain
$B$	bias
$RSR$	relative spectral response
$a$	emissivity adjusted view factor
$i, j, k$	indices of summation
$Calcoef$	calibration coefficients
$\overline{A_{opt}}$	clear aperture area
$\Omega$	instantaneous field of view (band specific)
$\bar{R}$	spectral responsivity
$R'$	peak-normalized spectral response
ESF	Elkhorn Slough Foundation
GPS	Global Positioning System
ROI	Region of Interest
NDV	$\bar{N}$ -Dimensional Visualizer
ENVI	Environment for Visualizing Information
ETM+	Enhanced Thematic Mapper Plus
MTF	Modulation Transfer function

IFOV	Instantaneous Field of View
HITRAN	High Resolution Transmission Molecular Absorption database
MODTRAN	Moderate Resolution Transmittance
OTF	Optical Transfer Function
BRDF	Bi-directional reflectance distribution function
GCP	Ground Control Points
MSS	Multispectral Scanning System
HSS	Hyperspectral Scanning System
USS	Ultraspectral Scanning System
CCI	Charged Coupled Imager
CCD	Charge Coupled Device
PCA	Principle Components Analysis
SAM	Spectral Angle Mapper Classifier
MAXL	Maximum likelihood Classifier
Kappa	Coefficient of Agreement
SDUH	Science Data Users Handbook
TMC	Thematic Mapper Calibrator
IC	Internal Calibrator
PASC	Partial Aperture Solar Calibrator
FASC	Full Aperture Solar Calibrator
DC	Direct Current
DN	Digital Number

## **ACKNOWLEDGMENTS**

The author would like to thank Erick Van Dyke of the Elkhorn Slough Foundation for providing invaluable data regarding the Elkhorn Slough and its surrounding wetlands. Also, the author would like to thank Alan A. Ross of the Naval Postgraduate School for providing helpful preliminary background information about the Elkhorn Slough. My greatest appreciation goes to Professor Richard C. Olsen of the Naval Postgraduate School Physics Department for his time and insight into spectral image classification and use of the ENVI software. Finally, the author would like to thank his wife Janice for her patience and support.

## I. INTRODUCTION

For over 150 years, spectral remote sensing has been an acknowledged utility, dating back to the invention of the camera. While spectral remote sensing has enjoyed substantial development since the camera's inception, recent advances in video, scanners, cameras, and other remote sensing support systems have produced sensor platforms of high spatial, spectral, and radiometric resolution.

In September 1999, the Ikonos satellite was launched by Lockheed Martin for Space Imaging. Ikonos had the world's highest resolution among commercial satellites for two years. Its camera, built by Eastman Kodak, provides  $1\text{ m}/11\text{ bit}$  panchromatic and  $4\text{ m}/11\text{ bit}$  four band multispectral data. This represents a substantial improvement in resolution over the Landsat 7 satellite launched in April 1999, that supports the Enhanced Thematic Mapper Plus sensor.

The utility of image classification schemes is affected by increased resolution. In a classified image, high resolution may result in classified regions without sufficiently defined boundaries. In general, in some instances, increased resolution merely introduces noise that obscures the features of most interest to the observer (Wilkie and Finn, 1996). However, the use of appropriate training data sets in performing a supervised image classification may provide the necessary means, variances, and covariances to combat this noise associated with high resolution.

The goal of this thesis is to create a class map of the Elkhorn Slough and its surrounding wetlands. The Environment for Visualizing Information (ENVI) software and a reference class map of the study area provided by the Elkhorn Slough Foundation

will be used. A comparison of the created and reference class maps will be made. The comparison will be used to evaluate the utility of using four band high resolution data and training data to perform scene classification.

Chapter II of this thesis will present a description of spectral remote sensing and multispectral imaging theory. Chapter III discusses the means by which multispectral data is acquired and corrected. Multispectral data and classification schemes are explained in Chapter IV. The Ikonos and Landsat 7 remote sensing systems are described in Chapter V. Chapter VI presents the study area and spectral analysis. Chapter VII provides a summary of the spectral analysis and causes of any inaccuracy.

## **II. MULTISPECTRAL IMAGING THEORY**

### **A. SPECTRAL REMOTE SENSING**

#### **1. Background**

Remote sensing is the process of acquiring and recording information about an object without being in direct contact with that object (Gibson, 2000). Although this information may present itself in various forms, sensing the electromagnetic spectral information produced by an object is of concern here. The process of sensing electromagnetic spectral information is referred to as spectral remote sensing. The unique way that each object emits, reflects, absorbs, or scatters electromagnetic radiation allows an electromagnetic sensing device to discriminate between different objects. Objects typically produce a spectral signature by reflecting electromagnetic energy produced from a source that could be local or non-local to the remote sensing platform that contains the sensing device. These two processes are referred to as active and passive remote sensing respectively. The sensor collects this energy in spectral bands defined at particular regions of the electromagnetic spectrum. The energy is then converted into computer processable data that can be displayed in a more usable form called an image.

An essential element in remote sensing is the ability to record images of the earth's surface (Campbell, 1996). Space borne or airborne sensors are typically used to record these images as their operational altitudes provide a means for collecting spectral information from large areas. They provide us with as much or more detail than field surveys, accomplish this over large areas, and can do so repeatedly (Wilkie and Finn,

1996). The spectral characteristics of a region or scene can provide detailed information about that scene such as its human land use, water resources, and distribution of vegetation as multiple images can be obtained simultaneously from different wavelength bands. Hence using multispectral imaging, spectral information from the near infrared, short-wave infrared, mid-wave infrared, and long-wave infrared region can be collected. These regions are outside the visible portion of the electromagnetic spectrum. These bands are used to discriminate features that are not visible to the human eye (Multispectral Users Guide, 1995).

Collecting spectral data using space borne or airborne sensors is a nonintrusive way to obtain information that could provide support to address questions concerning conserving a biological system. Human subsistence and market activities are bringing increasing distress to ecological systems around the globe, jeopardizing the structure, function, production, and resilience of earth's life support systems (Wilkie and Finn, 1996).

## **2. Electromagnetic Spectrum**

The electromagnetic energy collected by a remote sensing device can be characterized by its distribution of wavelengths. A continuum consisting of all possible wavelengths is called the electromagnetic spectrum. Figure 2.1 defines some useful regions of the electromagnetic spectrum. However the range of wavelengths between  $0.4\mu m$  to  $14.0\mu m$  is most used in spectral remote sensing. This is attributable to the existence of several wavelength sub-bands between  $0.4\mu m$  and  $14.0\mu m$  that allow partial or complete transmission of electromagnetic radiation through the atmosphere.

These wavelength sub-bands are referred to as atmospheric windows. The atmosphere attenuates radiation passing through it on a one-way trip for about 100 kilometers. If a sensor is carried by a low-flying aircraft, effects of the atmosphere on image quality may be negligible (Campbell, 1996).

Figure 2.2 shows the locations of atmospheric windows used in remote sensing. Atmospheric windows are defined by regions of high transmission. Passive remote sensing systems take advantage of this by using the sun's illumination to sense at wavelengths from  $0.4\mu m$  to  $3.0\mu m$ . Active remote sensing systems must generate radiation within an atmospheric window. The most common active remote sensing system is radar that produces electromagnetic radiation in the microwave band of the spectrum (Gibson, 2000).

### **3. Spectral Response**

The spectrum of reflected wavelengths for reflective materials can be depicted graphically as a reflectivity curve. The reflectivity curve yields reflectance as a percentage of incident radiation reflected from a specific material as a function of the incident radiation's wavelength. The percentage is called albedo. Figure 2.3 presents typical albedos of several materials observed in the visible and near infrared bands.

The curves differ dramatically as each material interacts with the sun's radiation to reflect energy in distinct ways. For healthy vegetation, chloroplasts that contain chlorophyll reflect wavelengths corresponding to greenish colors (between  $0.7\mu m$  and  $1.3\mu m$ ) as the chloroplasts absorb all other wavelengths. In the process of absorption, the incident radiant energy is transformed and not reflected. Between 10 and 30 percent

of the total amount of visible light arriving at the surface of a leaf is reflected back as green (Gibson, 2000). The near infrared wavelengths yields an even greater spectral response in healthy vegetation as mesophyll cells in leaves reflect about 60 percent of the incident near infrared radiation that reaches the leaves. Since the abundance of chlorophyll and mesophyll in plants with leaves are directly linked to their health, poor plant health yields lesser reflectance in both the green and the near infrared.

The presence of rocks, soils, or moisture with vegetation is almost inevitable. This will significantly affect the spectral signature of a scene said to be vegetation. Soils constitute the primary background spectral response in most vegetated landscapes, and, in combination with rock, the sole spectral response in nonvegetated terrain (Wilkie and Finn, 1996). Soils from different regions may produce different spectral responses as the mineral composition of soils varies from region to region. Mineral reflectance spectra are strongly dependent on the chemical composition of the rock (Elachi, 1987). Wavelengths from  $2.08\ \mu m$  to  $2.35\ \mu m$  have strong absorptions in materials containing hydroxyl ions making these wavelengths useful for identifying hydrothermally altered rocks.

Moisture tends to reduce the overall reflectance of all materials. As the moisture content of a material increases, the material's reflectance tends towards the reflectance of water. This is partly responsible for enabling one to distinguish between soil regions differing in extents of irrigation. Likewise, one is also able to distinguish between water regions with different soil concentrations. For example, a pond is a body of still water, and under most conditions will have a different soil concentration than a river, stream, or any other body of running water. In these cases the one would expect the reflectivities to be closer to clear water than soil or even moist soil but still discernable from one another.

Clear water appears blue because of its high reflectance between wavelengths of  $0.4\ \mu\text{m}$  and  $0.6\ \mu\text{m}$  and appears black at wavelengths beyond  $0.7\ \mu\text{m}$ . Water appears black in the infrared where its absorption is relatively high and reflectance is low. Figure 2.4 illustrates how deeply radiation can penetrate into clear water. When soil or other particulate is suspended in water, depending on the depth and concentration of the soil or particulate, the spectral reflectance deviation from clear water can be dramatic. For example, plankton reflects in the green and near infrared. However, water containing plankton only reflects in the green. Figure 2.4 shows that the plankton filled water is green because green wavelengths not only penetrate to reach more plankton, they emerge from the water with far less attenuation than the infrared wavelengths. This idea becomes important when viewing water in a false color composite.

#### **4. General Radiation Laws**

To be modeled as a black body, a body must emit the maximum intensity of radiance across all wavelengths that it is theoretically possible to radiate for the particular temperature of the body (Gibson, 2000). True black bodies do not exist; a black body is an idealized concept. Being a black body requires it to absorb all radiation incident upon it and emit radiation at the maximum theoretical rate. In defining this maximum theoretical rate, it is instructive to begin with the production of radiation.

##### ***a. Electromagnetic Radiation***

Electromagnetic radiation is generated by the conversion of energy from other forms such as kinetic, chemical, or nuclear (Elachi, 1987). Materials generate this

radiation as their molecules seek lower energy states. The frequency of radiation generated by a material depends upon the process by which the material's molecules seek lower energy states. Electronic transitions in atoms tend to produce radiation in the visible and ultraviolet wavelengths. Infrared wavelengths are produced by vibrational and rotational transitions in molecules.

When radiation is produced by any material, it may possess a degree of polarization. Electromagnetic radiation consists of waves with alternating electric and magnetic fields. These electric and magnetic fields are perpendicular to each other and are in a plane perpendicular to the direction of wave propagation. However the orientation of the fields relative to a coordinate frame may be defined in any direction. The orientation of the fields is termed the polarization of the radiation (Rees, 1990). The types of polarization that the fields could have are called plane, circular, elliptical, and random polarization. In plane polarization the net electric and magnetic fields each sweep out planes as the wave propagates. In circular polarization the net electric and magnetic each fields sweep out helices as the wave propagates, and the helices can rotate either clockwise or counter clockwise about the direction of propagation. These rotations further define circular polarization as being either left-hand circularly polarized or right-hand circularly polarized. A simple consistent convention would distinguish the two. In elliptical polarization the net electric and magnetic fields each sweep out elliptical helices as the wave propagates. In random polarization the radiation is a mixture of the plane, circularly, and elliptically polarized waves. Radiation in this condition is also said to be unpolarized. Sun radiation is said to be unpolarized (Gibson, 2000). The importance of polarization lies in the fact that some sensing devices are designed to only detect

radiation of a particular polarization, and processes of reflection and absorption may alter the polarization of radiation. The effects of polarization generally do not become considerable until sensors try to collect radiation at relatively long wavelengths. Polarization is not considered in the visible and infrared region, but is considered in the microwave region used by radar.

***b. Planck Radiation Laws***

It was mentioned that the sun is a source of polarized radiation. It is also a source that could be considered a black body as previously defined. The sun has a surface temperature of 5,750-6,000  $K$  and radiates across a range of wavelengths at an average distance from the Earth of 150 million kilometers (Gibson, 2000). To compute the distribution of energy among these wavelengths the Planck Radiation Law applies. This radiation law is Equation 2.1. Equation 2.1 yields the spectral emittance of a black body as a curve. Figure 2.5 in Appendix A gives the spectral emittance of three black body sources.

$$L_v(T) = \frac{2h\nu^3}{c^2(e^{\frac{h\nu}{kT}} - 1)} \quad [\text{Equation 2.1}]$$

$$h = \text{Planck's constant } (6.6261 \times 10^{-34} J - s)$$

$$\nu = \frac{c}{\lambda} \text{ (} s^{-1} \text{)}$$

$$T = \text{Temperature (} K \text{)}$$

$$\bar{k} = \text{Boltzmann constant } (1.3807 \times 10^{-23} J - K^{-1})$$

$$c = \text{Speed of light } (3 \times 10^8 \frac{m}{s})$$

$$\lambda = \text{Wavelength } (m)$$

Like the sun, the earth is also considered a black body. The peak of the curve represents the wavelength that contains the greatest intensity of emitted radiation. To compute this wavelength the Wien Displacement Law applies. This law is Equation 2.2.

$$\lambda_{\max} = \frac{\delta}{T} \quad [\text{Equation 2.2}]$$

$$\delta = 2,898 \mu m - K$$

$$T = \text{Temperature } (K)$$

Following the equation development of W.G.Rees, 1990, to compute the total radiant exitance produced by a black body, first the spectral emittance (Equation 2.1) is integrated over all wavelengths or frequencies to yield  $L$ . It is then used in Equation 2.3 to define the total radiant exitance (Equation 2.4).

$$Irradiance = \int_{2\pi} L(\cos \theta) d\Omega \quad [\text{Equation 2.3}]$$

$$\theta = \text{Angle of incidence relative to the normal}$$

$$d\Omega = \text{Solid angle containing the incoming radiation}$$

$$L = \text{Total radiance}$$

$$\overline{M} = \Lambda T^4 \text{ where } \Lambda = \frac{2\pi^5 \overline{k}^4}{15c^2 h^3} \quad [\text{Equation 2.4}]$$

The  $\Lambda$  is called the Stefan-Boltzmann constant and its value is  $5.67 \times 10^{-8} \text{ Wm}^{-2} \text{ K}^{-4}$ .

These equations become very useful calibrating remote sensing devices.

Recall that Equation 2.1 and Equation 2.4 are based upon the idea that the materials whose spectral characteristics they describe are ideal sources and sinks. Real sources and sinks involve less than 100% radiative processes. These processes are absorption, reflection, and scattering. They are measured as ratios of their individual radiant powers to incident radiant power. If  $\beta$  is the absorptance,  $\rho$  is the reflectance, and  $\tau$  is the transmittance, then Equation 2.5 must hold.

$$\beta + \rho + \tau = 1 \quad [\text{Equation 2.5}]$$

If an object has the properties  $\beta = 1$  and  $\rho = \tau = 0$ , then the object is a black body (Seyrafi and Hovanessian, 1993). Equations 2.1 and 2.4 must be modified to describe real sources and sinks. The modification factor is called emissivity. Kirchoff's law states that the ratio of emitted radiation flux to absorbed radiation flux is the same for all blackbodies at the same temperature (Campbell, 1996). This ratio is emissivity. It is defined by Equation 2.6.

$$\varepsilon_\lambda = \frac{L_v}{L_{v,p}} \quad [\text{Equation 2.6}]$$

$L_{\nu,p}$  = Black Body Radiance at wavelength  $\lambda$

$$\rho = 1 - \varepsilon \quad [\text{Equation 2.7}]$$

$\rho$  = Reflectivity with zero transmittance

Materials with  $\varepsilon = 1$  are black bodies, with  $\varepsilon = 0$  are called white bodies, and with  $0 < \varepsilon < 1$  are called gray bodies. Equations 2.1 and 2.4 are modified by simply multiplying them by the appropriate emissivity to describe real bodies.

Emissivity becomes very important when sensing radiation from  $7 \mu m$  to  $18 \mu m$ , the thermal infrared region. Many of the same kinds of film, filters, and cameras that we use in the visible portion of the spectrum can also be used, with minor variations, for imaging in the near infrared (Campbell, 1996).

### *c. Spatial Resolution Limitations*

Diffraction is another process involving electromagnetic radiation of concern in spectral remote sensing because of its importance in establishing the optical resolving power of remote sensors. W.G Rees, 1990, shows that the amplitude of the diffracted field in the case of Fraunhofer diffraction (far-field diffraction) for a circular aperture is given by Equation 2.8.

$$\text{Amplitude} = Q \frac{J_1(\overline{KD} \sin \theta_r / 2)}{(\overline{KD} \sin \theta_r / 2)} \quad [\text{Equation 2.8}]$$

$J_1$  = First order Bessel function

$\bar{K}$  = Wave number

$D$  = Diameter of circular aperture

$\theta_r$  = Radial angle

$Q$  = Proportionality Constant

Figure 2.6 illustrates the Fraunhofer diffraction geometry for a circular aperture. The locations of the zeros are computed using Equation 2.9.

$$\sin(\theta_r) = 1.22 \frac{\lambda}{D} \quad [\text{Equation 2.9}]$$

$\lambda$  = Wavelength

A useful criterion for establishing the spatial resolution limit is that the maxima of the amplitude produced by one object must just coincide with the first vanishing of the amplitude produced by the other object. The angular separation corresponding this diffraction limit or ultimate resolving power is defined by Equation 2.9.

In all optical systems diffraction sets the ultimate resolution limit, although it may not be responsible for the operational resolution limit. Limitations provided by other system factors can be more restrictive on resolution than diffraction. The resolution of an optical system is a combination of the performances of the lens and

the film (Rees, 1990). When a digital system is used, resolution is limited by the instantaneous field of view (IFOV).

The Modulation Transfer Function (MTF) is used to measure performances of lenses. The MTF for a given spatial frequency expresses the fraction of an incoming signal of that frequency that the detector outputs ("Figures of Merit").

## **B. SENSING THE EARTH'S SURFACE**

### **1. Radiation Propagation in the Atmosphere**

Radiation from the sun has to propagate through the atmosphere twice before being collected at a space borne sensor. Solar radiation is absorbed, scattered, and refracted twice before reaching the sensor. The extent of the atmosphere is about 100 *km* and Table 2.1 gives its gaseous composition.  $CO_2$  levels have become of particular concern.  $CO_2$  has strong absorption in the spectral region from 14  $\mu m$  to 17  $\mu m$ . This region covers a large portion of the earth's spectral emittance. Hence  $CO_2$  absorbs a large portion of the radiation emitted by the earth.

In addition to the gases in Table 2.1, the atmosphere contains water vapor, methane, and aerosols such as dust, volcanic ash, smoke, and pollen. The two main causes of attenuation in the atmosphere are molecular absorption by several minor constituents of the atmosphere and scattering due to aerosols (Seyrafi and Hovanessian, 1993). Figure 2.7 illustrates the spectral irradiance at the earth's surface and outside the earth's atmosphere. Take note of the regions defining atmospheric windows. Absorption is primarily due to electronic transitions in atoms and vibrational and rotational

transitions in molecules. As mentioned previously, these processes produce strong absorption in the visible, ultraviolet, and infrared regions.

Considering only the gases listed in Table 2.1, attenuation is dominated by Rayleigh scattering. Following Seyrafi and Hovanessian, 1993, Rayleigh scattering attenuation is computed using Equation 2.10.

$$I = I_o e^{-\sigma_m R} \quad [\text{Equation 2.10}]$$

$I_o$  = Original Radiation

$I$  = Scattered Radiation

$\sigma_m$  = Rayleigh scattering coefficient

$R$  = Path length

The Rayleigh cross section  $\sigma_r$  presented to an incident wave is defined so that the total power scattered by a gaseous molecule in all directions is equal to the power flowing across the cross section (Seyrafi and Hovanessian, 1993). This cross section is computed using Equation 2.11.

$$\sigma_r = \frac{8\pi^3 (n^2 - 1)}{3N^2 \lambda^4} \quad [\text{Equation 2.11}]$$

$n$  = Index of refraction of the gaseous medium

$N$  = Molecular number density

When considering only the aerosols, attenuation is dominated by Mie Scattering. Again following Seyrafi and Hovanessian, 1993, Mie scattering attenuation is computed using Equation 2.12.

$$I = I_o e^{-\sigma_a R} \text{ where } \sigma_a(h) = \frac{M(h)}{M(0)} \sigma_a(0) \quad [\text{Equation 2.12}]$$

$I_o$  = Intensity of original Radiation

$I$  = Intensity of scattered Radiation

$\sigma_m$  = Rayleigh scattering coefficient

$R$  = Path length

$M(h)$  = Aerosol number density at height  $h$

$\sigma_a(0)$  = Aerosol coefficient at sea level

Figure 2.8 gives a representative profile of the aerosol density versus altitude.

An accurate description of the combined effects atmospheric attenuations on radiation propagation is sufficiently complex to require computer models. Some widely used models include HITRAN and MODTRAN.

Refraction alters the direction of propagation of radiation as it travels from one medium to another with a different index of refraction. Snell's Law (Equation 2.13) involves the indices of refraction of both mediums describing this change in the direction of propagation. The index of refraction is defined as the ratio between the velocity of light in a vacuum ( $c$ ) to its velocity in the medium ( $c_n$ ) (Campbell, 1996). Equation 2.14 defines the index of refraction.

$$n \sin(\theta) = n' \sin(\theta') \quad [\text{Equation 2.13}]$$

$n, \theta$  = Index of refraction and incident angle of first medium

$n', \theta'$  = Index of refraction and transmission angle of second medium

$$n = \frac{c}{c_n} \quad [\text{Equation 2.14}]$$

$c_n$  = Speed of light in material with index of refraction  $n$

The index of refraction is a property of a medium and is determined by the way in which atoms respond to an electromagnetic wave. This response can be influenced by changes in the thermodynamic conditions imposed upon the medium, such as temperature and density. The atmosphere has layers of different compositions, temperatures, and densities making refraction a considerable effect in spectral remote sensing.

Atmospheric turbulence is characterized by random air motion. This motion causes random changes in the local index of refraction bending the radiation rays propagating through the atmosphere. It is the cause of phenomena such as the twinkling of stars at night, shimmering of distance objects on a hot day, and mirages (Seyrafi and Hovanessian, 1993). Temperature fluctuations have the greatest influence on the index of refraction fluctuations. Figure 2.9 very generally illustrates how large turbulent wind eddies can form to cause a radiation ray to wander.

The effects of atmospheric turbulence can be characterized as changes in the beam direction (beam wander), changes in the beam size (beam breathing), and intensity fluctuations (scintillation). These effects manifest themselves as motion, blur, and scintillation in the image. The single most important parameter that characterizes the effects of turbulence on radiative transfer is the atmospheric refractive index structure parameter,  $C_n^2$ .

$C_n^2$  is computed using Equation 2.15.

$$C_n^2 = [79 \times 10^{-6} \frac{P}{T}]^2 C_T^2 \quad [\text{Equation 2.15}]$$

$C_T^2$  = Temperature Structure Parameter

$P$  = Atmospheric pressure ( *mbar* )

$T$  = Temperature ( *K* )

Equation 2.16 is given by Hufnagel and Stanley, 1964, as an altitude-only dependent way to compute  $C_n^2$ .

$$C_n^2 = 4.2 \times 10^{-14} h^{\frac{1}{3}} e^{-\frac{H}{h_o}} \quad [\text{Equation 2.16}]$$

$H$  = Altitude above the ground (m)

$h_o$  = 3200m

Atmospheric turbulence can reduce the performance of optical imaging systems, particularly the system's resolution. A measure of the extent to which an optical system's performance has been reduced is called the optical transfer function. A model created by D.L Fried, 1966, for spherical waves is given by Equation 2.17. This equation is valid only for exposures taken over either a long (long term OTF) or short (short term OTF) time interval.

$$OTF = e^{-\{21.62 C_n^2 R \lambda^{-\frac{1}{3}} f_s^{\frac{5}{3}} [1 - A (\frac{f_s \lambda}{D_o})^{\frac{1}{3}}]\}} \quad [\text{Equation 2.17}]$$

$R$  = Path length

$\lambda$  = Wavelength of the radiation

$f_s$  = Angular spatial frequency

$D_o$  = Diameter of the aperture

$A = 0$  (Long term OTF),  $\frac{1}{2}$  (far-field short term OTF),  $1$  (near-field short term OTF)

## 2. Radiation Interacting With Surface Materials

Radiation interacts with surface materials through the processes of reflection, absorption, scattering, transmission, and fluorescence. If a surface is smooth, specular reflection occurs in which all or almost all incident radiation is reflected at the angle of incidence. If the surface is rough, diffuse reflection occurs in which all or almost all incident radiation is scattered in all possible directions of reflection. A perfectly diffuse reflector is often designated as a Lambertian surface (Campbell, 1996). Some materials

have a complex distribution of surfaces that receive incident radiation. These materials may produce specular reflection for radiation incident at one angle and diffuse reflection when radiation is incident at a different angle. A bi-directional reflectance distribution function (BRDF) is used to describe the complex reflection produced by a surface over all possible angles incidence and reflection.

Transmission occurs when incident radiation is transmitted through a material with little or no attenuation. The transmittance in the form of depth penetration of water is illustrated in Figure 2.4. Even though a material may reflect radiation of a particular wavelength, penetration depth may limit the extent to which it can reflect, thereby allowing more radiation to be transmitted. An example of this is plant leaves. Plant leaves reflect infrared radiation, but because of their thin structure the radiation does not penetrate long enough to be completely absorbed, resulting in significant amounts of infrared radiation passing through.

Fluorescence occurs when an object illuminated with radiation of one wavelength emits radiation of a different wavelength (Campbell, 1996). When examining remotely sensed data, one needs to be aware that there are some types of minerals and plants that fluoresce.

The combined effects of reflection, absorption, and transmission are defined in Equation 2.18.

$$E_I(\lambda) = E_R(\lambda) + E_A(\lambda) + E_T(\lambda) \quad [\text{Equation 2.18}]$$

$$E_I(\lambda) = \text{Incident Energy}$$

$$E_R(\lambda) = \text{Reflected Energy}$$

$$E_A(\lambda) = \text{Absorbed Energy}$$

$$E_T(\lambda) = \text{Transmitted Energy}$$

Equation 2.18 is simply the conservation of energy. Reflectance, transmittance, and absorptance are as previously defined.

THIS PAGE INTENTIONALLY LEFT BLANK

### **III. COLLECTING SPECTRAL INFORMATION**

#### **A. Remote Sensing Platforms**

##### **1. Altitudes of Operation**

As mentioned previously, spectral data is typically collected utilizing airborne or space borne sensors. This is because spectral data can be collected from large scenes at high altitudes. Airborne sensors are carried by aircraft and space borne sensors are carried by satellites, all of which operate at various altitudes. Operational altitudes in part determine spatial resolution and scale, and hence data utility. Varying the distance at which images are acquired allows different types of information to be extracted (Gibson, 2000). Figure 3.1 in Appendix A illustrates the various heights at which typical remote sensing devices operate.

##### **2. Airborne Sensors**

Airborne sensors basically consist of a camera mounted at some point on an aircraft. The camera may obtain images at an oblique angle to the vertical or at the vertical. These images typically have very good spatial resolution but extensive geometric distortions. The geometrical distortions often manifest themselves as changes in scale from one region in the image to another. Images taken at the vertical may be used to produce maps only after the images have been processed to get rid of geometrical errors.

Three types of cameras often used as airborne sensors are metric, strip, and panoramic cameras. Although these cameras vary in design, some of the basic components are the same.

***a. Camera Components***

In general, light enters the camera through the lens cone assembly, which contains the lens, filter, shutter, and diaphragm. Passing through the lens cone, light is filtered to the desired wavelength, focused, and cut for exposure time and space on film. A film magazine holds the film. It usually includes a supply spool, holding perhaps several hundred feet of unexposed aerial film, and a take-up spool to accept exposed film (Campbell, 1996). An electrical film drive device progresses the film. Cameras use filters to collect single wavelength band imagery.

***b. Strip Cameras***

In strip cameras the film is passed over a slit. The slit is analogous to a shutter that never closes from the start to the end of image collection. Images are not separated by frames. Once image collection is complete, the result is one long strip of imagery. Figure 3.2 illustrates this idea.

The speed of film movement as it passes the slit is coordinated with the speed and altitude of the aircraft to provide proper exposure (Campbell, 1996). Strip cameras provide good use for measuring long straight regions. Disadvantages include image distortion due to any change in the aircraft's motion.

*c. Panoramic Cameras*

Panoramic cameras use a rotating lens or prism to direct light to the film. It also uses a slit for film exposure, however the slit moves with a prism or lens across the film while the film is stationary. The film remains stationary during each sweep of the prism and lens. This process results in images consisting strips covering wide areas. Figure 3.3 illustrates this idea.

Disadvantages include image distortion due to forward motion of the aircraft and the side-to-side scan of the lens and prism. Panoramic photographs have serious geometric distortions that require correction before they can be used as the basis for measurements (Campbell, 1996). The principle advantages of the panoramic camera are its high image resolution and large area of coverage (Lillesand and Kiefer, 1987).

*d. Metric Cameras*

Metric cameras provide images with the least geometric errors. They are often referred to as mapping cameras. A low distortion lens system is held in a fixed position relative to the plane of the film (Lillesand Kiefer, 1987). Each time the shutter is opened, only one frame of imagery is obtained. An electronic system regulates how often the shutter opens.

*e. Image Distortions*

Images are primarily taken with the camera oriented with a vertical view of the ground. Three types of geometrical errors can be characterized as terrain, optical, and radial displacement errors. Optical distortions are caused by defects in the lens.

Radial displacement occurs when objects appear to lean outward from the central perspective of the camera lens (Campbell, 1996). Terrain errors are produced as changes in the elevation of a scene changes the scale.

A refining of lens making processes has made optical distortions insignificant. Terrain and radial errors are corrected in orthorectification or rubber sheeting. Rubber sheeting uses a mathematical model to adjust the image according to ground control points (GCP). Orthorectification is a procedure which models the viewing geometry of the sensor and account for distortions introduced by terrain relief ("Remote Sensing: Key Concepts"). This process involves scanning the image into a computer system, thereby digitizing it. A computer program then uses the image, with a map that illustrates the correct locations of figures in the image, to correct the image. In order for this transformation to be accurate, it is also necessary to input a digital elevation model, which stores the height of all the scanned pixels (Gibson, 2000). The result orthorectification is an image with scale variations removed. The x and y axes of the image are aligned with the east and north axes of the map projection being used, and each pixel in the image is geo-coded with its associated coordinate in the map projection ("Orthorectification: What, Why, How, Who?").

#### *f. Geographic Information Systems*

It is often convenient to use overlays to define or interpret an image. An overlay consists of image data of particular geographic qualities; for example vegetation classes or human development classes. Many overlays defining earth resources in a scene is called a Geographic Information System. Manual geographic information

systems usually comprise several data elements including maps, sheets of transparent materials used as overlays, aerial and ground photographs, statistical reports and field survey reports (Star and Estes, 1990). Overlays are able to be integrated into a single data set that can be analyzed using a computer.

## **2. Space borne Multispectral Scanning Systems**

Space borne Multispectral scanning systems (MSS) collect spectral information in two distinct ways. The first way, which is called traverse scanning, MSS use a rotating mirror to record a swath of ground perpendicular to the satellite's path. A telescope collects light and focuses it onto fiber-optic bundles that transmit the light to detectors. The light is then divided into a number of wavelength bands corresponding to the system's spectral resolution and sent to the detectors.

The instantaneous field of view (IFOV) of a scanning instrument can be defined as the ground area viewed by the sensor at a given instant in time (Campbell, 1996) The spatial resolution of the system sets the IFOV.

The second way in which the MSS collects spectral data is employing pushbroom scanning and using a Charged Coupled Imager (CCI) as a sensor. This system does not use a scanning mirror, but relies on quantum mechanical shifting that occurs within the CCI.

### ***a. Charge Coupled Imager***

A CCI consists of an array of Charge Coupled Devices (CCD's). Light entering the MSS is formed into a beam using lenses and is split into a number of spectral

regions with diffraction gratings or filters. Each CCD is made out of metal-oxide semiconductor materials and develops a quantum mechanical potential well. When light strikes the CCD a number of charges are generated proportional to the intensity of the light. The collected charges are shifted down the array and are converted to equivalent current or voltage at the output terminal (Karim, 1900). The shifting is controlled by a clock, allowing scanning to be done electronically. The CCD's are sensitive to the visible and near infrared regions. Responsivity, detectivity, and quantum efficiency are among various parameters used to quantify the performance of semiconductor sensors.

***b. Traverse and Pushbroom Scanning***

Figures 3.4 and 3.5 demonstrate the pushbroom and traverse scanning methods.

**3. Other Remote Sensing Systems**

In addition to the MSS, there are the Hyperspectral Scanning System (HSS) and the Ultraspectral Scanning System (USS). In these systems, spectral data is collected simultaneously from many narrower wavelength bands than in the MSS. Figure 3.4 illustrates the relative difference in the number and width of the wavelength bands in which each system operates.

**B. RESOLUTION**

There are four types of resolution of interest in remote sensing. They are spectral, temporal, radiometric, and spatial resolution. Spectral resolution is a measure of how

well a sensor can distinguish a material based on the sensor's number and widths of wavelength bands. High spectral resolution would be characteristic of a system using a large number of small wavelength bands. Temporal resolution is a measure of how often data can be obtained from the same area (Gibson, 2000). Spatial resolution is a measure of the smallest spatial length a material can possess to be resolved. Refer to Chapter II for detail regarding spatial resolution. Radiometric resolution measures the number of shades of gray a sensor can detect and applies only to digital systems. It is often expressed in *bits*. Equation 3.1 expresses this idea.

$$\text{Number of gray levels} = 2^{\text{Number of bits}} \quad [\text{Equation 3.1}]$$

THIS PAGE INTENTIONALLY LEFT BLANK

## **IV. MULTISPECTRAL DATA ANALYSIS TOOLS**

### **A. MULTISPECTRAL DATA**

Multispectral data can be imagined to be a number of registered two dimensional arrays of digital numbers. Each array corresponds to data in each spectral band, and the digital numbers are brightness values generated by the remote sensing system. Figure 4.1 illustrates this for remote sensing systems of different spectral resolutions.

Figure 4.2 illustrates the digital numbers that correspond to a pixel. Electronic sensors record digital numbers as bits in the binary number system. The number of brightness within a digital image is determined by the number of bits available (Campbell, 1996).

#### **1. Digital Images**

In a given band, the radiances of all materials covered by a pixel contribute to determining the pixel's digital number. A digital image is composed of an array of pixels, with each having one digital number per band.

When examining multispectral data on a video monitor, the digital data undergoes a complex process in which band brightness is corresponded with portions of the red, green, or blue projected on the screen by the monitor's electronics. It is often useful to examine images in true color or in false color. Using true color, the red, green, and blue bands of multispectral data are projected onto the video monitor in red, green, and blue respectively. Using false color, the red, infrared, and green bands are projected in green, red, and blue respectively. An analyst of multispectral data determines to use either a

true color or false color image based on how well the image distinguishes important features of a scene under investigation.

## **B. PRINCIPLE COMPONENTS ANALYSIS**

It is often very useful to plot pixels in digital number space. Digital number space is a multi-dimensional space in which each axis corresponds to each available band. Multispectral imagery tends to show high correlation between certain bands yielding information redundancy. A principle components analysis transformation (PCA) is performed on the data to remove this correlation. The PCA uses a variance-covariance matrix to calculate a coefficient matrix, which is applied to the brightness values of raw image pixels giving a decorrelation (Wilkie and Finn, 1996).

The PCA transform is a linear transformation that is also known as the Karhunen-Loève or Hotelling transform (Richards, 1995). Equation 4.1 illustrates the PCA transformation. Equation 4.1 gives the pixel sets before and after a PCA transformation. Figures 4.3a and 4.3b illustrates that the PCA transformation is simply a rotation in digital number space.

$$\bar{Y}_i = G\bar{X}_i \quad \text{[Equation 4.1]}$$

$\bar{Y}_i$  = Vector of principle component values of the  $i_{th}$  pixel

$G$  = Linear PCA transform

$\bar{X}_i$  = Vector of pixel points in original space

Figure 4.3b illustrates that the PCA transformation results in a number of PCA components. Each component can be represented as an image. The number of components produced by the transformation equals the number of bands in the raw data. The components possess a progressively smaller variance. The first three components of Landsat TM imagery will typically contain over 95% of the variance in all spectral bands (Wilkie and Finn, 1996). PCA components beyond the first few typically show the noise from the original data.

### **C. MULTISPECTRAL IMAGE CLASSIFICATION**

Informational classes are Regions of Interest to multispectral data users. These regions may be forests, areas of human development, or any other region to be analyzed. Spectral classes are groups of pixels that have similar spectral properties. When visualized in digital number space, spectral classes tend to form clusters. It is not uncommon to find several spectral classes within one informational class. For example, an informational class defined as forest may possess spectral classes of trees, soil, or even shaded areas. The goal of digital image classification is to assign pixels to classes in a region under investigation. Each pixel is compared to all others and those that belong to informational classes. Classification is performed using a computer that implements any one of a number of user specified algorithms. The two general classification schemes are Supervised and Unsupervised classification. This thesis will only present some detail regarding supervised classification; and detail regarding unsupervised classification may be found from (Rees, 1996) and others.

## **1. Supervised Classification**

Supervised classification is the process of assigning unidentified pixels to informational classes using training areas. Training areas are user defined samples of pixels with known identities. Although there are a number of specific algorithms for performing a supervised classification, this thesis will offer only a detailed description of the Spectral Angle Mapper and the Maximum Likelihood algorithms. For detail of other supervised classification algorithms see Campbell, (1996) and others.

### ***a. Maximum Likelihood***

The maximum likelihood algorithm is considered to be the most common supervised classification method (Richards, 1999). This classifier considers the relative likelihood that a pixel belongs to a particular class. Probabilities are computed from the estimated means and variances of the classes. A pixel is then assigned to the class that maximizes the probability. Since remotely sensed images contain classes that are most often impure, the maximum likelihood classifier provides the advantage of taking variations in brightness into consideration. Another advantage is that pixels can be classified even if they lie within an overlap region defined where frequency distributions of different classes overlap. Computation of the estimated probabilities is based on the assumption that both training data and the classes themselves display multivariate Gaussian frequency distributions (Campbell, 1996).

Before the classifier proceeds with the classification, the user may set probability thresholds. All pixels with computed probabilities below this threshold are unclassified. The results of this classifier are decision rules and a classified image. A

decision rule is created for each class. It consists of an image that conveys the computed probabilities for all pixels. This may be a grayscale image such that black and white represents zero and unity probabilities respectively. The classified image consists of a number of uniform patches identified by a particular color that associates each patch with a class.

***b. Spectral Angle Mapper***

The spectral angle mapper (SAM) classifies pixels based on their spectral similarity to reference spectra or 'end member' spectra. A computer with appropriate software computes spectral similarity by treating pixels as vectors in digital number space. This space is consequently band intensity space. A vector can be created by establishing its tail at the origin and terminating at its representative pixel. The length of the vector's projection onto a particular band's axis corresponds to the pixel's brightness in that band.

The SAM determines spectral similarity by computing the angle (spectral angle) between vectors that represent the reference spectrum and the unclassified scene spectrum. Figure 4.4 illustrates the idea of spectral angle.

When the reference spectrum and the unclassified scene spectrum are composed of many pixels, Equation 4.3 is used to compute the spectral angle.

$$\alpha = \cos^{-1} \left( \frac{\sum_{i=1}^N t_i r_i}{\left( \sum_{i=1}^N t_i^2 \right)^{\frac{1}{2}} \left( \sum_{i=1}^N r_i^2 \right)^{\frac{1}{2}}} \right) \quad [\text{Equation 4.3}]$$

$\alpha$  = Spectral angle

$t_i$  = Unclassified scene spectrum

$r_i$  = Reference spectra vector components

$\overline{N}$  = Number of bands of data

Take note that  $\alpha$  is independent of vector length. This means that the SAM does not consider pixel brightness. This allows comparison between library spectra and the spectra of target pixels even with incomplete knowledge of the illumination characteristics of the target pixel spectra (Kruse, 1993).

In the same likeness as the maximum likelihood classifier, with the SAM the user can input a spectral angle threshold. The computed values of  $\alpha$  can be directly translated to the 0-255 scale for display purposes (Mather, 1999). The output of the SAM is a classified image and a number of decision rules that equals the number of endmembers. The decision rules may be grayscale images, such that black and white represents large and small angular deviations from the reference spectrum vector respectively. The classified image consists of a number of uniform patches identified by a particular color that associates each patch with a class.

#### **D. Accuracy Assessment**

In order to evaluate the accuracy of the classification process, the software tool computes a confusion matrix. The confusion matrix is a labeled table illustrating the results of a comparison between a reference image and a classified image. Comparisons are made on a pixel-by-pixel basis. The confusion matrix gives two kinds

of errors for each informational class. They are called omission and commission errors. Omission errors quantify the portion of pixels in a particular reference class that the classifier assigned to other classes. Commission errors occur when a particular class in the classified image is incorrectly assigned pixels from other classes.

The confusion matrix also expresses consumer and user accuracy. Producer accuracy quantifies the portion of pixels from a particular reference class that were classified as belonging to that same class. Consumer accuracy is the ratio of correctly classified pixels assigned to a particular class to the total number of pixels classified (correctly and incorrectly) as that class.

A percent correct and a coefficient of agreement, Kappa, are additional parameters computed in the confusion matrix. Kappa measures the agreement, beyond chance, between two maps, taking into account all pixels of an image (Wilkie and Finn, 1996). The confusion matrix is a square matrix with rows corresponding to reference classes and columns corresponding to classified image classes. Percentage correct is the percentage ratio of the number of pixels correctly classified to the number of pixels examined. Percentage correct may be given for each class and for the overall classification. Since the confusion matrix is a square matrix, number of pixels correctly classified is the sum of the diagonal elements. Kappa expresses the agreement between two images. Equations 4.4, 4.5, and 4.6 show how elements of the confusion matrix are computed.

$$\text{Total percentage Correct} = \frac{\sum_{i=1}^c e_{ii}}{P} \quad [\text{Equation 4.4}]$$

$e_{ii}$  = Confusion matrix elements

$\bar{P}$  = Total number of pixels

$\bar{c}$  = Number of classes

$$\text{Class percentage correct} = \frac{e_{ii}}{\sum_{j=1}^{\bar{c}} e_{ij}} \quad [\text{Equation 4.5}]$$

$$\text{Kappa} = \frac{\sum_{i=1}^{\bar{c}} p_{ii} - \sum_{i,j=1}^{\bar{c}} [p(x_i)p(y_i)]}{1 - \sum_{i,j=1}^{\bar{c}} [p(x_i)p(y_i)]} \quad [\text{Equation 4.6}]$$

$p_{ij}$  = The probability of the  $i_{th}$  pixel in image  $x$  being the  $j_{th}$  pixel in image  $y$

$$\sum_{i=1}^{\bar{c}} p_{ii} = \text{The percentage correct}$$

## **V. LANDSAT 7 AND IKONOS**

### **A. OPERATIONAL DIFFERENCES**

The output of the Ikonos and Landsat 7 satellite systems differ in spatial and spectral resolution. Ikonos provides 4-meter 4-band multispectral and 1-meter panchromatic imagery. Landsat 7 provides 30-meter multispectral (bands 1-5 and 7), 15-meter panchromatic (band 8), and 60-meter thermal (band 6) imagery.

### **B. LANDSAT 7**

#### **1. Enhanced Thematic Mapper Plus (ETM+)**

Landsat 7 was built by Lockheed Martin Missiles and Space and was launched on April 15, 1999. It is the most recently successfully launched satellite in the Landsat series. Landsat 7 uses the Enhanced Thematic Mapper Plus (ETM+) sensor, built by Raytheon Santa Barbara Remote Sensing, to measure radiation reflected or emitted from the earth. The sensor measures radiation in eight bands and produces better resolution in the thermal infrared than the Thematic Mapper(TM) sensor onboard Landsat 4 and 5. The eight bands detect radiation in the visible, near infrared, short-wave, and thermal infrared regions of the electromagnetic spectrum.

The ETM+ collects radiation using a scanning mirror that sweeps across the direction of travel. A telescope focuses the radiation into compensation mirrors, which then sends it to the focal planes. Compensation mirrors are used to correct for scan lines. Scan lines is the compound effect of along-track orbital motion and cross-track scanning which leads to significant overlap and underlap in ground coverage between successive

scans (SDUH). The energy is then partitioned. Some of the partitioned energy is sent to the silicon detectors for bands 1-4 and 8. The rest of the energy is sent to a cold focal plane (maintained at  $91\text{ K}$ ) that contains the detectors for bands 7, 5, and 6.

## **2. Orbit**

Landsat 7 operates in a sun synchronous orbit at an altitude of  $705\text{ km}$ . This allows it to pass over the same point on earth at essentially the same local time every 16 days (SDUM). However the sun's elevation angle may change significantly over this time. The production of a useful image requires consideration of dependencies of material reflectances and atmospheric effects on the sun's elevation angle. The elevation angle made between a plane tangent to the earth's surface and a line leading to the sun. Landsat 7 is positioned perpendicular to this tangent plane. Images can be produced most efficiently at sun elevation angles above  $30^\circ$  and a low angle limit has been set at  $15^\circ$ .

## **3. Radiometric Calibration and Relative Spectral Response**

Two spherical integrating sources were used to calibrate the ETM+ prior to launch (SDUH). These devices consist of a hollow sphere that has a small hole and a uniformly coated inner surface. A radiation source is placed inside the sphere. Radiation exits the sphere through the small hole in a random orientation and provides a radiance spectrum covering the entire range of the detector. Following SDUH, calibration reduction on all bands except band 6 was performed using Equations 5.1 and 5.2.

$$L_{\lambda}(b,s) = \frac{\int RSR(b,\lambda)L_{\lambda}(s,\lambda)d\lambda}{\int RSR(b,\lambda)d\lambda} \quad [\text{Equation 5.1}]$$

$L_{\lambda}(b,s)$  = Band Weighted Spectral Radiances for band  $b$  and sphere level  $s$

$RSR(b,\lambda)$  = Relative Spectral Response from band  $b$  at  $\lambda$

$L_{\lambda}(s,\lambda)$  = Measured Spectral Radiance of Sphere level  $s$  at  $\lambda$

$$Q(d,b,s) = G(d,b)L_{\lambda}(b,s) + B(d,b) \quad [\text{Equation 5.2}]$$

$Q(b,d,s)$  = Quantized detector responses

$G(d,b)$  = Gains

$B(d,b)$  = Biases

In Equation 5.2,  $Q(d,b,s)$  is regressed against  $L_{\lambda}(b,s)$ .

Band 6 is the thermal band. In calibration it is matched with the Thematic Mapper Calibrator (TMC), which uses selectable blackbody sources. Also since the ETM+ itself is a producer of thermal radiation, following SDUH contributions of this thermal radiation to calibration is modeled using Equation 5.3.

$$Q_{sc} - Q_{sh}(d) = G(d)(L_{\lambda,sc} - L_{\lambda,esh}) \quad [\text{Equation 5.3}]$$

$$L_{\lambda,esh} = L_{sh} + \sum a_j(L_{sh} - L_j)$$

$Q_{sc}(d)$  = Quantized Response of Band 6 at detector  $d$  to the scene

$Q_{sh}(d)$  = Quantized Response of Band 6 at detector  $d$  to the shutter

$G(d)$  = Gain of the Detector

$L_{\lambda,sc}$  = Spectral Radiance of the scene

$L_{\lambda,esh}$  = Scene-Equivalent Spectral Blackbody Radiance of the Shutter

$L_{sh}$  = Blackbody Radiance of the Shutter

$L_j$  = Blackbody Radiance of the  $j_{th}$  component of the ETM+

$a_j$  = Emissivity adjusted view factor for the  $j_{th}$  component of the ETM+

Under operation calibration is performed periodically with three onboard calibration devices. They are the Internal Calibrator (IC), the Partial Aperture Solar Calibrator (PASC), and the Full Aperture Solar Calibrator (FASC). The IC is useful for calibrating all ETM+ bands, while the PASC and FASC are mainly useful for the reflective bands (SDUH). The IC consists of two tungsten lamps as blackbody sources. The FASC consists of a white panel that can be positioned in front of the ETM+ aperture. The white panel diffusely reflects radiation into the ETM+ full aperture. With known surface reflectance, solar irradiance and geometry conditions, this device behaves as an independent, full aperture calibrator (SDUH). The PASC allows the ETM+ to image the sun while viewing a 'dark earth'. The PASC is attached to the ETM+ sun shade obscuring a small portion of the aperture. Figures 5.1-8 illustrate the spectral responses of the ETM+ eight bands.

The ETM+ has 8 *bit* radiometric resolution. This is optimized by adjusting the gain state. The gain is adjusted to low or high for high or low surface brightness respectively. Figure 5.9 illustrates this.

Figure 5.10 illustrates the relative location of the ETM+ onboard the Landsat 7.

## **C. IKONOS**

Ikonos was built by Lockheed Martin Commercial Space Systems for Space Imaging and was launched in September 1999. For two years it had the highest commercially available spatial resolution of 1 meter panchromatic and 4 meter 4 band multispectral. It has a nominal swath width of 11 *km* at nadir (sensing vertically downward) allowing for enhanced revisit rate and stereo capabilities. The sensor was built by Eastman Kodak Company.

### **1. Sensor System**

The sensor system consists of an optical telescope assembly, a focal plane unit, a digital processing unit, and a power supply unit. The camera telescope has the equivalent resolving power of a 10,000 *mm* telephoto lens ("Figures of Merit"). It consists of five curved mirrors and two flat mirrors that allow for a reduced telescope length while focusing radiation onto the focal plane. The primary mirror has a honeycomb glass core covered with a thin highly polished mirror.

The focal plane unit contains the sensor arrays. The sensor arrays consist of separate CCD arrays for simultaneously collecting panchromatic and multispectral imagery. Filters are used to isolate the red, green, blue, and near infrared portion of the

collected radiation. The digital data from the CCD array electronics is eventually compressed in the digital processing unit. The digital processing unit compresses the digital image files from 11 *bits* per pixel (*bbp*) data to an average value of 2.6 *bbp* at a speed of 115 million pixels per second ("Figures of Merit").

The Power supply system uses hybrid DC-DC converters and electronic filters to convert high voltage direct current (DC) to a relatively low voltage DC. The low voltage DC is used to power the camera's sub-systems. Total camera power consumption is 350 *watts*. Figure 5.11 in Appendix A provides additional specifications for the Ikonos system.

## **2. Radiometric Calibration and Relative Spectral Response**

### ***a. Relative Spectral Response***

Ikonos spectral band characteristics are given in Table 5.1 on the following page.

Figures 5.12 and 5.13 illustrate the relative spectral responses for panchromatic and 4-band multispectral sensing.

The Ikonos spectral responses were determined analytically by combining the spectral reflectivity data of optical witness samples and the measures net quantum efficiency of the spectral filter/detector assemblies (Space Imaging). Equation 5.4 is integrated over the wavelength interval of 350-1035 *nm* for computing Ikonos in-band radiance.

$$L_k = \int L(\lambda)R'_k(\lambda)d\lambda \quad [\text{Equation 5.4}]$$

$L_k$  = In-band radiance at the sensor aperture for spectral band  $k$

$L(\lambda)$  = Spectral radiance at the sensor aperture

$R'_k(\lambda)$  = Peak-normalized spectral response for spectral band  $k$

Ikonos imagery is calibrated to at-aperture in-band radiance by rescaling its transmitted data. The DN values are converted to in-band radiance with Equation 5.5 and the calibration coefficients from Table 5.2.

$$L_{i,j,k} = DN_{i,j,k} * [CalCoef_k]^{-1} \quad [\text{Equation 5.5}]$$

$i, j, k$  = Indices representing image pixel  $i, j$  in spectral band  $k$

$L_{i,j,k}$  = In-band radiance at the sensor aperture for pixel  $i, j$  in spectral band  $k$

$CalCoef_k$  = In-band radiance calibration coefficient for spectral band  $k$

$DN_{i,j,k}$  = Image product digital numbers pixel  $i, j$  for spectral band  $k$

The calibration coefficients for each spectral band  $k$  were computed using Equation 5.6 (Proc. SPIE Vol. 4381).

$$CalCoef_k = G_k^{-1} A_{opt} \Omega_k \int L(\lambda) \bar{R}_k(\lambda) L_k^{-1} d\lambda \quad [\text{Equation 5.6}]$$

$G_k$  = Gain Coefficient for spectral band  $k$

$\bar{A}_{opt}$  = Clear aperture area of the Ikonos telescope

$\Omega_k$  = Ikonos IFOV in spectral band  $k$

$L_k$  = In-band solar radiance at the sensor aperture for spectral band

$k$

$L(\lambda)$  = Solar spectral irradiance at the sensor aperture

$\bar{R}_k(\lambda)$  = Spectral responsivity for spectral band  $k$

$\lambda$  = Wavelength

## **VI. MULTISPECTRAL ANALYSIS**

### **A. DESCRIPTION OF THE STUDY AREA**

This thesis examined the Elkhorn Slough and its surrounding wetlands. The Elkhorn Slough (ES) sits on the central California coast about 100 *miles* south of San Francisco (Silberstein and Campbell, 1989). Its waterway is a narrow winding body that measures 700 *ft* wide and 25 *ft* deep at its mouth in the town of Moss Landing. The ES is supplied freshwater from winter rains and salt water from the sea. It is composed of a number of habitats including the waterway, mudflats, salt marsh, and the uplands, which mainly consists of taller plants.

Local industry includes National Refractories, which produce heat-resistant bricks by extracting magnesium from seawater, and Pacific Gas and Electric, which produces electricity. Conservation of the ES is currently being undertaken by the Elkhorn Slough Foundation (ESF).

### **B. COLLECTING DATA**

Ikonos satellite imagery of the ES its surrounding wetlands was collected for October 23, 2000. The other input for the study was a classification map provided by the ESF. The vector map defined geo-referenced polygons that define qualitative attributes of the primary regions-of-interest (ROIs). The vector format file was in standard ARCVIEW shape file format. The map was the product of a compilation of information from aerial photos and Global Positioning System (GPS) assisted field observations. The ESF used a 50% thumb rule to qualitatively define each ROI. The thumb rule stated that

each region was defined to be the material which comprised at least 50% of it. Tables 6.1 and 6.2 in Appendix B provides the nomenclature for the ROIs.

### **C. PROCESSING THE DATA**

The bulk of the analysis time was spent resolving the ROIs derived from the above noted class map. A fairly standard process was used in the Environment for Visualizing Images (ENVI). A Principle Components (PC) transform was applied to the four band data, which facilitated visualizing the data.

The primary problem with the initial set of ROIs was that most reflected a significant mixture of regions (e.g. soil and vegetation), and these needed to be resolved or purified.

### **D. TRAINING DATA**

In order to use the ROIs as training data for the classification process, it was necessary to refine the ROIs spectrally to ensure that each ROI's spectral information uniquely defined it. Analysis of the true and false color images and using ENVI's N-Dimensional Visualizer (NDV) provided the means to refine the spectral data.

The NDV produces a color-coded plot of pixels in Digital Number (DN) space and allows user directed or automated rotation of user perspective through various dimensions. The NDV displays a two dimensional slice of DN space at a time. The DN space had four dimensions, one for each spectral band of the Ikonos imagery, or three dimensions in PC space. The NDV also affords the user the ability to color code pixels during visualization and to export these color-coded pixels back and forth between the

NDV and the image. This is useful for isolating pixels during visualization and for providing a convenient way to link spectral and spatial information.

In the first step of the refinement process, all ROIs were individually analyzed with the NDV using the raw data and the PCA transformed data. This was awkward because of the large number of pixels, and a lack of well defined clusters in DN space. This was addressed by defining small ROIs which could be used as reference classes. The reference classes were obtained by defining spectrally pure field vegetation, sand, soil, trees, concrete, and water. Also a shade test region was created for calibration of the NDV, and for providing a means for determining the direction of increasing brightness once rotation in DN space has started. Figure 6.1 illustrates the reference spectra in DN space. Although the axes are not seen, the horizontal axis is the near infrared band and the vertical axis is the green band. A third band, which is also unseen, is perpendicular to this page; it is the red band. Each ROI and the test regions were then simultaneously visualized with the NDV. Figure 6.2 shows the test regions and the Eucalyptus ROI in the NDV. Figure 6.2 has the same band dimensions as Figure 6.1.

Reference classes that are undesirable to include in the training data for a particular ROI, are termed excludable. After rotation through all dimensions, all pixels collocated with and in sufficiently close proximity to excludable reference classes were color-coded white. Color coding pixels white means that when classes are exported from the NDV to the image, white classes are excluded from exportation. The result of this process was a new set of secondary ROIs that was made more spectrally pure by eliminating excludable sub-classes.

In the second step of the refinement process, the objective was to ensure that the first step did not exclude too much of the primary ROI data. Excluding too much of the primary ROI data could produce training data that underestimated the variation and overestimated the distinctiveness of the region it was supposed to represent. The secondary ROIs were again individually analyzed with the NDV using the raw data and the PCA transformed data. The secondary ROIs were repeatedly exported to and from the NDV and a false or true color image.

## **E. CLASSIFICATION**

### **1. Spectral Angle Mapper**

The SAM was applied to the raw data using various angular thresholds. The SAM used both the refined and unrefined ROIs individually as training data. The angular thresholds used were 0.075, 0.100, 0.150, 0.250, and 0.300 radians. A classified image and a set of rule images were produced for each angular threshold.

### **2. Maximum Likelihood**

The maximum likelihood classifier (MAXL) was applied to the raw data using various probability thresholds. The MAXL used both the refined and unrefined ROIs as training data. The probability thresholds were 90% and 85%. A set of rule images, one for each region, and a classified image was produced for each probability threshold.

## F. CONFUSION MATRIX

A confusion matrix was computed using the ENVI result for all classified images using various combinations of the refined and unrefined training data as ground truth data. Tables 6.2a-f and 6.3a-f provide the confusion matrices for the SAM and MAXL at 0.250 radians and 85% threshold respectively. The refined data was used as training and the unrefined data was used as ground truth data. Table 6.1 in the next section should be referred to for illustration of the various combinations.

## G. RESULTS

Table 6.1 illustrates the results of the various classification schemes and confusion matrix computation schemes.

Classification Scheme	Threshold	Ground Truth Data	Training Data	Overall Accuracy
SAM	0.075 Radians	Refined	Refined	15.25%
SAM	0.100 Radians	Refined	Refined	16.59%
SAM	0.150 Radians	Refined	Refined	17.12%
SAM	0.250 Radians	Refined	Refined	29.78%
SAM	0.250 Radians	Unrefined	Refined	17.16%
SAM	0.250 Radians	Unrefined	Unrefined	10.70%
SAM	0.300 Radians	Refined	Refined	17.16%
MAXL	85%	Refined	Refined	14.27%
MAXL	85%	Unrefined	Refined	8.22%
MAXL	85%	Unrefined	Unrefined	3.71%
MAXL	90%	Refined	Refined	6.40%

Table 6.1 Results of Classification Schemes

The overall accuracies for all classification schemes were low. Generally there was a marked difference between the results produced by the two classification schemes. Overall the SAM produced classification results in closer agreement to the ESF class

map. However, from visual inspection, the rule images produced by the MAXL provide superior utility for informational reference. For most of the rule images, the MAXL resulted in far more suppression of regions that did not belong to the rule's class than did the SAM. The classified images for the SAM at 0.250 and the MAXL at 85%, using the refined data as training data and ground truth data, produced the best results and are presented in Figure 6.44 and Figure 6.43 respectively. In comparing the overall accuracy of the SAM at 0.250 radians threshold, using the refined data versus the unrefined data for both training and ground truth data, the refining process was responsible for a 278.31% magnification in accuracy. Similarly, the refining process using the MAXL at 85% probability threshold resulted in a 384.63% magnification in accuracy.

Figures 6.41 and 6.42 are the true and false color images respectively. Figures 6.3-21 and 6.22-40 provide the rule images for the SAM at 0.250 radians threshold and MAXL at 85% probability threshold respectively.

## **VII. SUMMARY AND CONCLUSION**

The Ikonos satellite was used to collect high spatial resolution multispectral imagery of the Elkhorn Slough was collected on October 23, 2001. Training data was obtained from the Elkhorn Slough Foundation. A rigorous spectral refining process was applied to the raw and PCA transformed data. The effectiveness of using the training data for scene classification was analyzed by applying the Spectral Angle Mapper and the Maximum Likelihood classifiers. Thresholds were varied, and the classifiers used both the refined and unrefined training data separately. Confusion matrices were computed using various combinations of refined and unrefined data as training data and/or ground truth data.

Table 6.1 from the previous chapter demonstrated the effectiveness of using high resolution 4-band multispectral data to perform supervised scene classification as asserted in Chapter I. Although overall accuracy was low using all classification schemes, other results were promising. The results indicated that up to a 385% improvement in accuracy can be achieved using the spectral refining process described in Chapter VI. The 385% improvement represents the amplification of accuracy as a percentage. The Maximum Likelihood classification result produced the least overall accuracy.

The nature of the data provided by the Elkhorn Slough Foundation was in part responsible for the low overall accuracies. Some Regions-of-Interest were very large and too spectrally diverse to produce high classification accuracy. For example, reducing the number of spectral sub-classes in the Tidal Wetland region as far as possible without loosing its overall spectral identity still resulted in Tidal Wetland being too spectrally

diverse. A similar effect occurred with some other regions. Low accuracies also come as a result of the thumb rule the Elkhorn Slough Foundation used to define their Regions-of-Interest. This thumb rule unavoidably produced a large number of heterogeneities in most Regions-of-Interest.

## APPENDIX A. GENERAL FIGURES AND TABLES

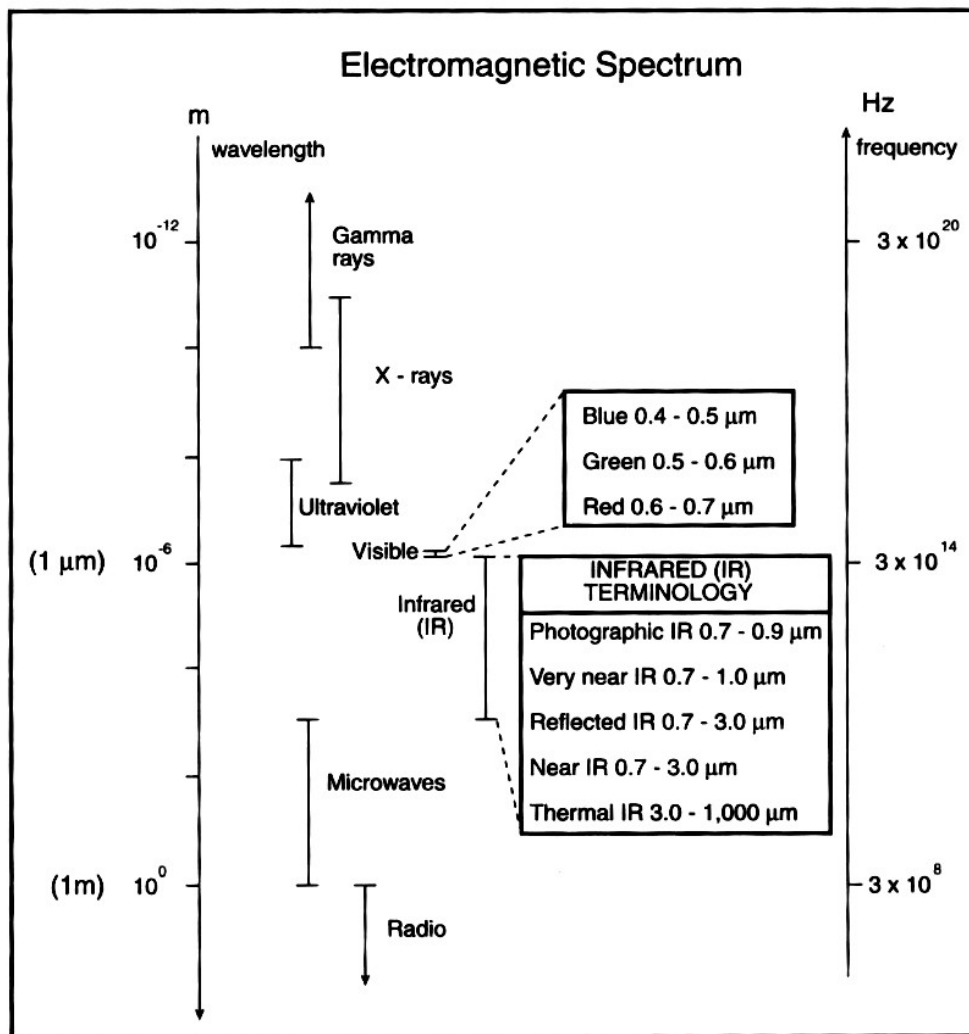


Fig. 2.1 The Electromagnetic Spectrum (Gibson, 2000)

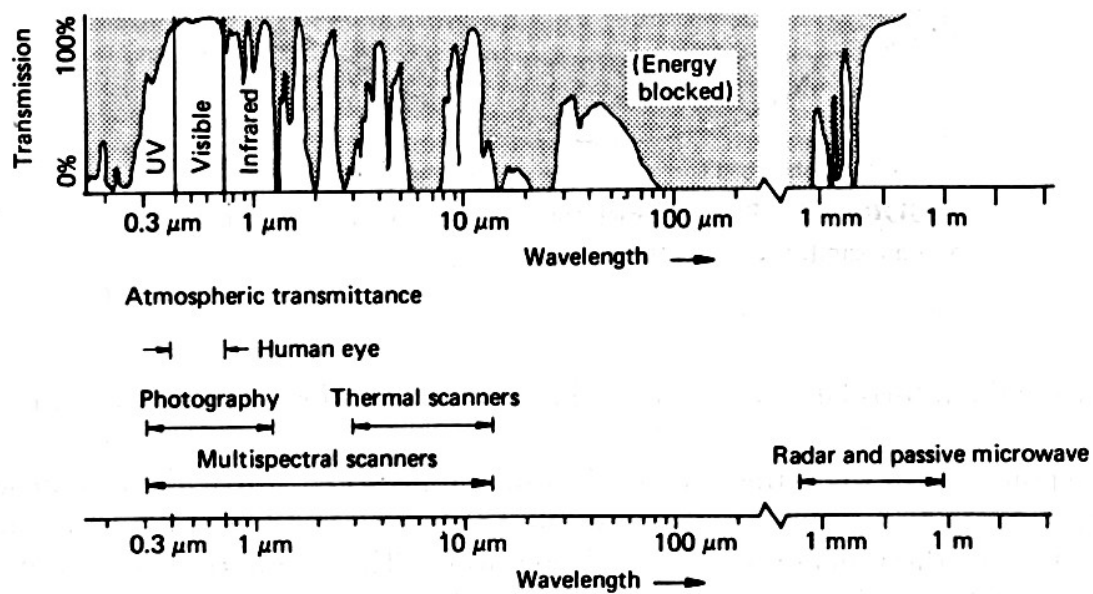


Fig. 2.2 Atmospheric Windows (Lillesand and Kiefer, 1979)

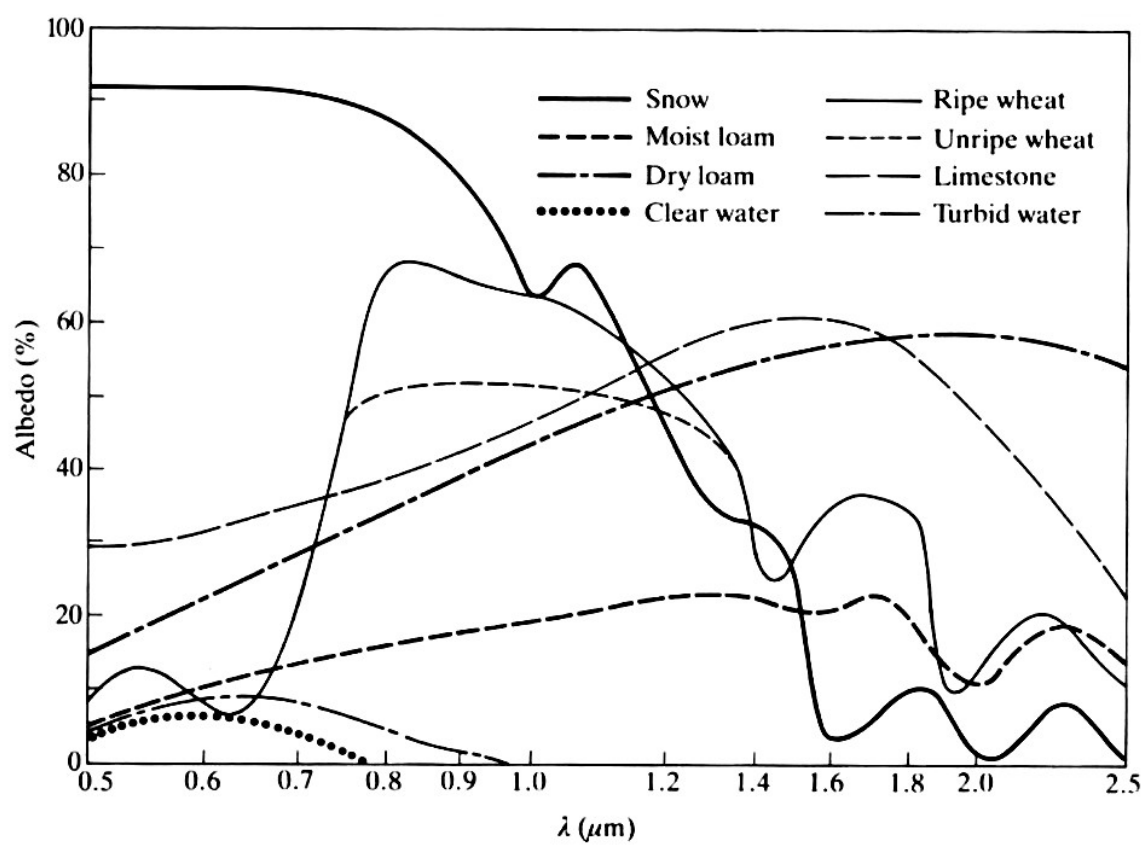


Fig. 2.3 Spectral Albedos (Rees, 1990)

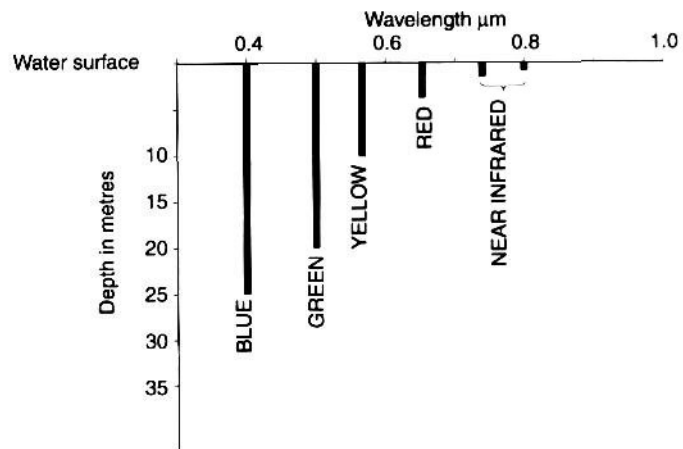


Fig. 2.4 Depth Penetration of radiation into Clear Water (Gibson, 2000)

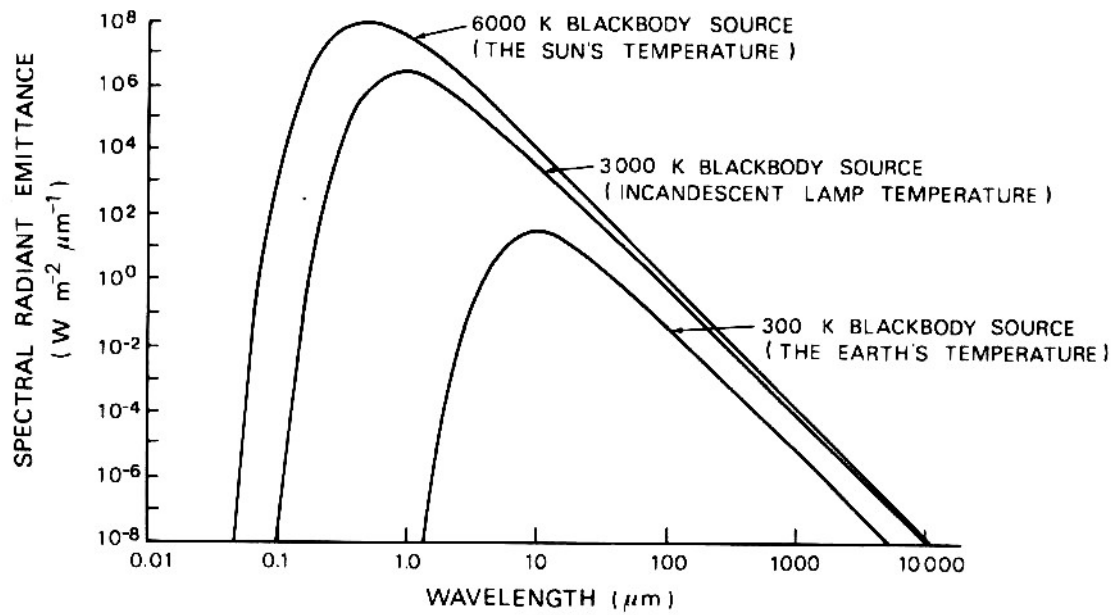


Fig. 2.5 Spectral Emittance of Three Black Body Sources (Lo, 1986)

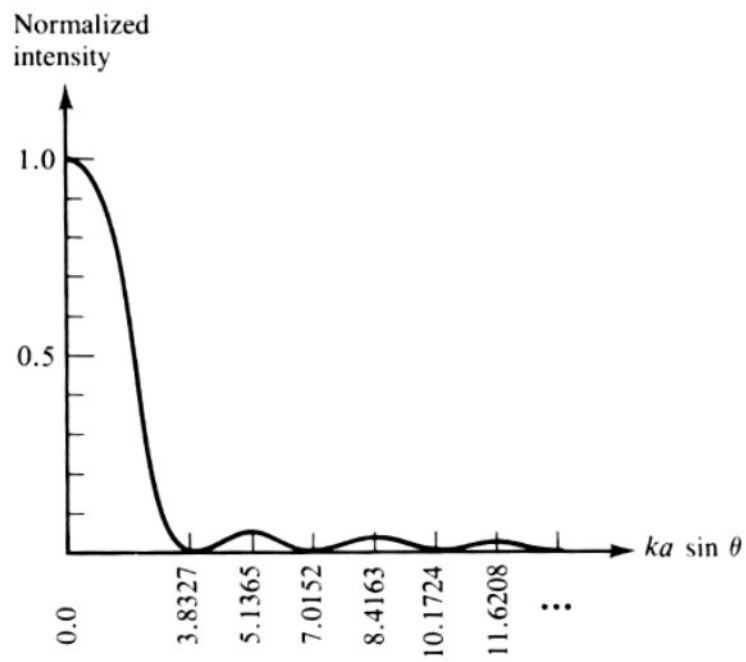


Fig. 2.6 Fraunhofer Diffraction Pattern for Circular Aperture (Karim, 1990)

<i>Component</i>	<i>Percentage</i>
N <sub>2</sub>	78.08
O <sub>2</sub>	20.94
Ar	0.93
CO <sub>2</sub>	0.0314
O <sub>3</sub>	0.00000004

Table 2.1 Gaseous Components of the Atmosphere (Gibson, 2000)

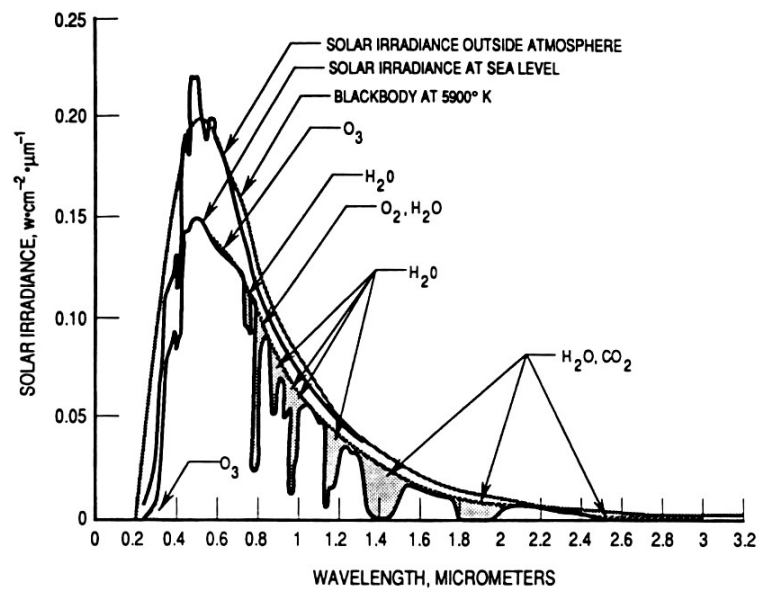


Fig. 2.7 Solar Irradiance With Atmospheric Gas Attenuation (Seyrafi and Hovanessian, 1993)

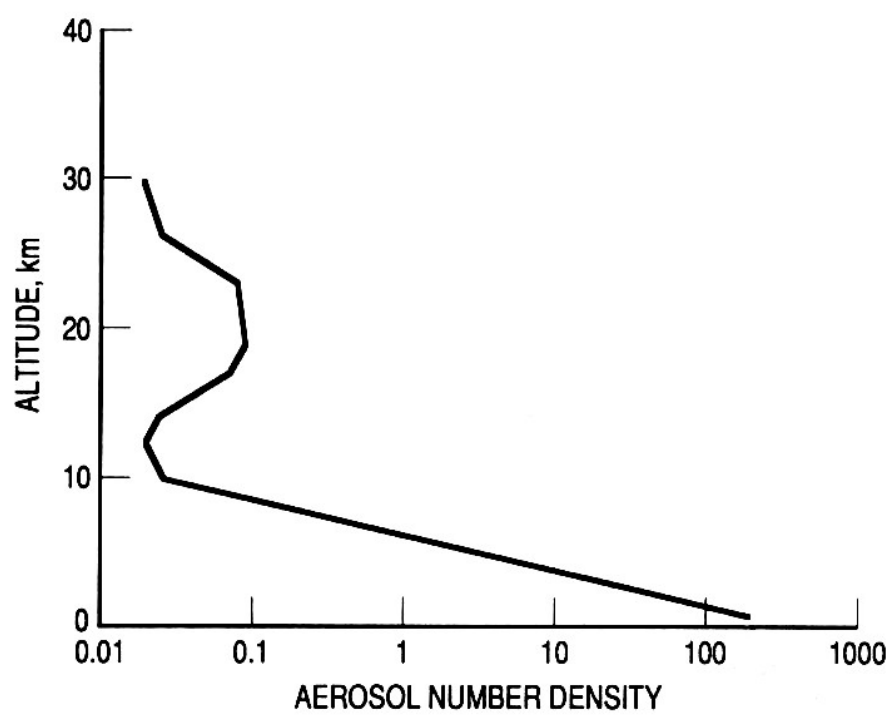


Fig. 2.8 Aerosol Number Density (Seyrafi and Hovanessian, 1993)

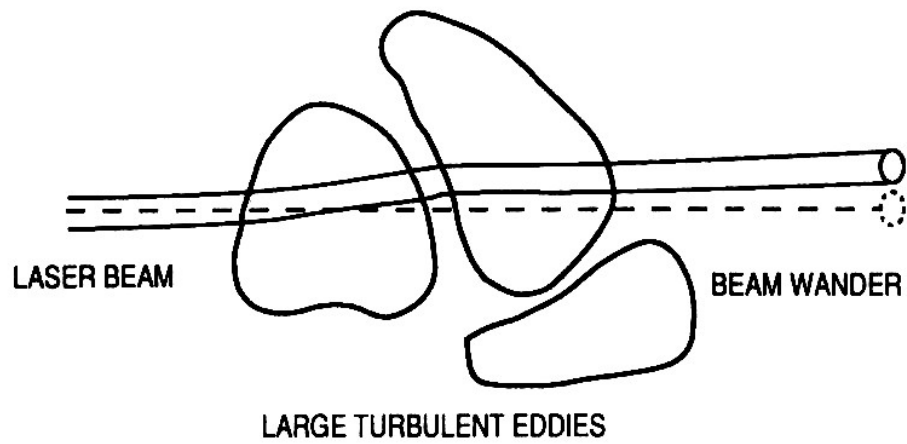


Fig. 2.9 Beam Wander of a ray of Radiation caused by Turbulence (Seyrafi and Hovanessian, 1993)

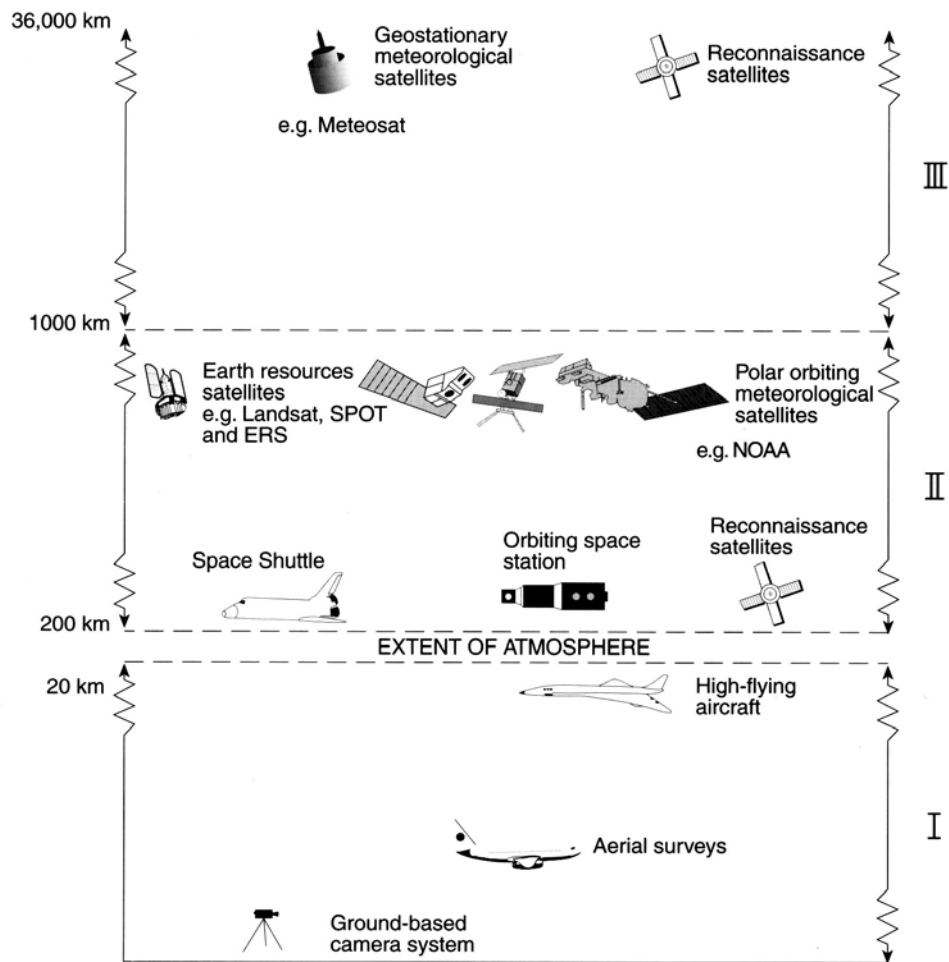


Fig. 3.1 Operational Altitudes of various remote sensing systems (Gibson, 2000)

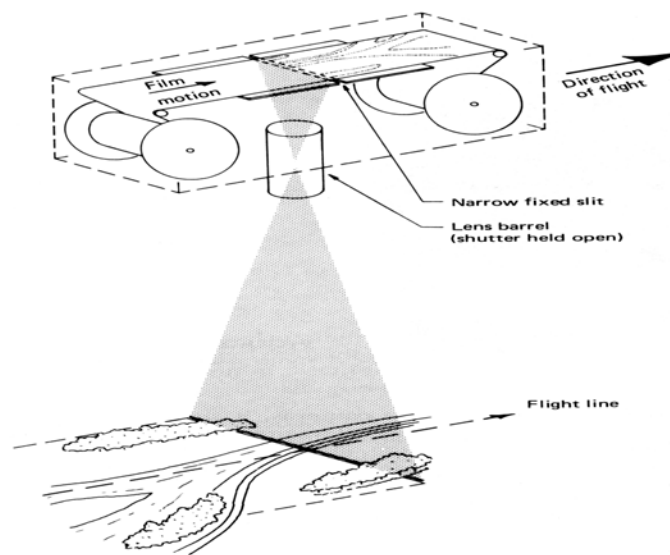


Fig. 3.2 Strip Camera Image Collection (Lillesand and Kiefer, 1987)

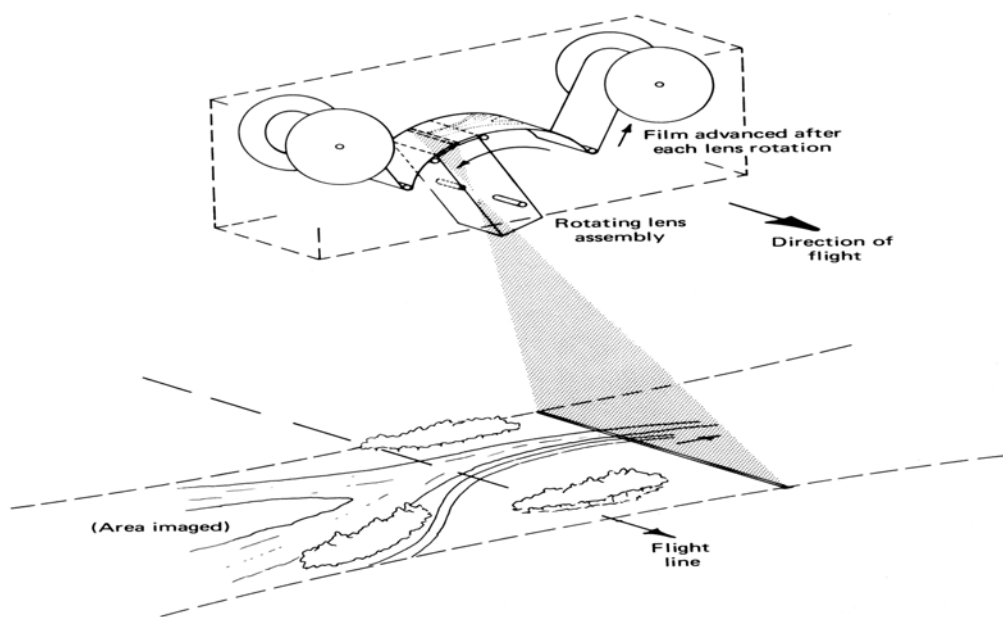


Fig. 3.3 Panoramic Camera Image Collection (Lillesand and Kiefer, 1987)

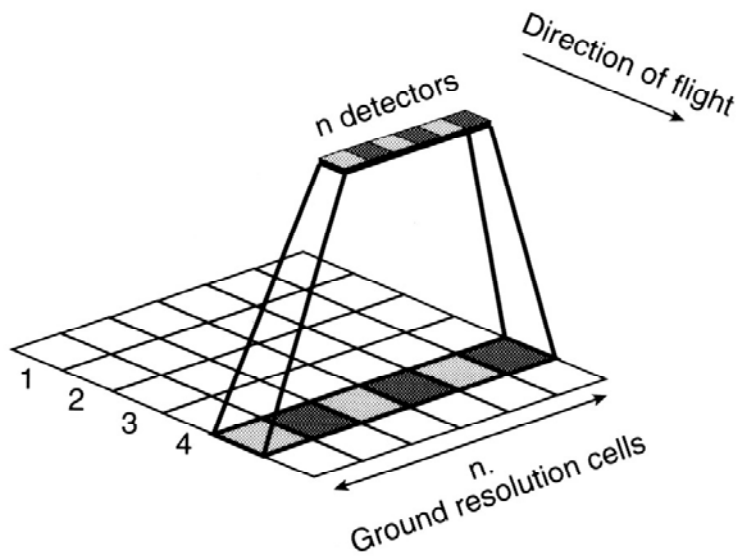


Fig. 3.4 Pushbroom Scanning (Gibson, 2000)

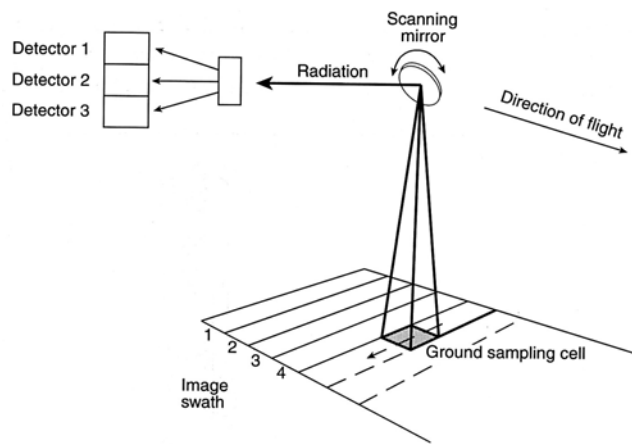


Fig. 3.5 Traverse Scanning (Gibson, 2000)

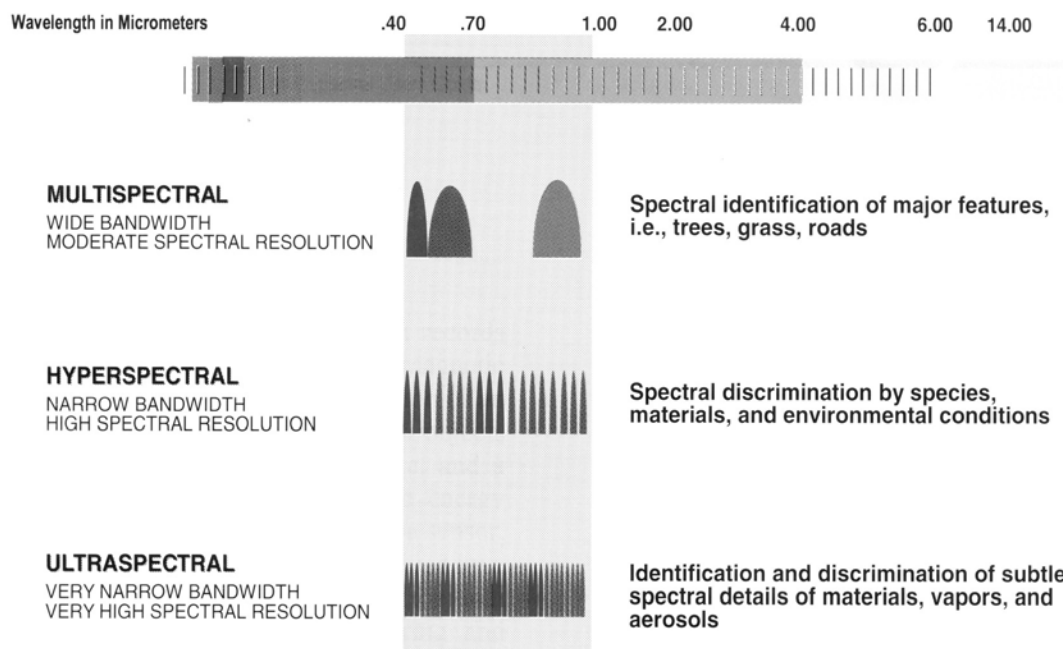


Fig. 3.4 Relative Difference in Spectral Resolution among Spectral Scanning Systems (Multispectral User's Guide, 1995)

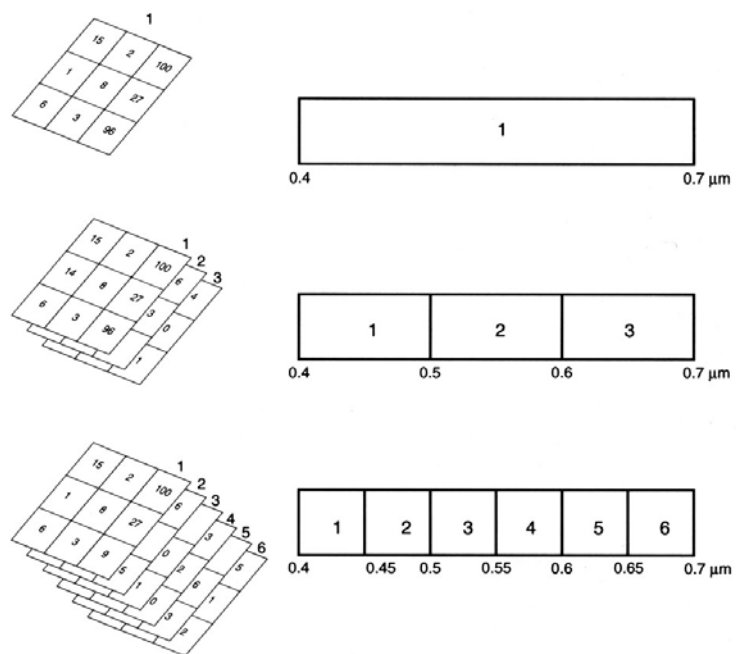


Fig. 4.1 Three sets of multispectral data with different spectral resolutions  
(Gibson, 2000)

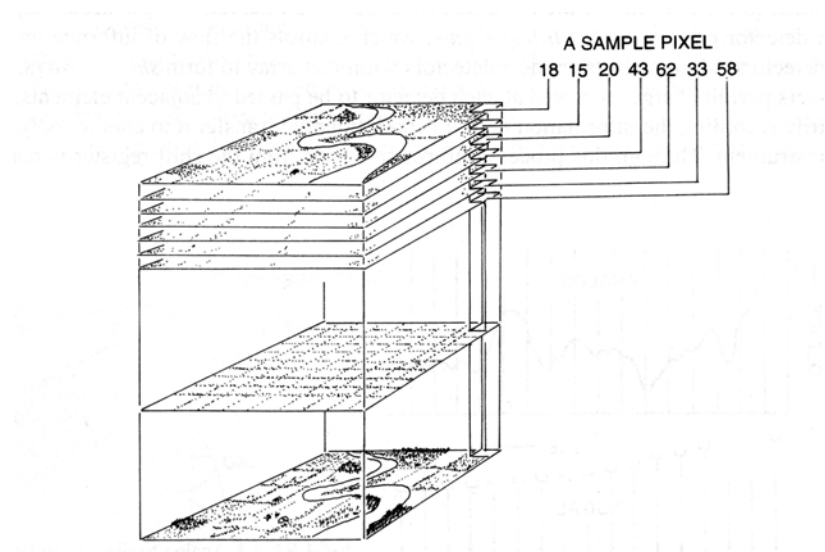


Fig 4.2 Digital numbers corresponding to a pixel (Campbell, 1996)

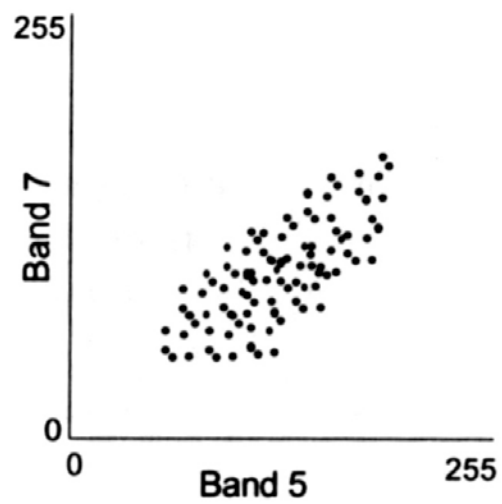


Fig. 4.3a Spectral Data Before Establishing Principal Components (Wilkie and Finn, 1996)

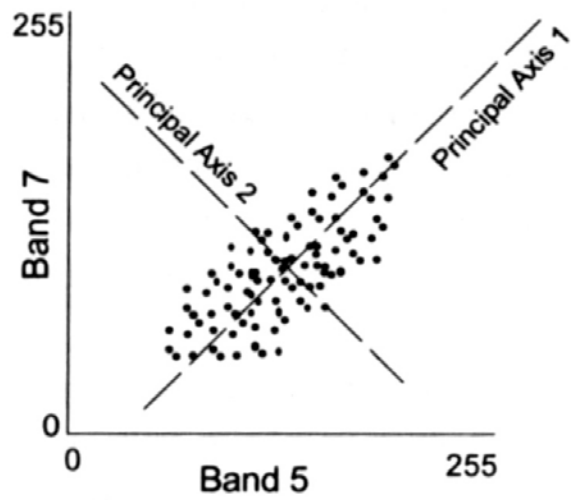


Fig. 4.3b Spectral Data After Establishing Principal Components (Wilkie and Finn, 1996)

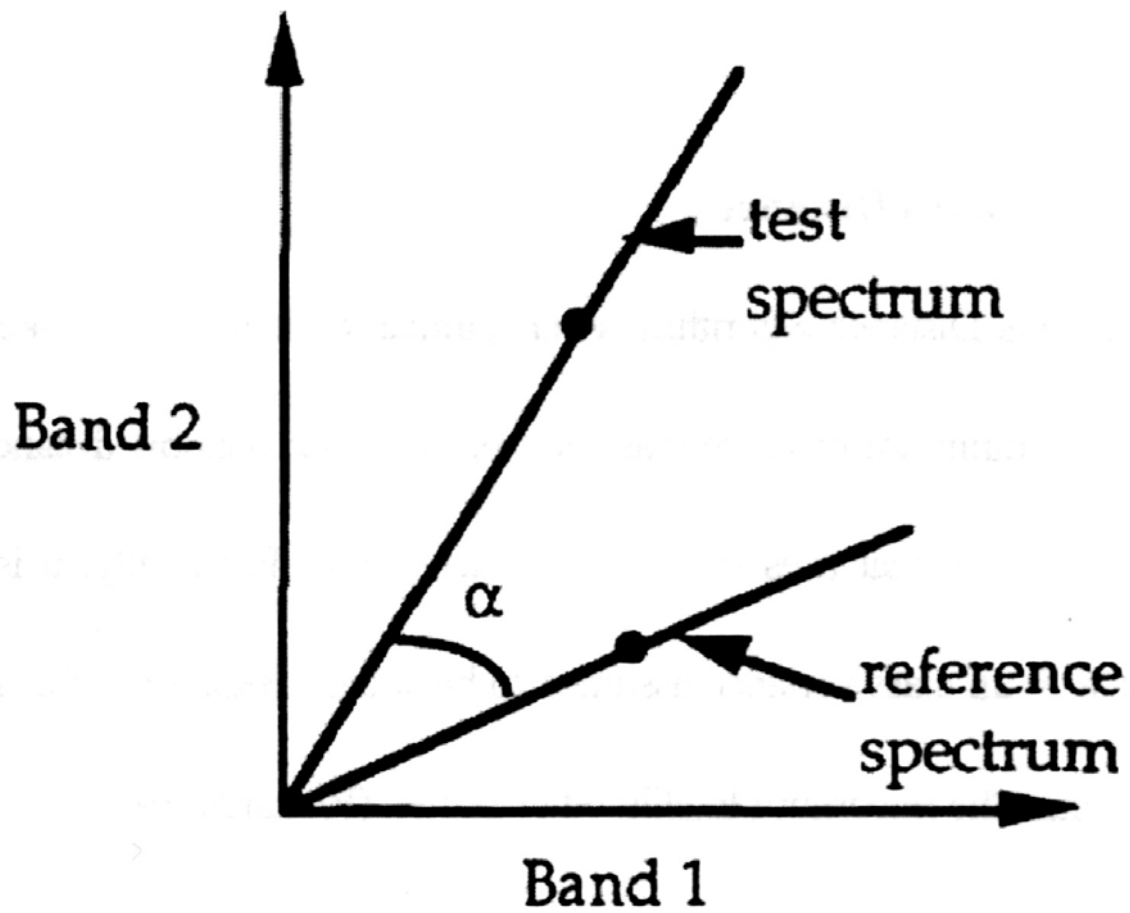


Fig. 4.4 The Spectral Angle ' $\alpha$ ' (Kruse, 1993)

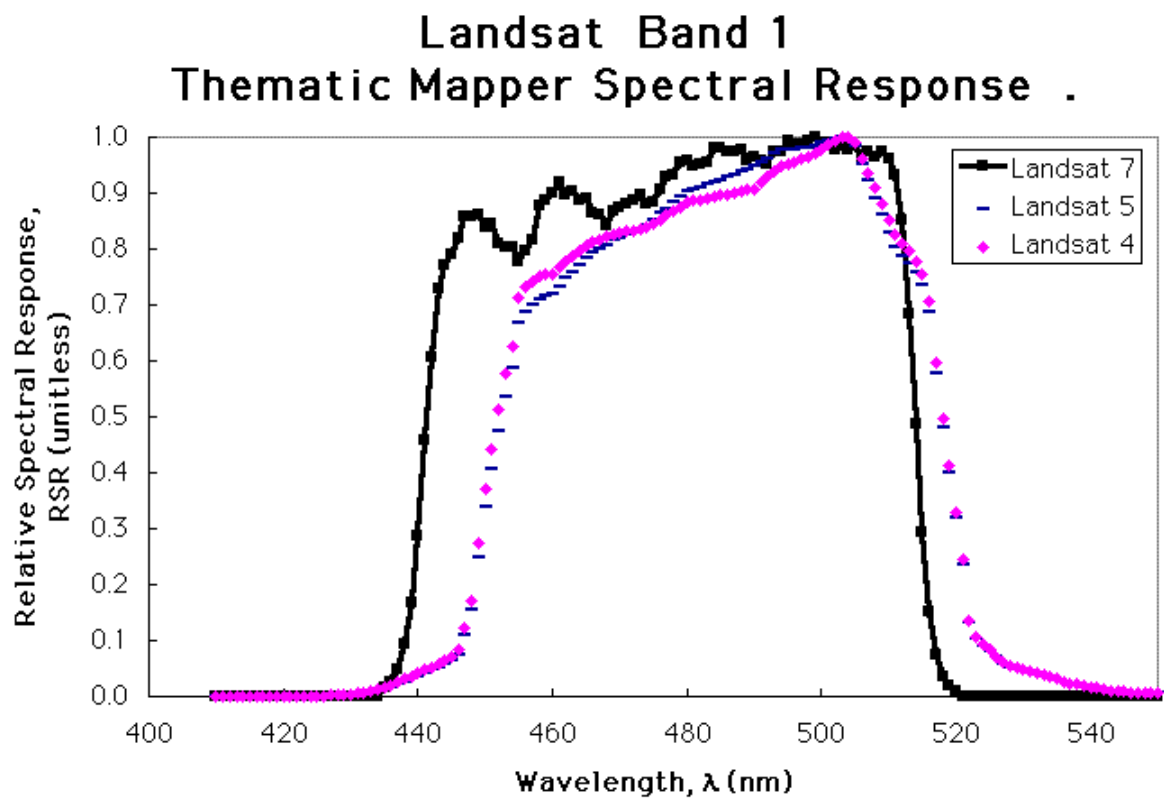


Fig. 5.1 Spectral Response of the ETM+ for band 1 (SDUH)

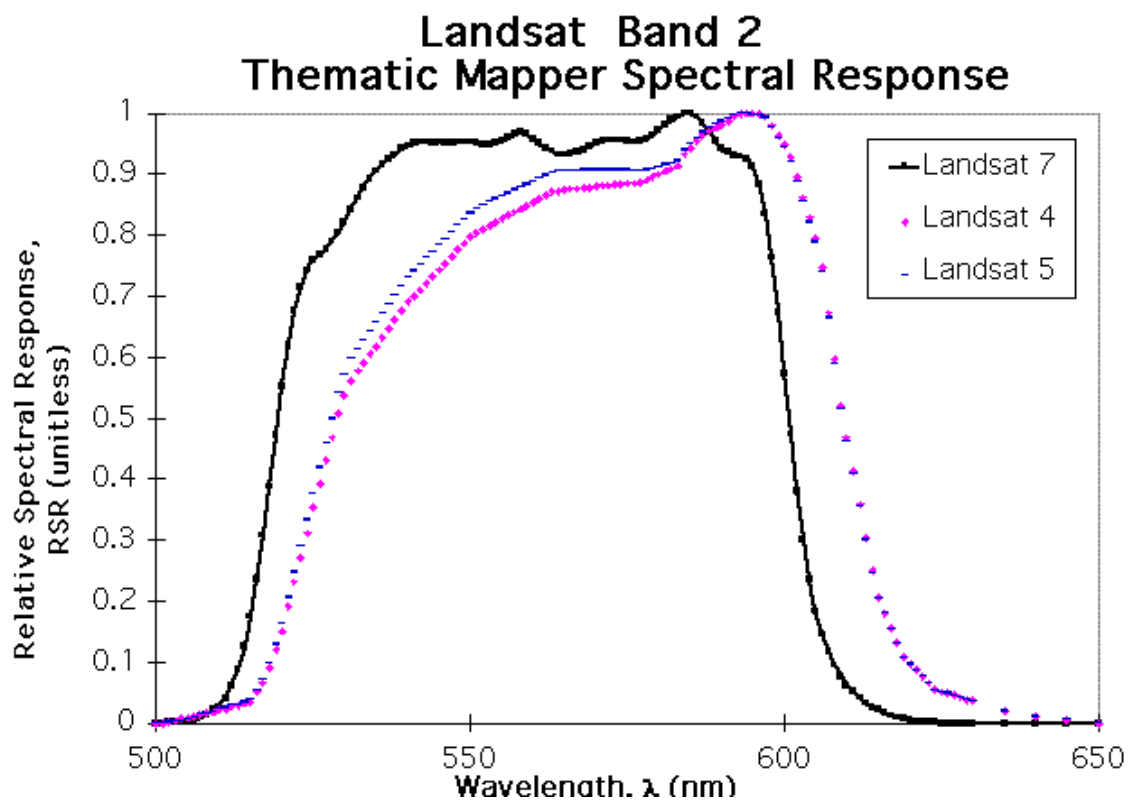


Fig. 5.2 Spectral Response of the ETM+ for band 2 (SDUH)

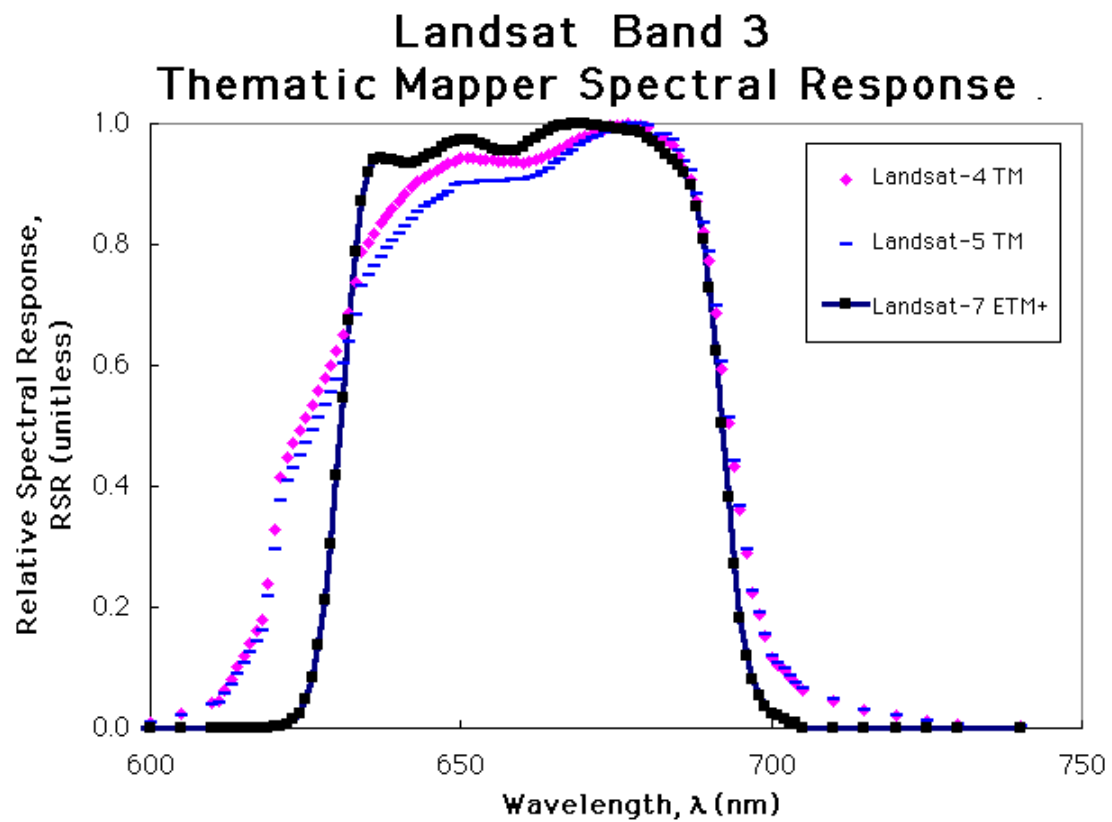


Fig. 5.3 Spectral Response of the ETM+ for band 3 (SDUH)

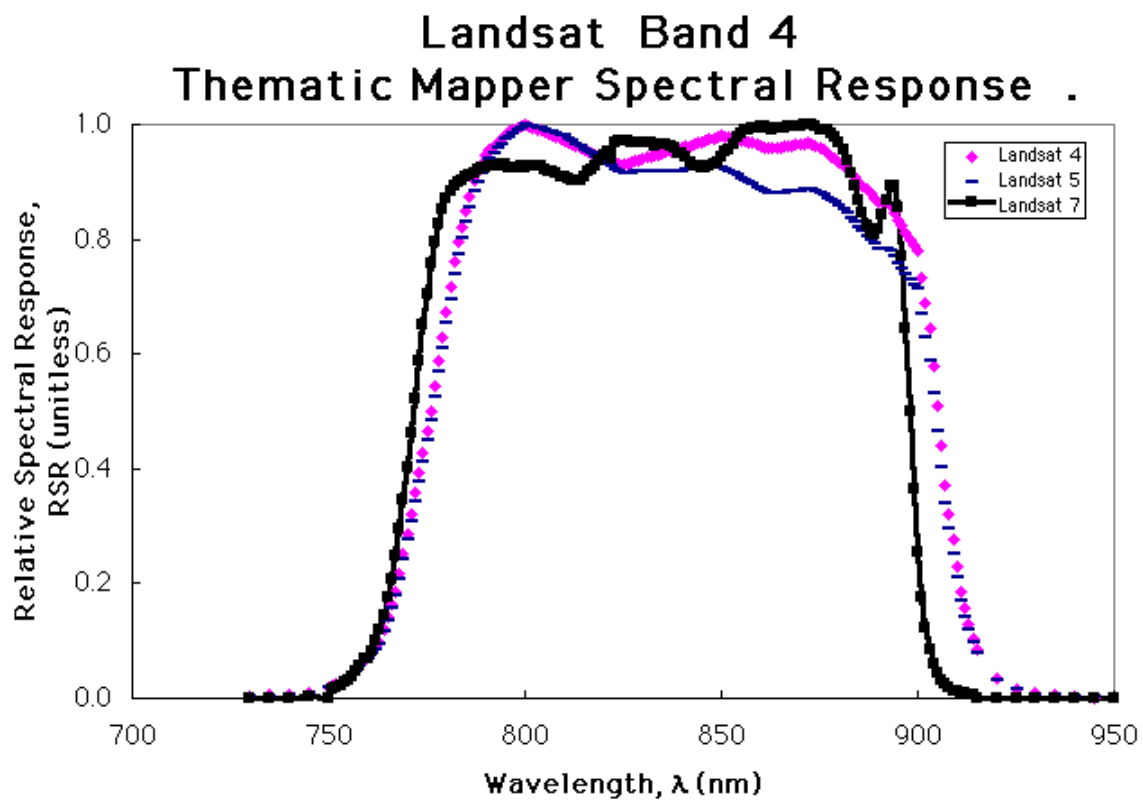


Fig. 5.4 Spectral Response of the ETM+ for band 4 (SDUH)

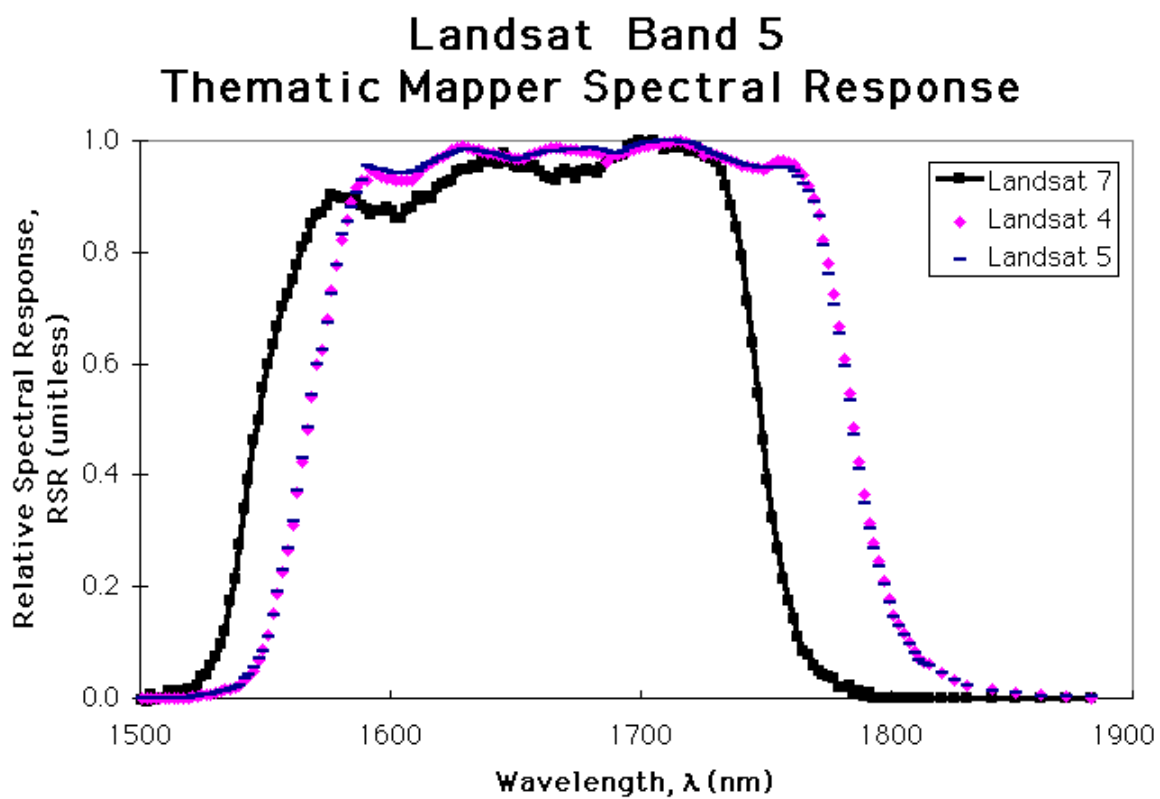


Fig. 5.5 Spectral Response of the ETM+ for band 5 (SDUH)

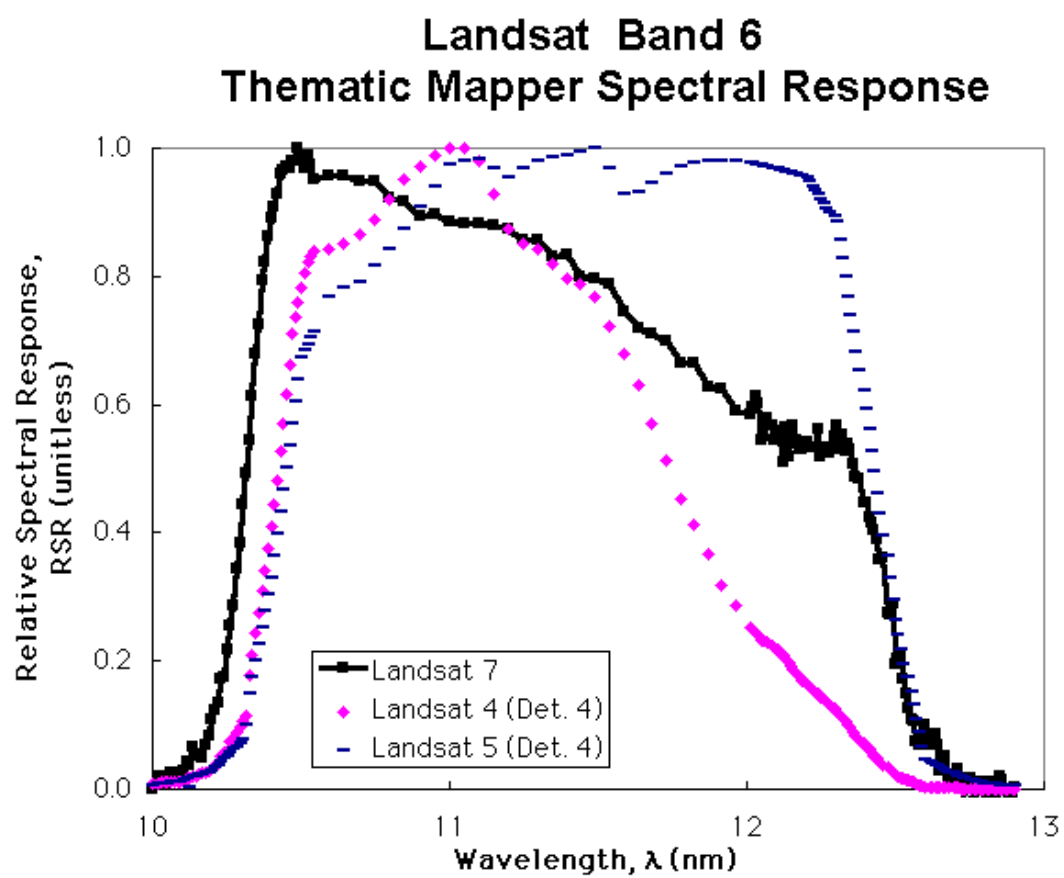


Fig. 5.6 Spectral Response of the ETM+ for band 6 (SDUH)

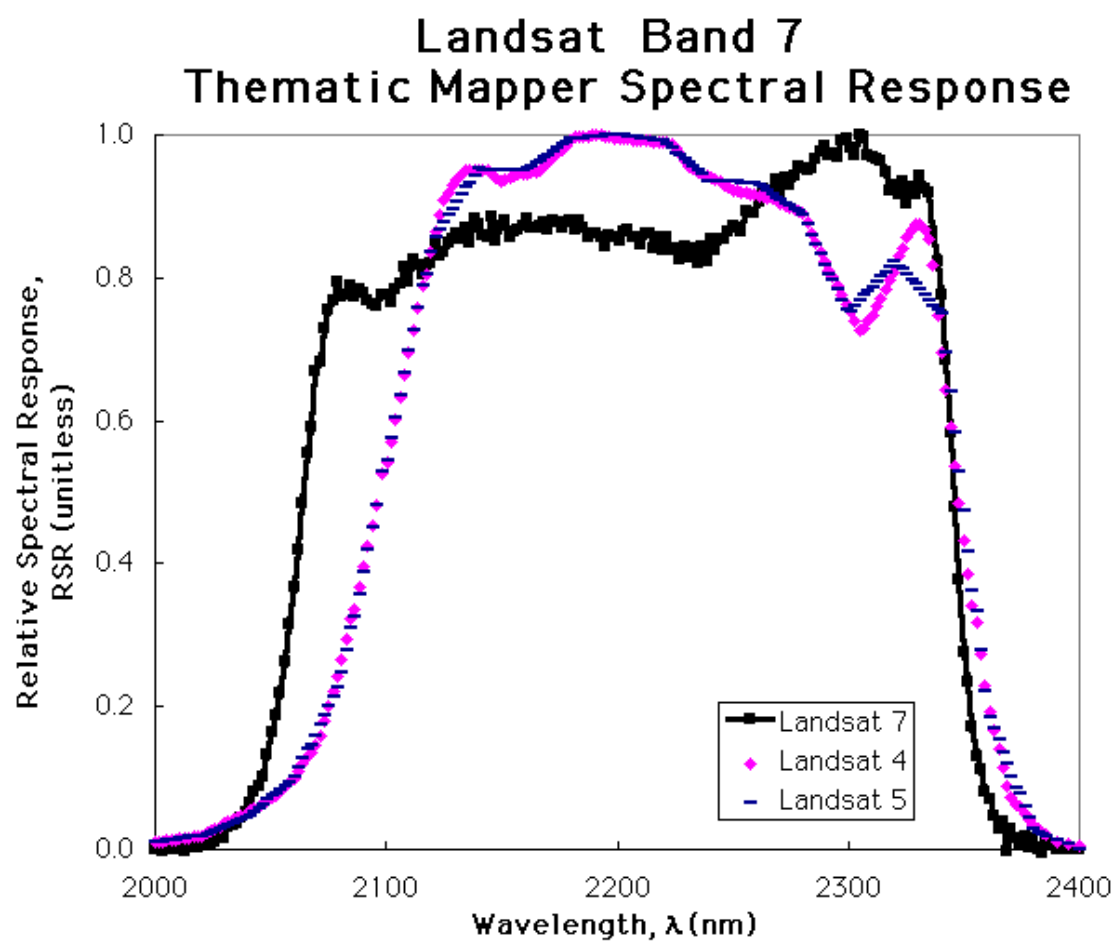


Fig. 5.7 Spectral Response of the ETM+ for band 7 (SDUH)

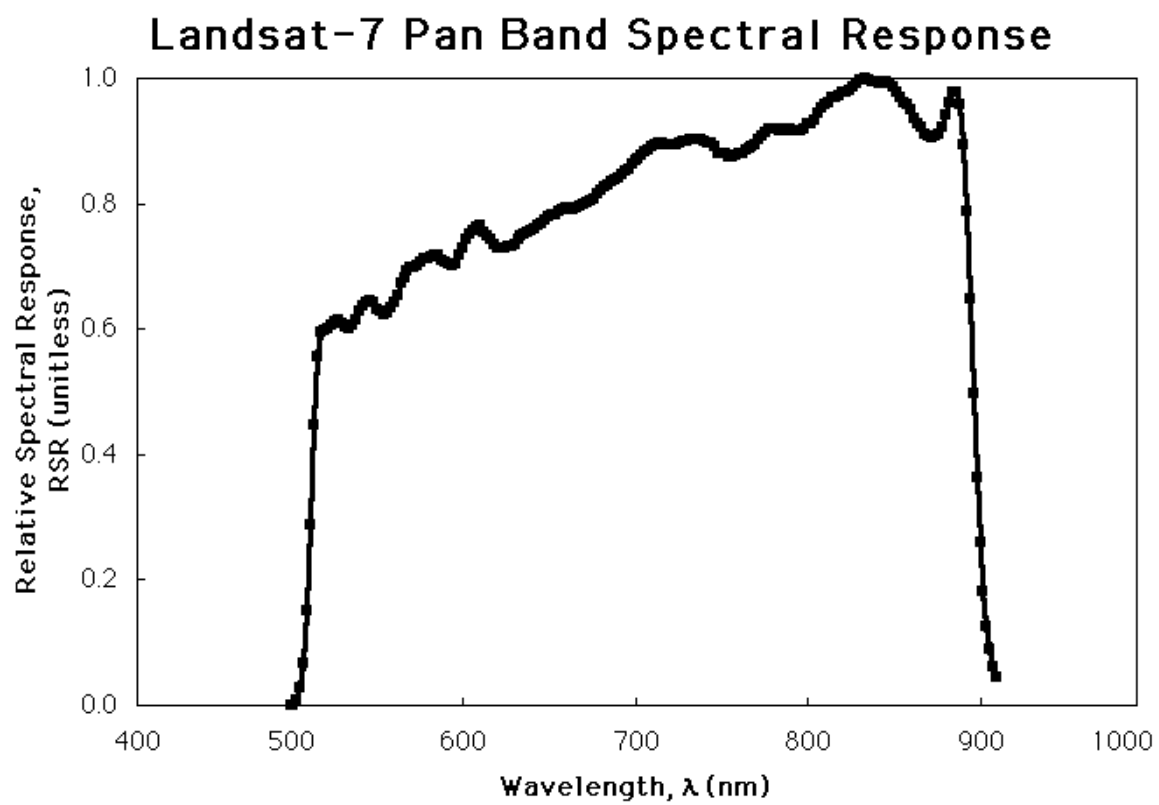


Fig. 5.8 Spectral Response of the ETM+ for band 8 (SDUH)

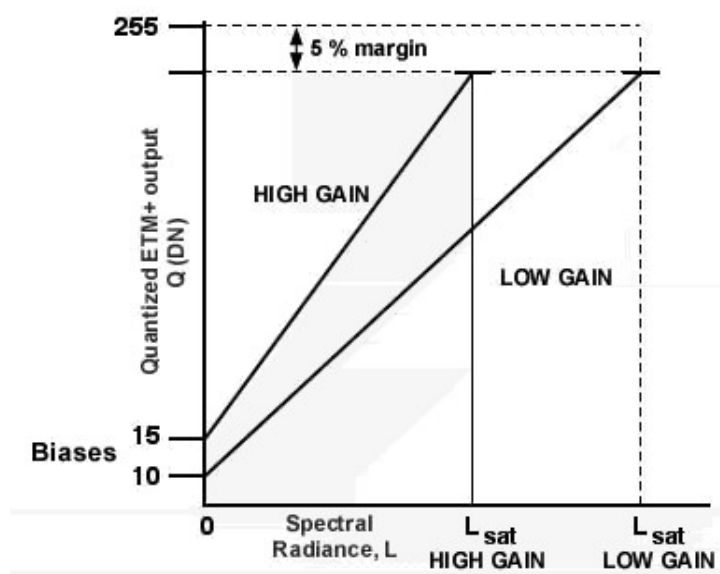


Fig. 5.9 Reflective Band Gain Dynamic Ranges (SDUH)

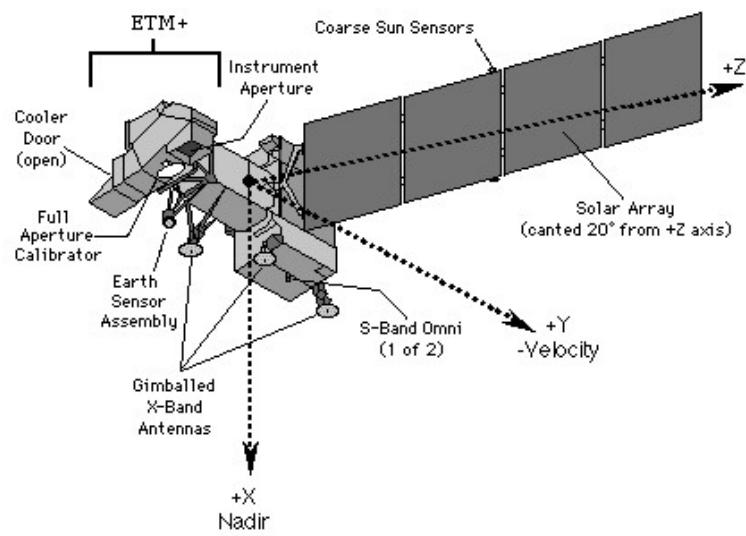


Fig. 5.10 Landsat 7 with ETM+ (SDUH)

<b>Launch Information</b>	<b>Vehicle:</b> Lockheed Martin Athena II <b>Rocket Location:</b> Vandenberg Air Force Base, California
<b>Resolution</b>	<b>• Ground resolution of each band:</b> 1-meter panchromatic (nominal at <26deg off nadir) 4-meter multispectral <b>• The ground processing software has the capability to rapidly process and mosaic imagery collected at various imaging angles so as to create seamless image products with a consistent pixel GSD.</b>
<b>Revisit frequency</b>	2.9 days at 1-meter resolution; 1.5 days at 1.5-meter resolution. These values are for targets at 40 degrees latitude.
<b>Spectral Bands</b>	<b>Panchromatic:</b> 0.45 - 0.90 microns <b>Multispectral:</b> #1: Blue 0.45 - 0.52 #2: Green 0.52 - 0.60 #3: Red 0.63 - 0.69 #4: Near IR 0.76 - 0.90 (same as Landsat 4&5 TM Bands #1-4)
<b>Swath Widths &amp; Scene Sizes</b>	<b>Nominal swath width:</b> • 11 km at nadir <b>Areas of interest:</b> • a single image at 11 km x 11 km • strips of 11 km x 100 km up to 11 km x 1000 km • image mosaics of up to 12,000 sq. km • up to two 10,000 square kilometer areas in a single pass within a region
<b>Metric Accuracy</b>	• 12-meter horizontal and 10-meter vertical accuracy with no control • 2-meter horizontal and 3-meter vertical accuracy with GCP control • These are specified as 90% CE (circular error) for the horizontal and 90% LE (linear error) for the vertical
<b>Orbital Information</b>	<b>Altitude:</b> 681 kilometers / 423 miles <b>Inclination angle:</b> 98.1 deg <b>Speed:</b> 4 miles per second / 7 kilometers per second <b>Descending nodal crossing time:</b> 10-11 a.m. <b>Revisit frequency:</b> 3 days at 1-meter resolution; 1.5 days at 1.5 meter resolution <b>Orbit time:</b> 98 minutes <b>Orbit type:</b> sun-synchronous <b>Viewing angle:</b> Agile spacecraft - in-track and cross-track pointing <b>Weight:</b> 1600 pounds

Fig. 5.11 Additional Ikonos specifications (Space Imaging SE-REF-016 Rev. A)

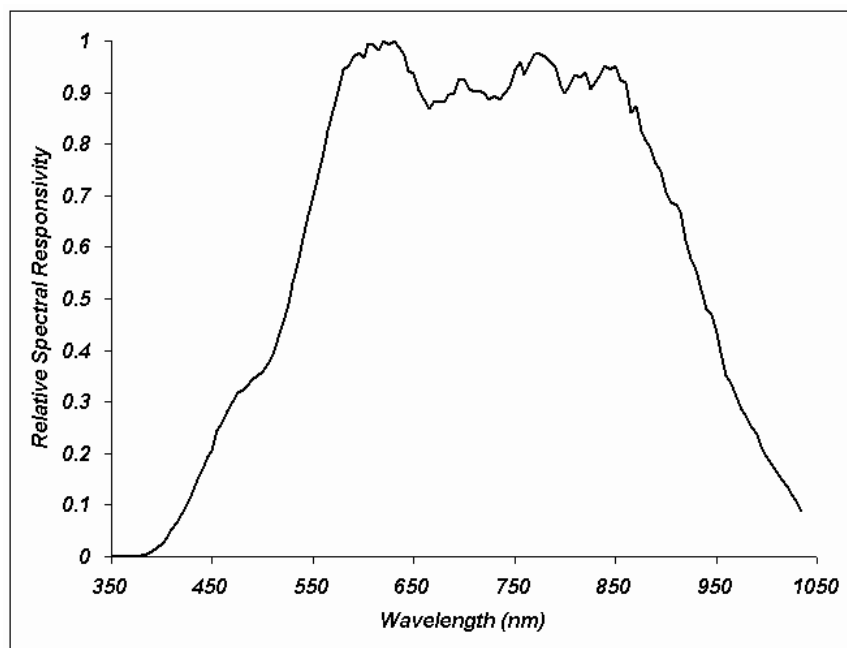


Fig. 5.12 Panchromatic Relative Spectral Response (Space Imaging)

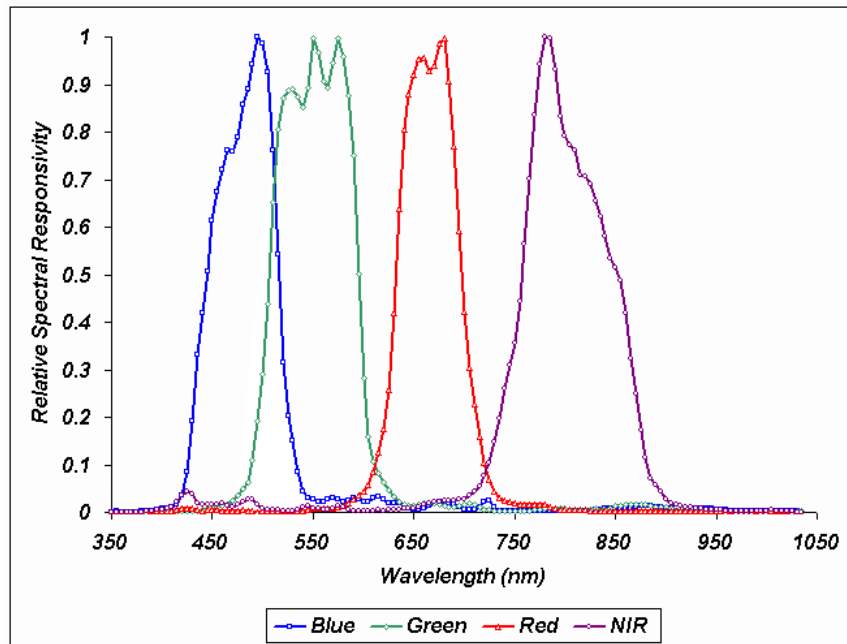


Fig. 5.13 Multispectral Relative Spectral Response (Space Imaging)

Band	Lower 50% (nm)	Upper 50% (nm)	Bandwidth (nm)	Center (nm)
Pan	525.8	928.5	403	727.1
MS-1 (Blue)	444.7	516.0	71.3	480.3
MS-2 (Green)	506.4	595.0	88.6	550.7
MS-3 (Red)	631.9	697.7	65.8	664.8
MS-4 (VNIR)	757.3	852.7	95.4	805.0

Note: 1. Spectral Bandwidths are Full-Width at Half-Max

Table 5.1 IKONOS Spectral Band Characteristics (Space Imaging)

<i><b>IKONOS Radiometric Calibration Coefficients for 11 bit products [mW/(cm<sup>2</sup>*sr*DN)]</b></i>				
<b>Production Date</b>	<b>Blue</b>	<b>Green</b>	<b>Red</b>	<b>NIR</b>
<b>pre 2/22/01</b>	633	649	840	746
<b>post 2/22/01</b>	728	727	949	843

<i><b>IKONOS Radiometric Calibration Coefficients for 8 bit products [mW/(cm<sup>2</sup>*sr*DN)]</b></i>				
<b>Production Date</b>	<b>Blue</b>	<b>Green</b>	<b>Red</b>	<b>NIR</b>
<b>pre 2/22/01</b>	79	81	105	93
<b>post 2/22/01</b>	91	91	119	105

Table 5.2 Calibration Coefficients for 8 and 11 bit IKONOS data (Space Imaging)

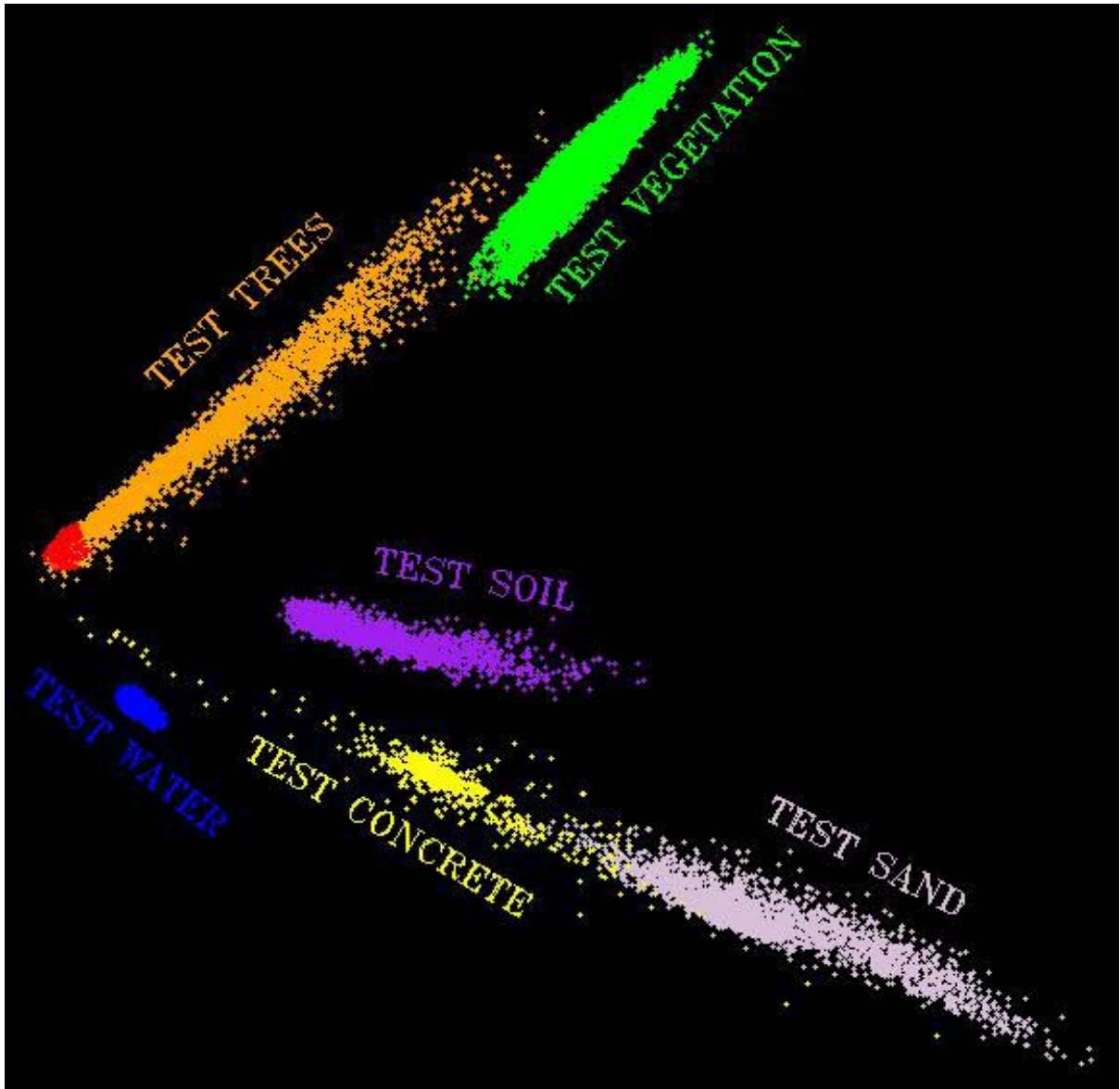


Fig. 6.1 NDV Plot of Reference Classes

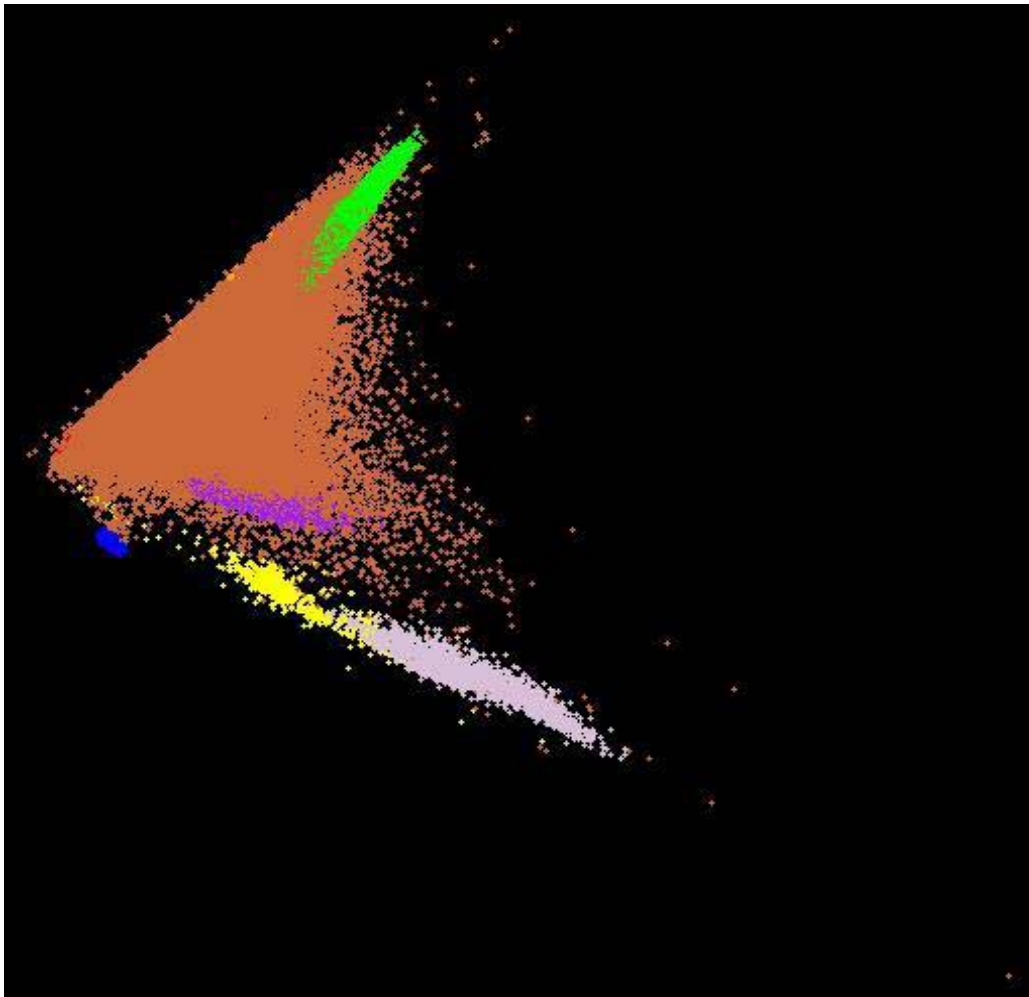


Fig. 6.2 NDV Plot of Reference Class with Eucalyptus ROI (Sienna)

## APPENDIX B. FIGURES AND TABLES OF RESULTS



Figure 6.3 SAM Chaparral Rule Image



Figure 6.4 SAM Conifer Rule Image



Figure 6.5 SAM Cultivated Fields Rule Image



Figure 6.6 SAM Development Rule Image



Figure 6.7 SAM Dry Ponds Rule Image

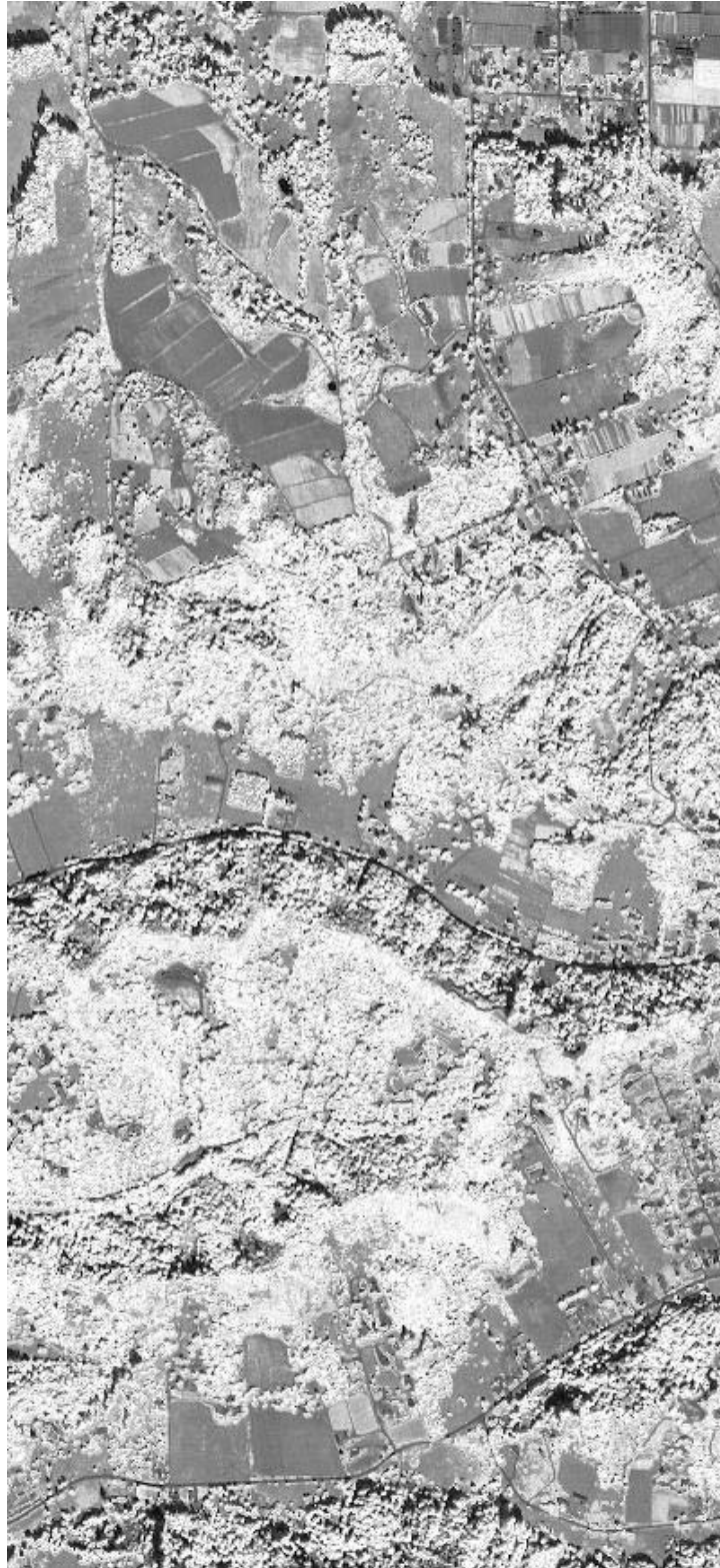


Figure 6.8 SAM Eucalyptus Rule Image



Figure 6.9 SAM Fallow Rule Image



Figure 6.10 SAM Fresh Water Marsh Rule Image



Figure 6.11 SAM Green House Rule Image

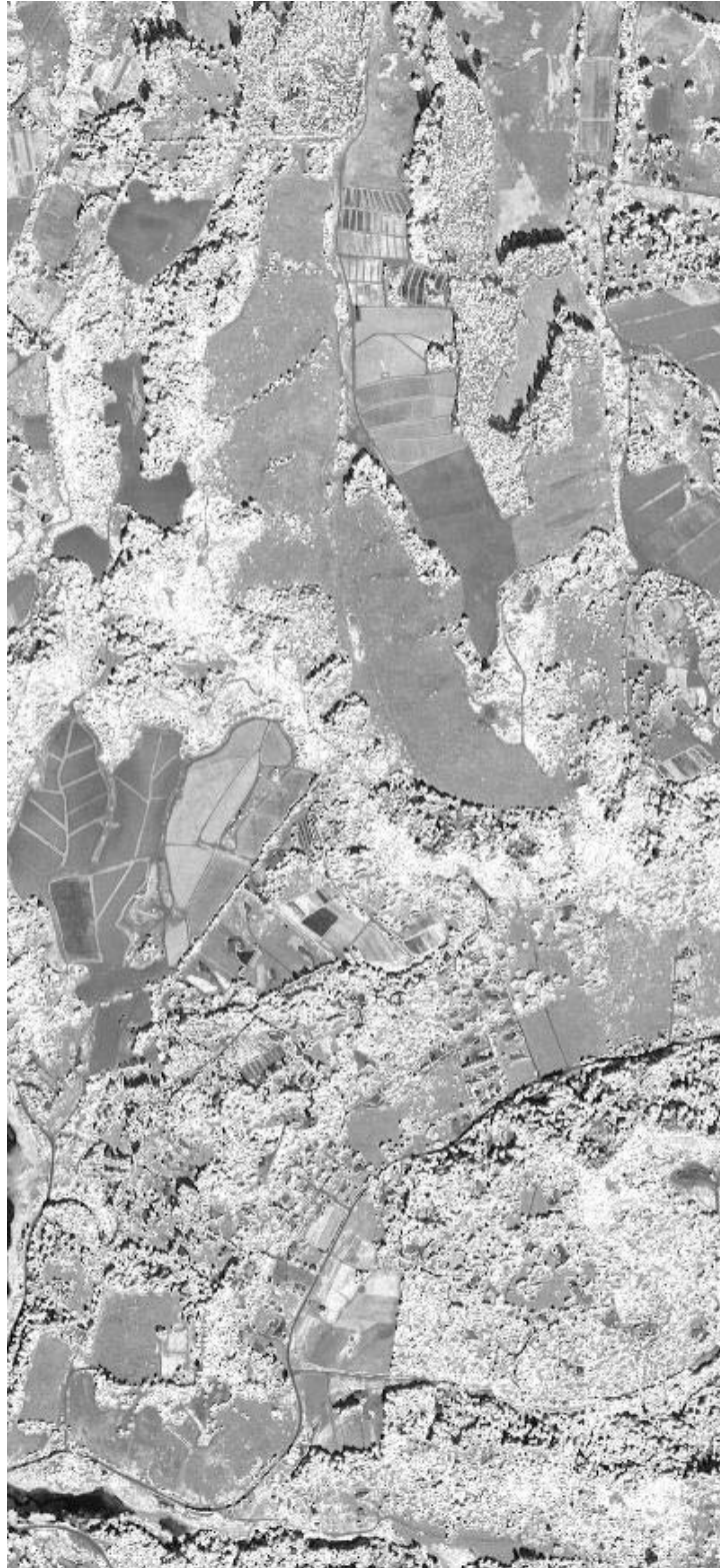


Figure 6.12 SAM Maritime Chaparral Rule Image



Figure 6.13 SAM Ponds Rule Image



Figure 6.14 SAM Riparian Rule Image



Figure 6.15 SAM Sage Scrub Rule Image

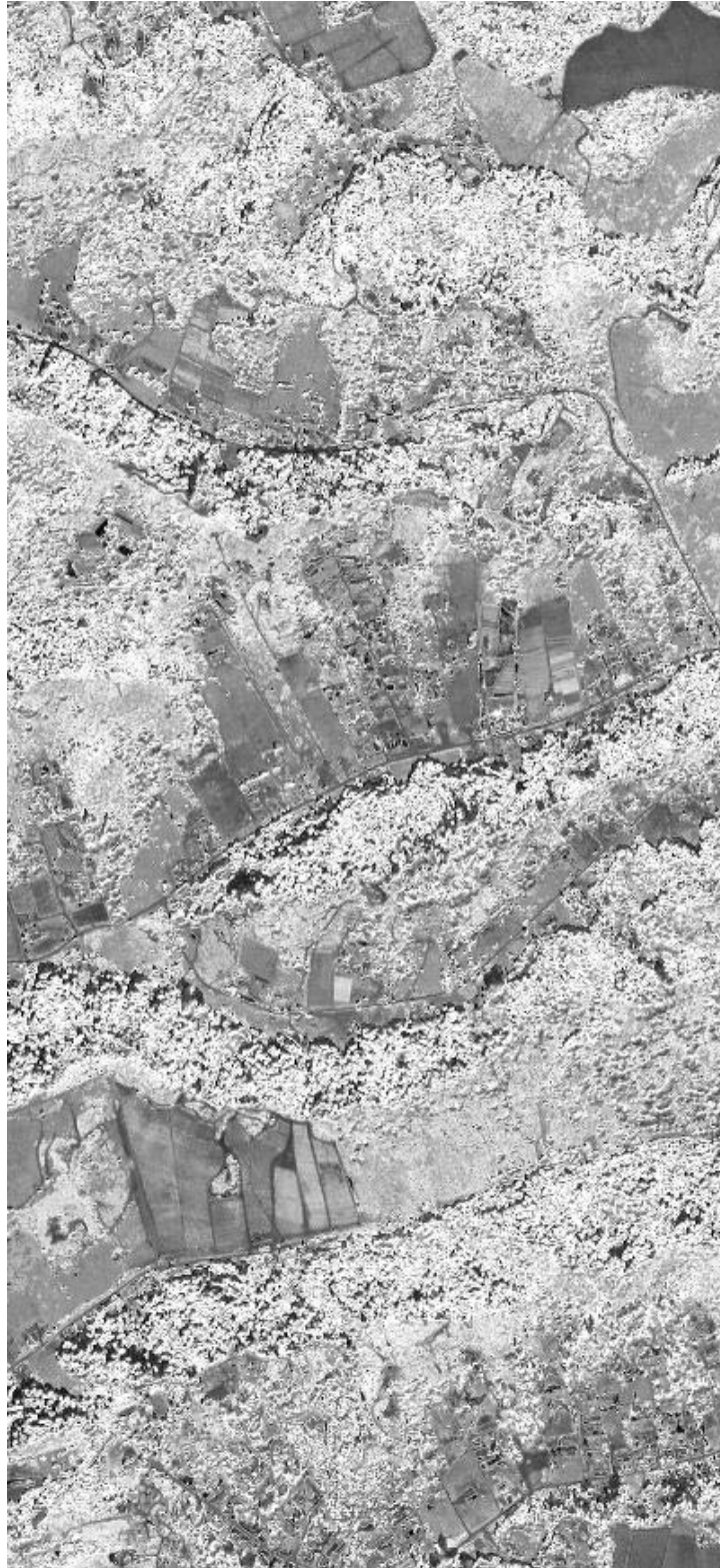


Figure 6.16 SAM Shadowed Oak Rule Image



Figure 6.17 SAM Slough Water Rule Image



Figure 6.18 SAM Sunlit Oak Rule Image

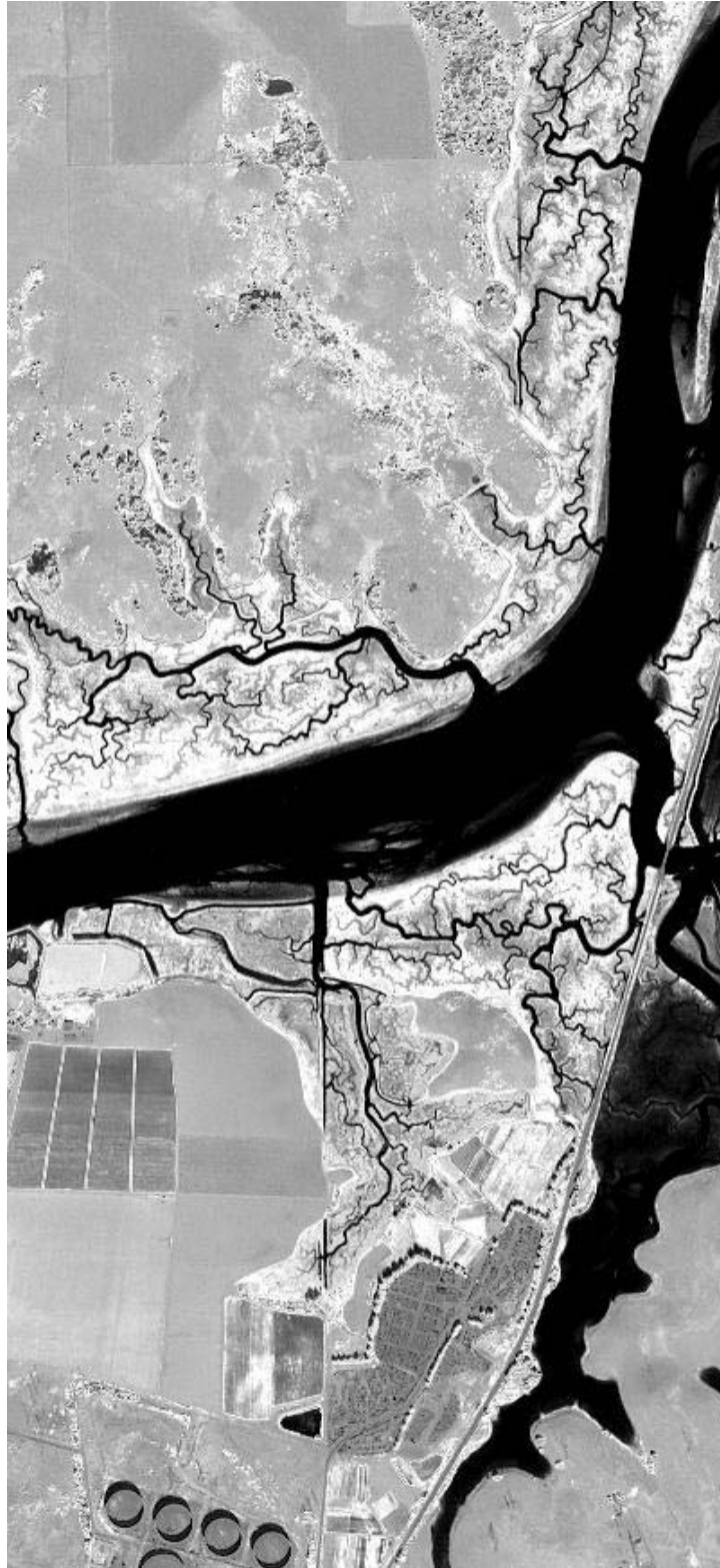


Figure 6.19 SAM Tidal Wetland Rule Image



Figure 6.20 SAM Turf Rule Image



Figure 6.21 SAM Dune Scrub Rule Image

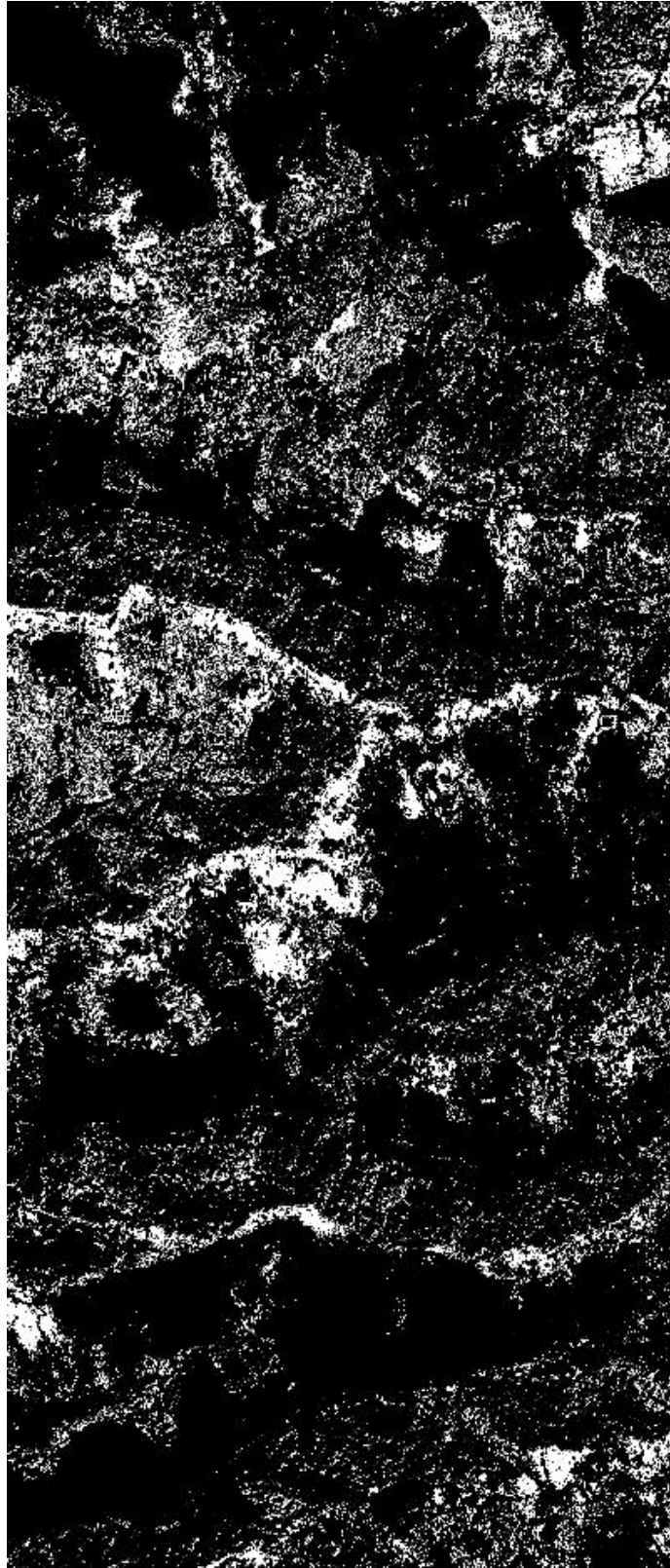


Figure 6.22 MAX.L. Chaparral Rule Image

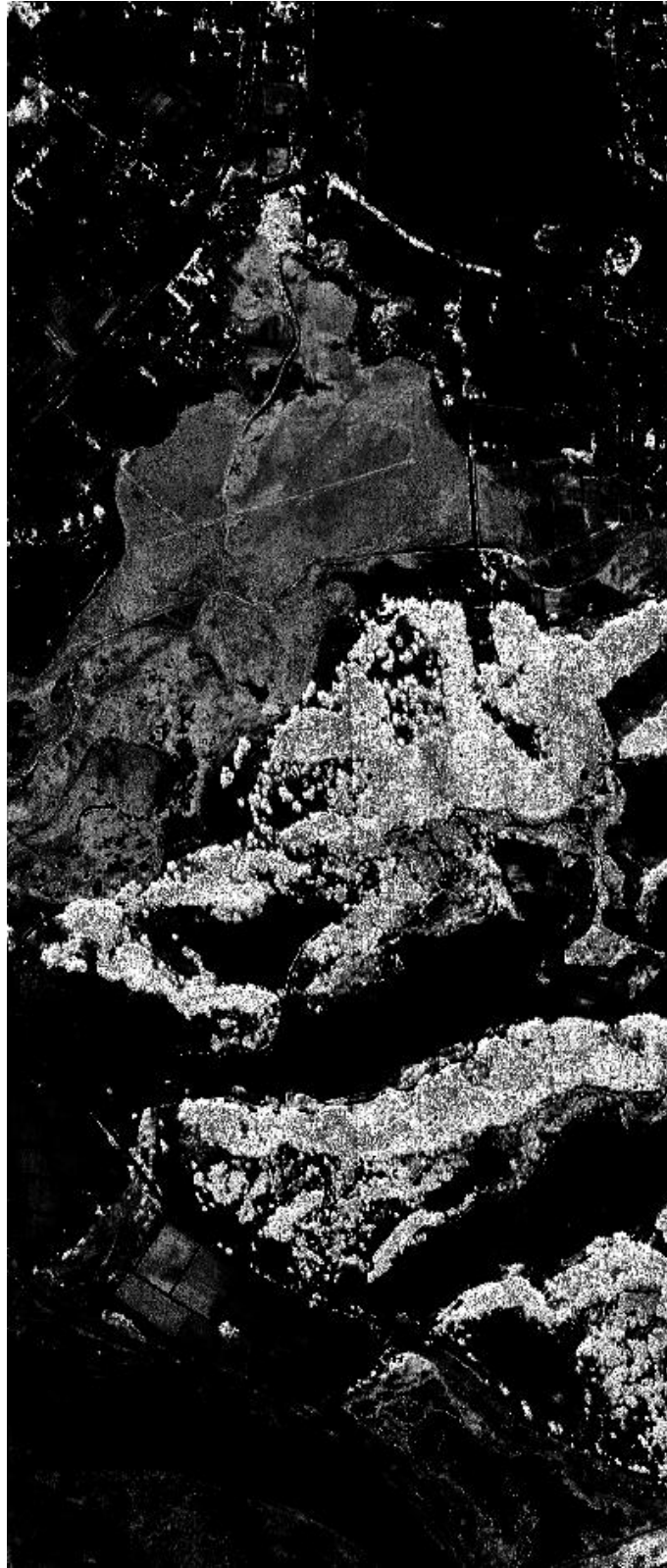


Figure 6.23 MAX.L. Conifer Rule Image



Figure 6.24 MAX.L. Cultivated Fields Rule Image



Figure 6.25 MAX.L. Development Rule Image



Figure 6.26 MAX.L. Dry Ponds Rule Image



Figure 6.27 MAX.L. Eucalyptus Rule Image



Figure 6.28 MAX.L. Fallow Rule Image



Figure 6.29 MAX.L. Fresh Water Marsh Rule Image



Figure 6.30 MAX.L. Green House Rule Image

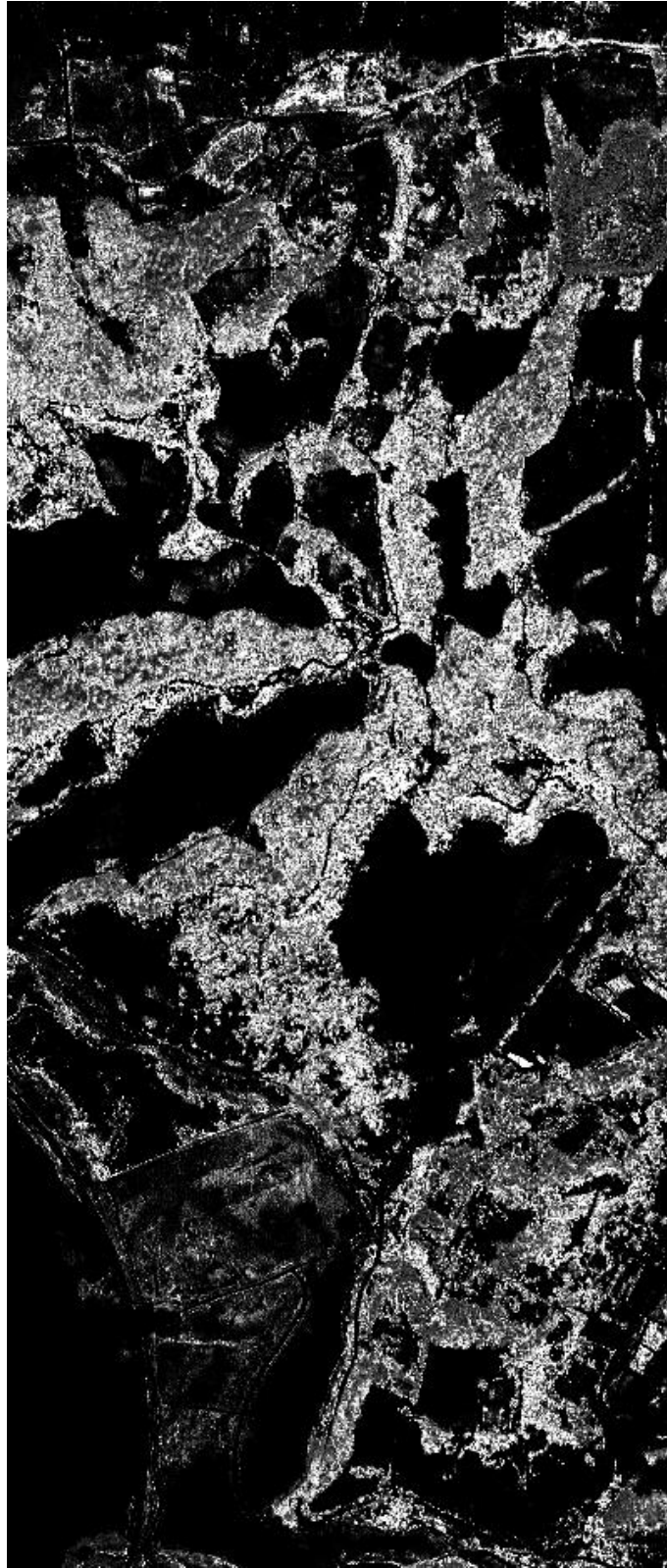


Figure 6.31 MAX.L. Maritime Chaparral Rule Image



Figure 6.32 MAX.L. Ponds Rule Image

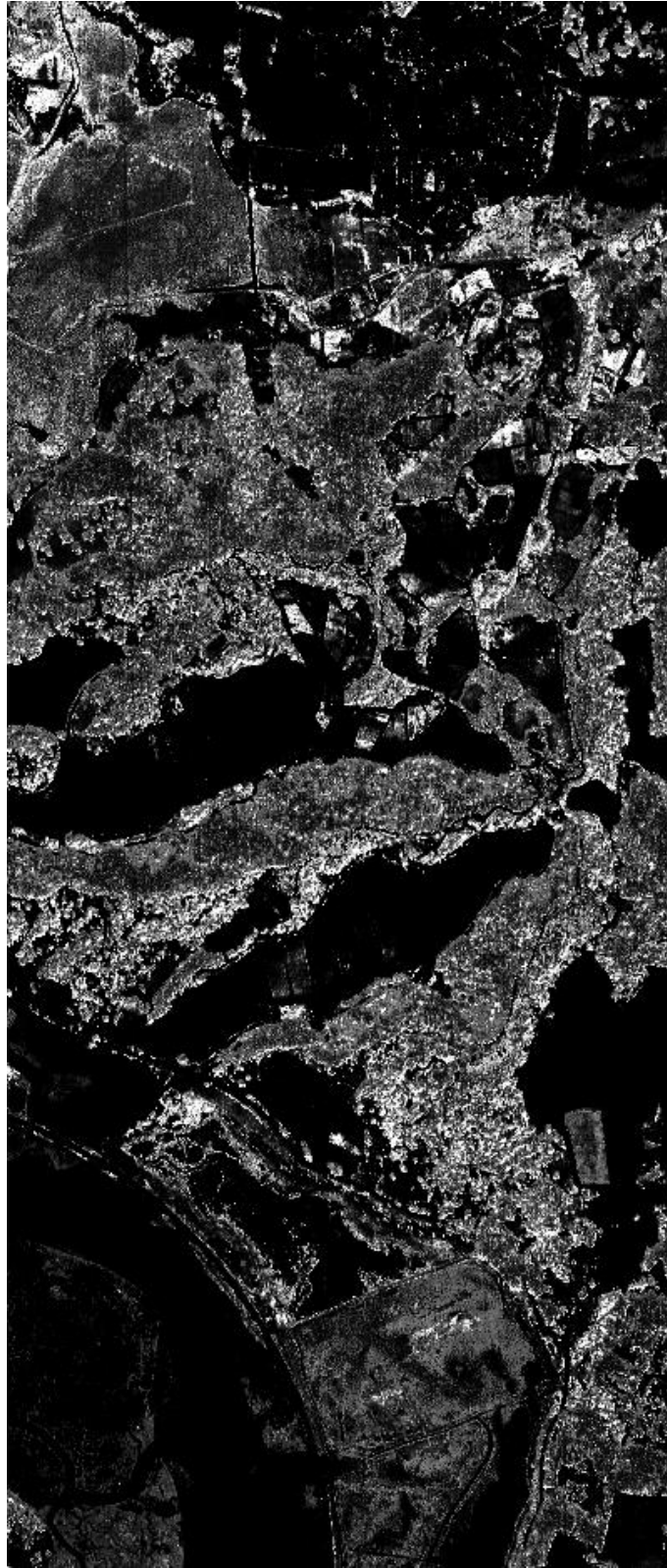


Figure 6.33 MAX.L. Riparian Rule Image

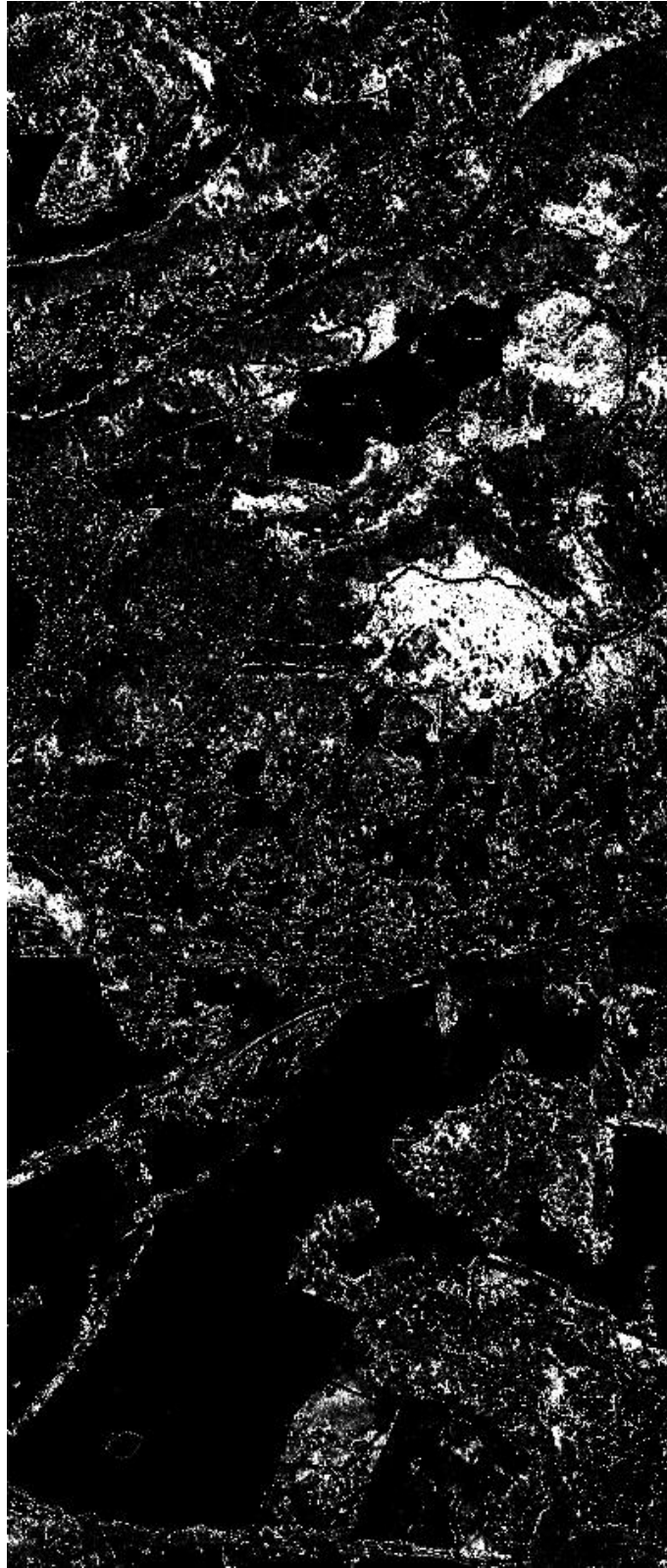


Figure 6.34 MAX.L. Sage Scrub Rule Image



Figure 6.35 MAX.L. Shadowed Oak Rule Image



Figure 6.36 MAX.L. Slough Water Rule Image

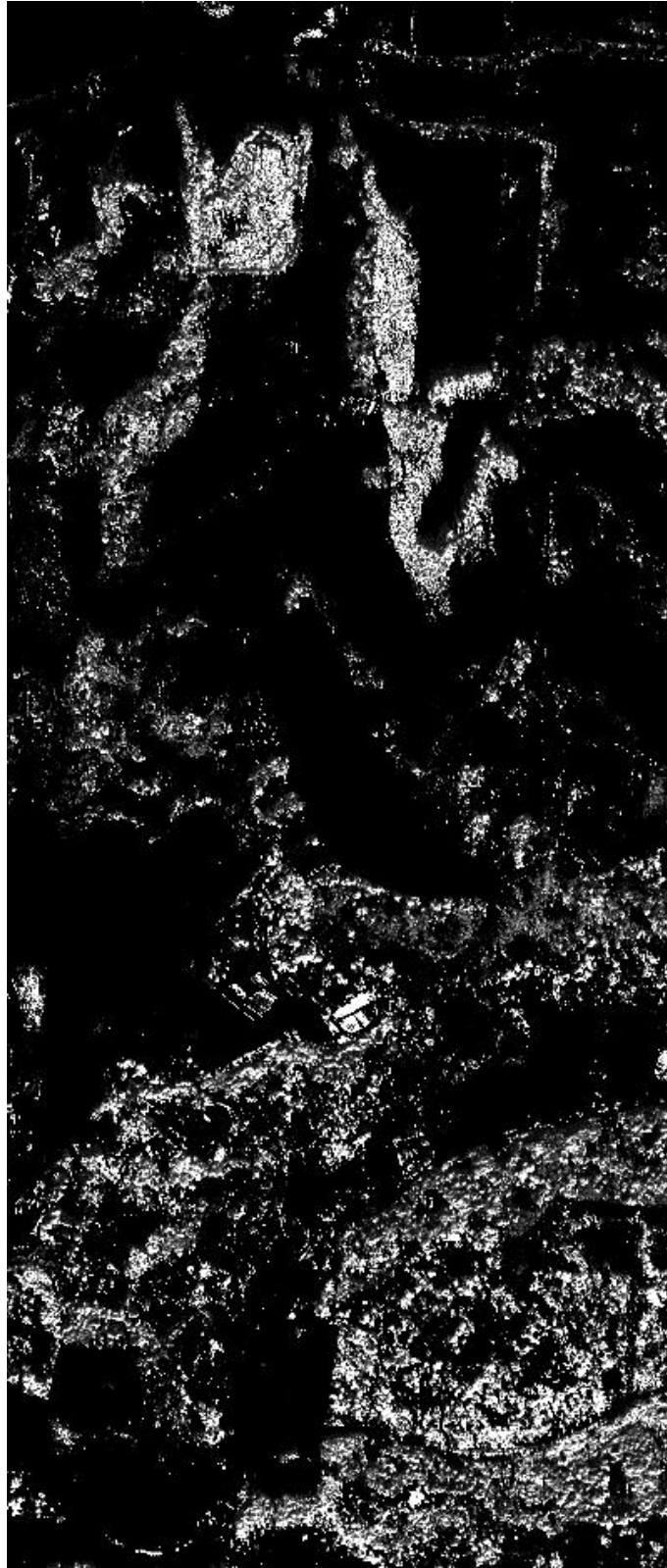


Figure 6.37 MAX.L. Sunlit Oak Rule Image

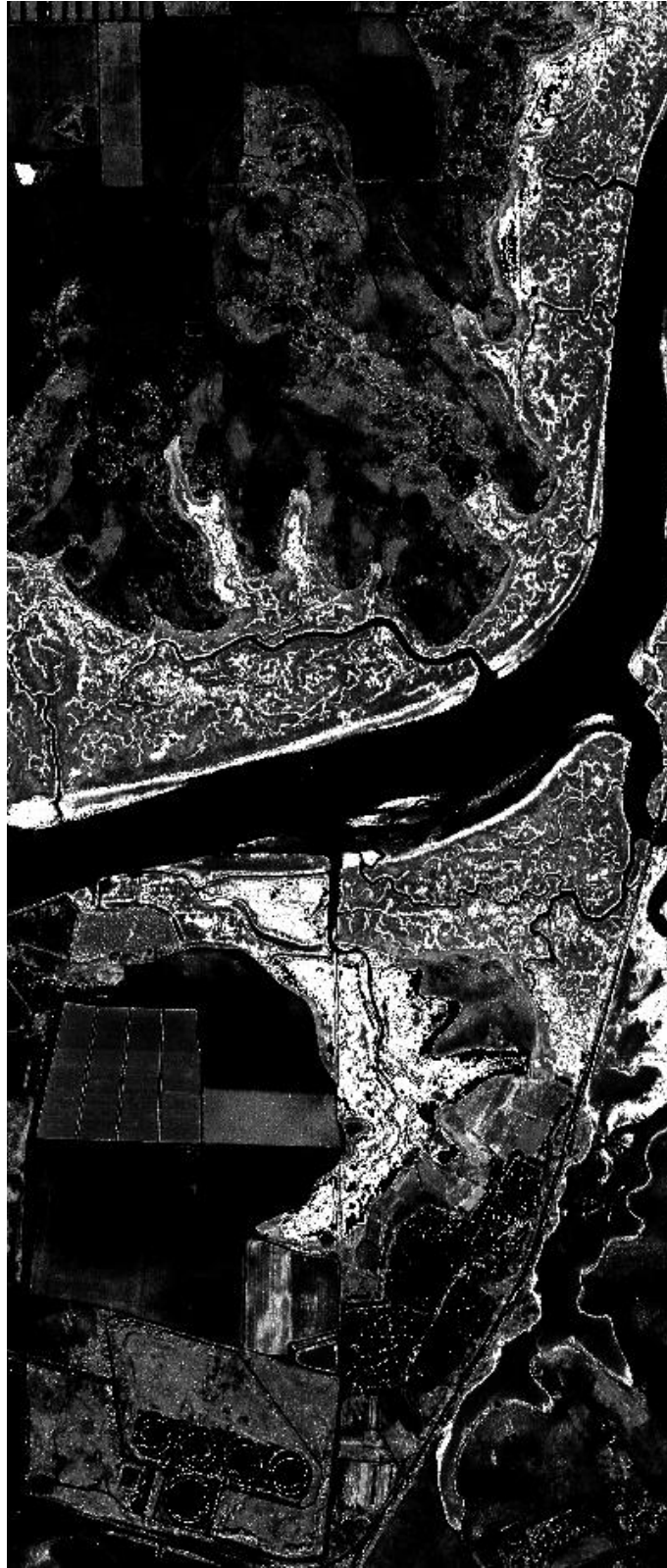


Figure 6.38 MAX.L. Tidal Wetlands Rule Image



Figure 6.39 MAX.L. Turf Rule Image



Figure 6.40 MAX.L. Dune Scrub Rule Image

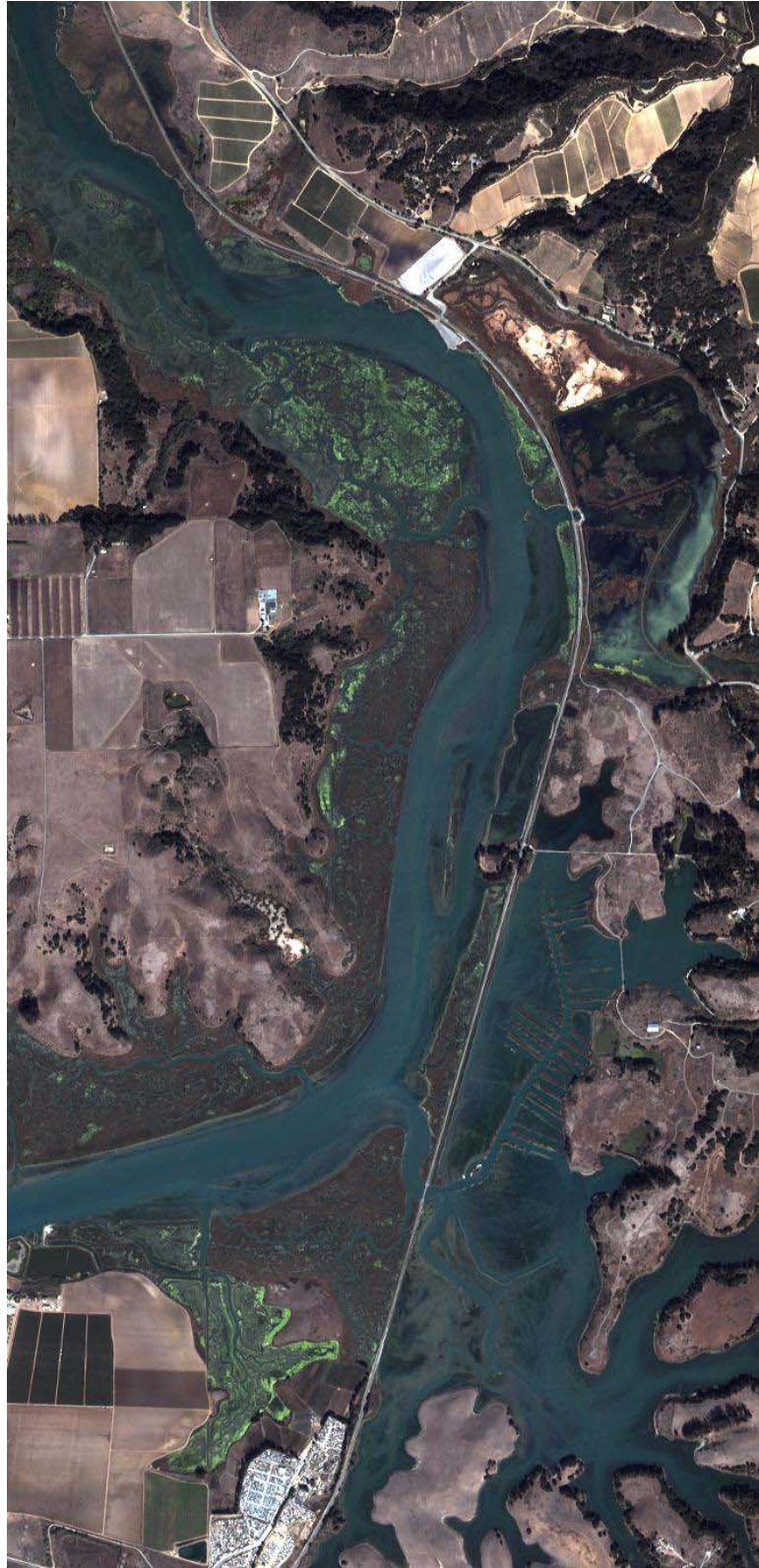


Figure 6.41 True Color Image of the Elkhorn Slough



Figure 6.42 False Color Image of the Elkhorn Slough

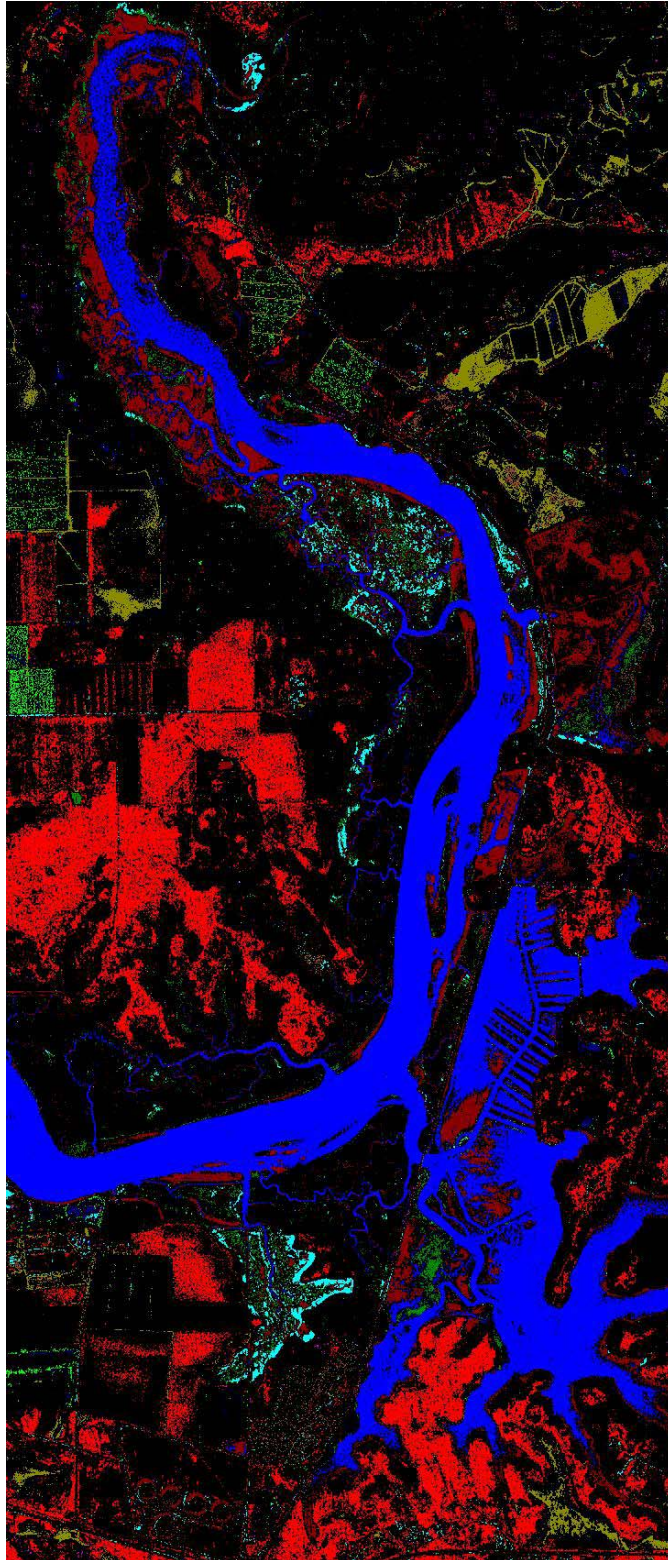


Figure 6.43 MAX.L. (85% Threshold) Classified Image

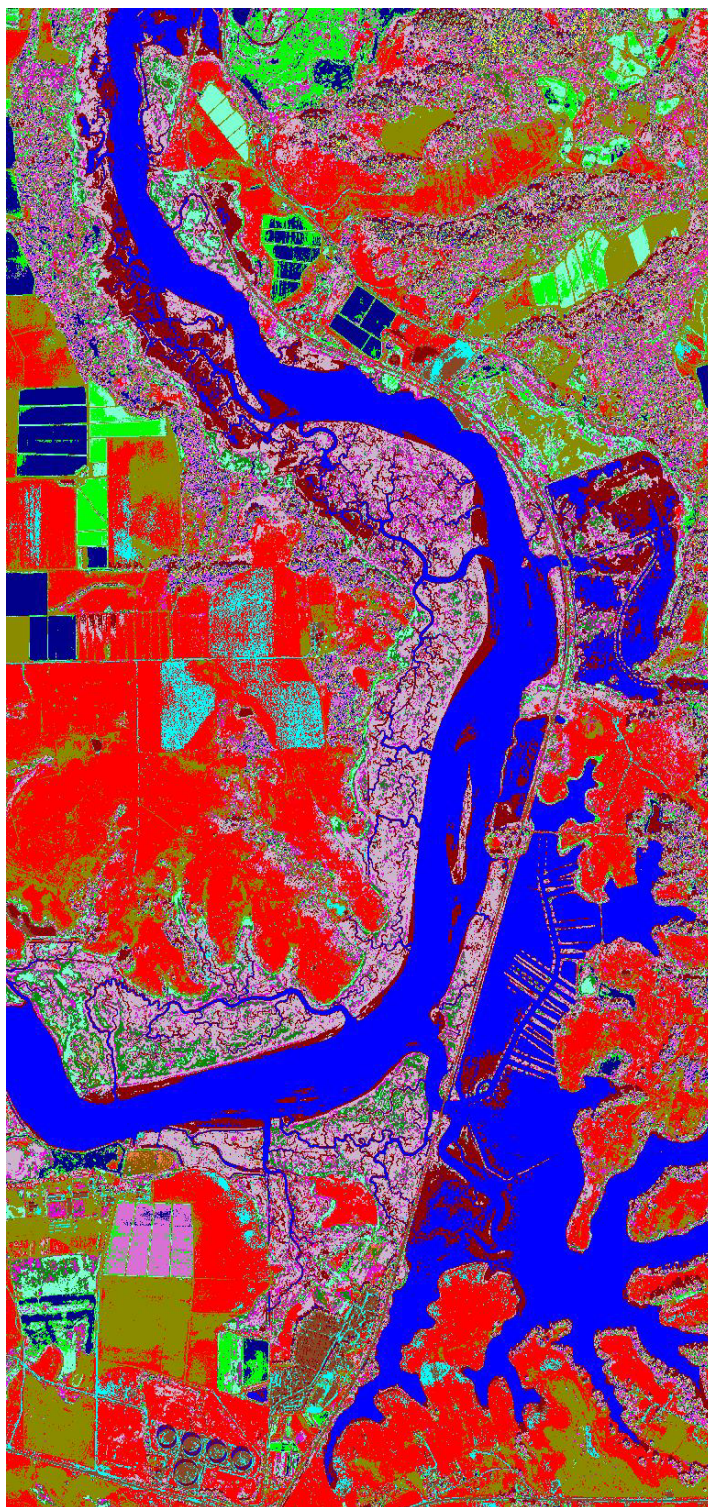


Figure 6.44 SAM (.250 Radian Threshold) Classified Image

Class	Ground Truth (Percent)				
	CONIFER	DEVELOPMENT	EUCALYPTUS	FALLOW	FWM
Unclassified	0.00	0.01	0.00	0.00	0.00
CONIFERS	5.31	0.46	6.75	0.10	0.41
DEVELOPMENT	0.35	36.77	0.04	1.80	0.57
EUCALYPTUS	8.10	0.32	11.21	0.09	0.38
FALLOW	2.47	8.12	0.41	42.99	8.48
FWM	3.02	3.15	1.27	3.02	13.61
GREENHOUSE	0.48	15.70	0.09	11.96	0.71
M. CHAPARRAL	2.14	1.01	1.46	0.26	2.27
RIPARIAN	1.75	0.84	1.15	0.29	2.68
SAGE SCRUB	12.13	4.15	9.56	4.06	8.52
SLOUGH WATER	1.89	1.96	0.56	0.07	0.24
TURF	3.27	1.26	5.68	2.36	7.62
CULT. FIELDS	2.16	2.16	2.79	1.83	13.46
DUNE SCRUB	1.79	1.85	0.51	4.75	7.79
CHAPARRAL	5.84	1.77	6.40	0.70	6.46
SUNLIT OAK	15.65	0.92	22.42	0.41	3.92
SHADOWED OAK	10.05	0.99	15.52	0.21	1.04
DRY PONDS	5.47	6.63	0.96	20.62	8.97
TIDAL WETLAND	2.56	2.15	0.98	2.42	10.00
PONDS	15.59	9.79	12.25	2.02	2.86
Total	100.00	100.00	100.00	100.00	100.00

Table 6.1a SAM Confusion Matrix

Class	Ground Truth (Percent)				
	GREENHOUSE	M. CHAPARRAL	RIPARIAN	SAGE SCRUB	SLOUGH WATER
Unclassified	0.00	0.00	0.10	0.00	0.00
CONIFERS	0.02	5.21	2.29	1.70	0.00
DEVELOPMENT	28.24	0.26	0.90	0.07	2.39
EUCALYPTUS	0.03	4.37	1.97	1.74	0.00
FALLOW	13.41	1.31	5.74	4.06	1.86
FWM	4.21	3.51	5.39	3.17	1.39
GREENHOUSE	26.57	0.56	0.85	0.39	1.06
M. CHAPARRAL	0.09	9.51	5.64	3.41	0.05
RIPARIAN	0.09	7.32	4.55	2.51	0.11
SAGE SCRUB	1.34	13.82	13.87	37.20	1.75
SLOUGH WATER	0.10	0.29	0.53	0.63	78.17
TURF	0.45	0.97	5.34	1.00	0.88
CULT. FIELDS	0.67	2.44	6.84	2.21	1.40
DUNE SCRUB	2.03	3.17	4.21	8.30	0.84
CHAPARRAL	0.38	13.73	9.08	4.71	0.33
SUNLIT OAK	0.35	8.15	7.83	4.45	0.09
SHADOWED OAK	0.06	9.74	5.15	4.08	0.02
DRY PONDS	14.63	3.48	5.76	4.38	0.63
TIDAL WETLAND	1.61	6.82	7.11	8.23	0.80
PONDS	5.72	5.35	6.85	7.76	8.22
Total	100.00	100.00	100.00	100.00	100.00

Table 6.1b SAM Confusion Matrix

Class	TURF	Ground Truth (Percent)			
		CULT. FIELDS	DUNE SCRUB	CHAPARRAL	SUNLIT OAK
Unclassified	0.00	0.01	0.00	0.00	0.00
CONIFERS	0.70	0.04	0.00	2.16	4.29
DEVELOPMENT	2.66	4.53	31.29	0.00	0.00
EUCALYPTUS	0.65	0.04	0.00	2.31	9.98
FALLOW	2.24	20.70	26.43	0.00	0.00
FWM	8.29	7.77	1.21	0.00	0.00
GREEN HOUSE	4.38	5.22	26.27	0.00	0.00
M. CHAPARRAL	0.67	0.28	0.08	13.11	0.05
RIPARIAN	0.63	0.84	0.06	16.43	0.00
SAGE SCRUB	3.87	1.59	4.65	0.72	1.45
SLOUGHWATER	0.17	0.08	0.76	0.00	0.00
TURF	41.78	11.62	0.05	0.00	16.70
CULT. FIELDS	11.34	13.19	0.27	1.01	0.00
DUNE SCRUB	1.23	1.41	2.71	0.00	0.00
CHAPARRAL	1.75	2.87	0.23	49.42	3.15
SUNLIT OAK	2.43	2.49	0.04	11.38	55.95
SHADOWED OAK	1.78	0.09	0.00	1.87	7.96
DRY PONDS	10.76	16.07	3.14	0.00	0.00
TIDAL WETLAND	1.87	1.84	1.40	1.59	0.00
PONDS	2.77	9.34	1.41	0.00	0.47
Total	100.00	100.00	100.00	100.00	100.00

Table 6.1c SAM Confusion Matrix

Class	SHADOWED OAK	Ground Truth (Percent)			Total
		DRY PONDS	TIDAL WETLAND	PONDS	
Unclassified	0.00	0.00	0.00	0.00	0.01
CONIFERS	10.59	0.20	0.04	0.35	0.97
DEVELOPMENT	0.00	2.61	3.66	4.32	5.18
EUCALYPTUS	14.87	0.23	0.03	0.22	1.10
FALLOW	0.00	28.80	5.49	8.09	14.69
FWM	0.00	5.23	5.90	3.86	5.95
GREENHOUSE	0.00	3.54	4.54	4.18	5.18
M. CHAPARRAL	0.00	0.81	0.28	3.60	1.47
RIPARIAN	0.00	0.90	0.42	1.69	1.48
SAGE SCRUB	12.37	7.98	15.41	16.63	6.42
SLOUGH WATER	1.20	0.12	22.00	7.80	5.96
TURF	0.23	0.41	4.34	2.57	7.58
CULT. FIELDS	0.00	1.34	5.61	2.45	8.42
DUNE SCRUB	0.00	4.56	6.22	4.52	2.72
CHAPARRAL	1.09	1.42	1.81	1.74	3.83
SUNLIT OAK	11.08	0.26	0.43	0.64	3.58
SHADOWED OAK	32.01	0.38	0.11	0.95	2.04
DRY PONDS	0.00	31.45	3.32	4.10	10.87
TIDAL WETLAND	0.00	4.65	6.50	5.20	3.33
PONDS	16.57	5.11	13.89	27.13	9.22
Total	100.00	100.00	100.00	100.00	100.00

Table 6.1d SAM Confusion Matrix

Class	Commission (Percent)	Omission (Percent)	Commission (Pixels)	Omission (Pixels)
CONIFERS	99.06	94.69	46212/46652	7848/8288
DEVELOPMENT	64.65	63.23	160694/248577	151106/238989
EUCALYPTUS	52.36	88.79	27537/52593	198494/223550
FALLOW	82.57	57.01	582014/704887	162946/285819
FWM	96.81	86.39	276539/285664	57899/67024
GREENHOUSE	96.64	73.43	240064/248417	23083/31436
M. CHAPARRAL	42.06	90.49	29576/70315	387694/428433
RIPARIAN	89.45	95.45	63673/71182	157497/165006
SAGE SCRUB	94.62	62.80	291602/308195	28008/44601
SLOUGH WATER	59.40	21.83	169843/285916	32420/148493
TURF	95.06	58.22	346007/363978	25039/43010
CULT. FIELDS	23.87	86.81	96521/404301	2026209/2333989
DUNE SCRUB	99.65	97.29	130167/130626	16470/16929
CHAPPARAL	99.81	50.58	183407/183750	351/694
SUNLIT OAK	99.37	44.05	170869/171951	852/1934
SHADOWED OAK	97.57	67.99	95613/97992	5052/7431
DRY PONDS	99.79	68.55	520753/521836	2361/3444
TIDAL WETLAND	71.29	93.50	113856/159712	659853/705709
PONDS	97.27	72.87	430305/442390	32456/44541

Table 6.1<sup>c</sup> SAM Confusion Matrix

Class	Prod. Acc. (Percent)	User Acc. (Percent)	Prod. Acc. (Pixels)	User Acc. (Pixels)
CONIFERS	5.31	0.94	440/8288	440/46652
DEVELOPMENT	36.77	35.35	87883/238989	87883/248577
EUCALYPTUS	11.21	47.64	25056/223550	25056/52593
FALLOW	42.99	17.43	122873/285819	122873/704887
FWM	13.61	3.19	9125/67024	9125/285664
GREENHOUSE	26.57	3.36	8353/31436	8353/248417
M. CHAPARRAL	9.51	57.94	40739/428433	40739/70315
RIPARIAN	4.55	10.55	7509/165006	7509/71182
SAGE SCRUB	37.20	5.38	16593/44601	16593/308195
SLOUGH WATER	78.17	40.60	116073/148493	116073/285916
TURF	41.78	4.94	17971/43010	17971/363978
CULT. FIELDS	13.19	76.13	307780/2333989	307780/404301
DUNE SCRUB	2.71	0.35	459/16929	459/130626
CHAPPARAL	49.42	0.19	343/694	343/183750
SUNLIT OAK	55.95	0.63	1082/1934	1082/171951
SHADOWED OAK	32.01	2.43	2379/7431	2379/97992
DRY PONDS	31.4	0.21	1083/3444	1083/521836
TIDAL WETLAND	6.50	28.71	45856/705709	45856/159712
PONDS	27.13	2.73	12085/44541	12085/442390

Table 6.1f SAM Confusion Matrix

Class	Ground Truth (Percent)				
	CONIFER	DEVELOPMENT	EUCALYPTUS	FALLOW	FWM
Unclassified	96.14	83.18	98.01	80.29	96.09
CONIFERS	0.00	0.00	0.00	0.00	0.00
DEVELOPMENT	0.01	7.62	0.01	0.09	0.07
EUCALYPTUS	0.00	0.00	0.00	0.00	0.00
FALLOW	0.49	1.74	0.03	16.26	1.60
FWM	0.00	0.00	0.00	0.00	0.00
GREENHOUSE	0.29	3.31	0.04	0.20	0.18
M. CHAPARRAL	0.00	0.00	0.00	0.00	0.00
RIPARIAN	0.00	0.00	0.00	0.00	0.00
SAGE SCRUB	0.00	0.00	0.00	0.00	0.00
SLOUGH WATER	0.57	0.01	0.01	0.00	0.00
TURF	0.53	0.36	0.03	0.26	0.67
CULT. FIELDS	0.11	0.50	0.05	0.36	0.50
DUNE SCRUB	0.06	0.25	0.00	0.08	0.17
CHAPARRAL	0.08	0.01	0.24	0.00	0.09
SUNLIT OAK	0.34	0.01	0.51	0.01	0.03
SHADOWED OAK	0.27	0.00	0.73	0.00	0.00
PONDS	0.98	1.12	0.08	0.05	0.36
TIDAL WETLAND	0.02	0.08	0.04	0.03	0.03
DRY PONDS	0.11	1.80	0.20	2.35	0.19
Total	100.00	100.00	100.00	100.00	100.00

Table 6.2a MAXL Confusion Matrix

Class	Ground Truth (Percent)				
	GREENHOUSE	M. CHAPARRAL	RIPARIAN	SAGE SCRUB	SLOUGH WATER
Unclassified	53.27	96.68	96.73	98.33	21.95
CONIFERS	0.00	0.00	0.00	0.00	0.00
DEVELOPMENT	3.41	0.04	0.17	0.01	0.65
EUCALYPTUS	0.00	0.00	0.00	0.00	0.00
FALLOW	0.45	0.06	0.67	0.07	0.31
FWM	0.00	0.00	0.00	0.00	0.00
GREENHOUSE	41.28	0.29	0.29	0.15	0.38
M. CHAPARRAL	0.00	0.00	0.00	0.00	0.00
RIPARIAN	0.00	0.00	0.00	0.00	0.00
SAGE SCRUB	0.00	0.01	0.01	0.10	0.00
SLOUGH WATER	0.01	0.00	0.00	0.00	71.22
TURF	0.12	0.05	0.27	0.02	0.02
CULT. FIELDS	0.51	0.02	0.56	0.02	0.09
DUNE SCRUB	0.17	0.03	0.07	0.02	0.09
CHAPARRAL	0.00	1.43	0.05	0.11	0.00
SUNLIT OAK	0.02	0.18	0.06	0.20	0.00
SHADOWED OAK	0.00	0.19	0.04	0.13	0.00
PONDS	0.16	0.06	0.30	0.06	5.06
TIDAL WETLAND	0.03	0.01	0.03	0.01	0.22
DRY PONDS	0.58	0.96	0.77	0.79	0.00
Total	100.00	100.00	100.00	100.00	100.00

Table 6.2b MAXL Confusion Matrix

Class	Ground Truth (Percent)				
	TURF	CULT. FIELDS	DUNE SCRUB	CHAPPARAL	SUNLIT OAK
Unclassified	51.18	80.26	92.10	87.18	90.85
CONIFERS	0.00	0.00	0.00	0.00	0.00
DEVELOPMENT	0.13	0.38	1.21	0.00	0.00
EUCALYPTUS	0.00	0.00	0.00	0.00	0.00
FALLOW	0.43	3.04	1.73	0.00	0.00
FWM	0.00	0.00	0.00	0.00	0.00
GREENHOUSE	3.55	0.24	3.41	0.00	0.00
M. CHAPARRAL	0.00	0.00	0.00	0.00	0.00
RIPARIAN	0.00	0.00	0.00	0.00	0.00
SAGE SCRUB	0.00	0.00	0.00	0.00	0.00
SLOUGH WATER	0.00	0.00	0.43	0.00	0.00
TURF	42.19	1.13	0.00	0.00	0.00
CULT. FIELDS	0.30	7.40	0.01	0.00	0.00
DUNE SCRUB	0.05	0.11	0.90	0.00	0.00
CHAPPARAL	0.00	0.00	0.00	12.82	0.00
SUNLIT OAK	0.03	0.03	0.00	0.00	9.15
SHADOWED OAK	0.00	0.00	0.00	0.00	0.00
PONDS	0.17	0.05	0.02	0.00	0.00
TIDAL WETLAND	0.03	0.01	0.19	0.00	0.00
DRY PONDS	1.94	7.35	0.00	0.00	0.00
Total	100.00	100.00	100.00	100.00	100.00

Table 6.2c MAXL Confusion Matrix

Class	Ground Truth (Percent)				Total
	SHADOWED OAK	PONDS	TIDAL WETLAND	DRY PONDS	
Unclassified	96.54	73.93	72.91	81.62	80.37
CONIFERS	0.00	0.00	0.00	0.00	0.00
DEVELOPMENT	0.00	1.02	0.32	0.52	0.68
EUCALYPTUS	0.00	0.00	0.00	0.00	0.00
FALLOW	0.00	0.83	1.67	4.82	2.87
FWM	0.00	0.00	0.00	0.00	0.00
GREENHOUSE	0.00	1.10	1.86	0.32	0.95
M. CHAPARRAL	0.00	0.00	0.00	0.00	0.00
RIPARIAN	0.00	0.00	0.00	0.00	0.00
SAGE SCRUB	0.00	0.01	0.01	0.03	0.00
SLOUGH WATER	0.00	0.30	13.97	0.00	4.26
TURF	0.00	0.95	0.07	0.20	1.01
CULT. FIELDS	0.00	0.20	0.10	0.06	3.70
DUNE SCRUB	0.00	0.48	0.13	0.03	0.11
CHAPPARAL	0.00	0.00	0.00	0.00	0.15
SUNLIT OAK	0.26	0.02	0.01	0.00	0.06
SHADOWED OAK	3.20	0.01	0.00	0.00	0.06
PONDS	0.00	20.10	7.24	1.57	1.52
TIDAL WETLAND	0.00	0.65	1.44	0.12	0.24
DRY PONDS	0.00	0.41	0.28	10.71	4.01
Total	100.00	100.00	100.00	100.00	100.00

Table 6.2d MAXL Confusion Matrix

Class	Commission (Percent)	Omission (Percent)	Commission (Pixels)	Omission (Pixels)
CONIFERS	0.00	100.00	0/0	8288/8288
DEVELOPMENT	44.61	92.38	14665/32871	220783/238989
EUCALYPTUS	0.00	100.00	0/0	223550/223550
FALLOW	66.19	83.74	91018/137505	239332/285819
FWM	100.00	100.00	2/2	67024/67024
GREENHOUSE	71.46	58.72	32485/45462	18459/31436
M. CHAPARRAL	0.00	100.00	0/0	428433/428433
RIPARIAN	0.00	100.00	0/0	165006/165006
SAGE SCRUB	74.72	99.90	133/178	44556/44601
SLOUGH WATER	48.32	28.78	98889/204643	42739/148493
TURF	62.39	57.81	30095/48239	24866/43010
CULT. FIELDS	2.79	92.60	4960/177684	2161265/2333989
DUNE SCRUB	97.14	99.10	5171/5323	16777/16929
CHAPARRAL	98.73	87.18	6926/7015	605/694
SUNLIT OAK	94.29	90.85	2925/3102	1757/1934
SHADOWED OAK	91.75	96.80	2648/2886	7193/7431
PONDS	87.73	79.90	64026/72977	35590/44541
TIDAL WETLAND	12.15	98.56	1405/11568	695546/705709
DRY PONDS	99.81	89.29	192095/192464	3075/3444

Table 6.2° MAXL Confusion Matrix

Class	Prod. Acc. (Percent)	User Acc. (Percent)	Prod. Acc. (Pixels)	User Acc. (Pixels)
CONIFERS	0.00	0.00	0/8288	0/0
DEVELOPMENT	7.62	55.39	18206/238989	18206/32871
EUCALYPTUS	0.00	0.00	0/223550	0/0
FALLOW	16.26	33.81	46487/285819	46487/137505
FWM	0.00	0.00	0/67024	0/2
GREENHOUSE	41.28	28.54	12977/31436	12977/45462
M. CHAPARRAL	0.00	0.00	0/428433	0/0
RIPARIAN	0.00	0.00	0/165006	0/0
SAGE SCRUB	0.10	25.28	45/44601	45/178
SLOUGH WATER	71.22	51.68	105754/148493	105754/204643
TURF	42.19	37.61	18144/43010	18144/48239
CULT. FIELDS	7.40	97.21	172724/2333989	172724/177684
DUNE SCRUB	0.90	2.86	152/16929	152/5323
CHAPARRAL	12.82	1.27	89/694	89/7015
SUNLIT OAK	9.15	5.71	177/1934	177/3102
SHADOWED OAK	3.20	8.25	238/7431	238/2886
PONDS	20.10	12.27	8951/44541	8951/72977
TIDAL WETLAND	1.44	87.85	10163/705709	10163/11568
DRY PONDS	10.71	0.19	369/3444	369/192464

Table 6.2f MAXL Confusion Matrix

## LIST OF REFERENCES

Campbell, James B., Introduction to Remote Sensing, The Guilford Press, New York, NY, 1996.

Canadian Geomatic Solutions, Ltd., "Remote Sensing: Key Concepts",  
<http://www.CGSL.com/6.htm>

Cook, M., Peterson, B., Dial, G., Gibson, L., Gerlach, F., Hutchens, K., Kudola, R., Bowen, H., "IKONOS Technical Performance Assessment," *SPIE Proceedings*, Vol. 4381, April 2001.

Fried, D.L., "Optical Radiation Through a Randomly Inhomogeneous Medium for Very Long and Very Short Exposures," *J. Opt. Soc. Amer.*, Vol. 56, 1966, p. 1372.

Gibson, Paul J., Introductory Remote Sensing: Principles and Concepts, Routledge, New York, NY, 2000.

Hufnagel, R.E. and N.R. Stanley, "Modulation Transfer Function Associated with Image Transmission Through Turbulent Media," *J. Opt. Soc. Amer.*, No. 54, 1964.

Iximaging, "Figures of Merit", <http://www.Iximaging.com/merits/>

Karim, Mohammad A, Electro-optical Devices and Systems, PWS-KENT Publishing Company, Boston, MA, 1990.

Kruse, F. A. et al., The spectral image processing system (SIPS) – Interactive Visualization and Analysis of Imaging Spectrometer Data, *Remote Sensing of the Environment*, v.44, 1993.

Lillesand, Thomas M. and Kiefer, Ralph W., Remote Sensing and Image Interpretation, 2<sup>nd</sup> Edition, John Wiley & Sons, New York, Chichester, Brisbane, Toronto, Singapore, 1987.

Lintz, Joseph Jr. and Simonett, David S., Remote Sensing of Environment, Addison-Wesley Publishing Company, Inc., Reading, MA, 1976.

Lo, C. P., Applied Remote Sensing, Longman Scientific and Technical, New York, NY, 1986.

Mather, Paul M., Computer Processing of Remotely-Sensed Images: An Introduction, 2<sup>nd</sup> Edition, John Wiley & Sons, Chichester, England, 1999.

Multispectral Users Guide, Department of Defense, August 1995.

NASA, "Landsat7 Science Data Users Handbook (SDUH)",  
[http://ltpwww.gsfc.nasa.gov/IAS/handbook/handbook\\_htmls/chapter6/chapter6.html](http://ltpwww.gsfc.nasa.gov/IAS/handbook/handbook_htmls/chapter6/chapter6.html)

Rees, W. G., Physical Principles of Remote Sensing, Cambridge University Press, New York, Port Chester, Melbourne, Sydney, 1990.

Richards, John A., Remote Sensing Digital Image Analysis: An Introduction, Springer-Verlag, Berlin, 1995.

Seyrafi, Khalil and Hovanessian, S. A., Introduction to Electro-optical Imaging and Tracking Systems, Artech House, Boston, London, 1993.

Silberstein, Mark and Campbell, Eileen, Elkhorn Slough, Monterey Bay Aquarium Foundation, Monterey, CA, 1989.

Spaceimaging, "The Digital Camera for IKONOS",  
<http://www.Spaceimaging.com/aboutus/satellites/IKONOS/kodak.htm>

Vexcel, "Orthorectification: What, Why, How, Who?",  
<http://www.Vexcel.com/aerial/orthophotos.html>

Wilkie, David S. and Finn, John T., Remote Sensing Imagery for Natural Resources Monitoring: A Guide for First-Time Users, Columbia University Press, New York, NY, 1996.

## INITIAL DISTRIBUTION LIST

1. Defense Technical Information Center .....  
Ft. Belvoir, Virginia
2. Dudley Knox Library .....  
Naval Postgraduate School  
Monterey, CA
3. Dr. Richard C. Olsen, Code PH/Os .....  
Naval Postgraduate School  
Monterey, CA
4. Ens Jamada J. Garner, USN .....  
Knoxville, TN
5. Alan Ross, SP .....  
Naval Postgraduate School  
Monterey, CA
6. Eric J. Van Dyke .....  
Elkhorn Slough National Estuarine Research Reserve  
Watsonville, CA
5. William B. Maier II, Code PH/MW .....  
Naval Postgraduate School  
Monterey, CA